

Investigation of Protein-drug Interaction using Capillary Isoelectric
Focusing with Whole Column Imaging Detection and
Spectroscopic Techniques

by

Tibebe Lemma Mukria

A thesis

presented to the University of Waterloo

in fulfillment of the

thesis requirement for the degree of

Doctor of Philosophy

in

Chemistry

Waterloo, Ontario, Canada, 2009

© Tibebe Lemma Mukria 2009

AUTHOR'S DECLARATION

I hereby declare that I am the sole author of this thesis. This is a true copy of the thesis, including any required final revisions, as accepted by my examiners.

I understand that that my thesis may be made electronically available to the public.

ABSTRACT

In this work, the possibilities of understanding protein-drug interactions and the possible modes of action of the drug have been explored using capillary isoelectric focusing (CIEF) and spectroscopic techniques.

The first study involves the implementation and applications of the new high performance Raman spectrometer with volume phase (VPH) based grating system, which is integrated with a short liquid-core optical waveguide for characterization and analysis of a wide range of molecules. The high performance Raman spectrometer has allowed us to measure solid samples with minor differences in chemical compositions. In addition, spectral characteristics of the interactions between therapeutic drugs with human serum albumin have been examined in terms of the cleavage of disulfide (S-S) bonds. The relative intensity of the Raman signal decreases as a complex formation progresses, suggesting perturbation around the disulfide bonds of human serum albumin (HSA).

This spectrometer is likely to be broadly applicable for simple to moderately complex samples. Furthermore, the future perspective of combining separation and spectroscopy technologies is a novel approach for capitalizing on the strengths of the two technologies.

Capillary isoelectric focusing (CIEF) with whole column imaging detection (WCID) was used to investigate the interaction of platinum-based anticancer drugs, cisplatin and oxaliplatin, with human hemoglobin A₀ (Hb) and HSA. This technique facilitates the investigation and characterization of the

formation of adducts between drugs and proteins. At higher drug to protein molar ratios (for both oxaliplatin and cisplatin), the results exhibit significant changes in the peak shapes and heights, which may indicate the destabilization of the protein. However, the conformational change was less evident at lower molar ratios. In addition, a major pI shift was observed for the oxaliplatin reaction mixtures (for 1:10, 1:50 and 1:100 ratios). In comparison with previously reported findings obtained by other analytical methods, conclusions were drawn about the validity of CIEF as a simple and convenient method for the investigation of protein-drug interactions. These results may provide useful information for further understanding the activity and toxicity of these chemotherapeutic drugs and improving their clinical performance.

Spectroscopic evidence also shows that oxaliplatin causes fluorescence quenching of HSA by formation of on HSA-oxaliplatin complex. The Stern-Volmer equation has been used to calculate the quenching constant in the linear range. The quenching rate constants K_q at three different temperatures indicate the presence of a static quenching mechanism in the interactions of oxaliplatin with HSA. The work describes the validity of the CIEF-WCID technique for the study of protein-drug interactions and provides useful information and insight into the interaction of anti-cancer drugs with HSA concerning their further toxicity of these chemotherapeutic drugs and ways of improving their clinical performance.

Finally, a novel two-dimensional (2D) protein characterization using a single one dimensional separation followed by a second characterization in the same instrument was developed. The technique combines capillary isoelectric focusing (CIEF), which separate proteins based on their isoelectric points, with a dynamic imaging focusing and allows estimates of their molecular weights from measurement of their diffusion coefficients. This techniques applies to simple to moderately complex protein samples.

ACKNOWLEDGEMENTS

First, I would like to thank my advisor, Prof. Pawliszyn for his support and guidance throughout my studies at UW. His support and leadership have been instrumental in my development as a research scientist.

I would like to thank my Co-Advisor Dr. Pawluczyk Romuald for his valuable suggesting for the Raman spectrum data collection and interpretation and help me conduct these experiments in his company. He was always been on helping me solve problems which came during my projects. This work would not have been possible without his guidance and dedication. Much of the work was completed in Chapter 2 by his two coop students: Andrew and Paul Nogas. I would also like to thank Olga Pawluczyk for her time and financial support.

I am graceful for the helpful suggestions and advice I have received from the members of my supervisory committee throughout my doctoral studies: Dr. Jim Sloan, Dr. Brenden J. McConkey and Dr. Richard A. Manderville. I would also like to thank to Dr. Palmer for the use of his fluorescence equipment and Dr. Tang for use of her Raman spectroscopy system.

A special thank you goes to Dr. Anderson and Mrs. Anderson for their friendship and help me with the correction of my thesis.

I also thank my previous advisor and group members Dr. Aroca, Case, Paul, and Nicholas (Nik).

I would like to thank my colleagues Dr. Lui Zhen, Wendy, Erasmus, David Donkor, Andrew, Paul Nogas and Leslie for helping me in my research and making my stay here a fun and memorable one. My appreciation is also extended to the faculty, staff members and to the members of chemical stores and machine shop at the Chemistry Department for their support during my graduate studies at UW.

Finally, I would like to thank to my beloved sister , Frezewed (Masho) Turner and her family, Larry Turner, my beautiful niece Melina Turner and Larry Junior and to my other family and dear friends, Tewodros Asefa, Zaid Solomon, Tsegereda Sebhatu and my godson Emmanuel and my beautiful Yodit for their love and encouragement not only to pursue my dreams, but throughout my entire life. I love you all.

DEDICATION

*In memory of my brother
Wondesen Lemma*

*To my beloved sister Frezewed (Masho)
Turner
for her patience, love and support throughout my studies*

TABLE OF CONTENTS

List of Figures	xxi
List of Tables	xxii
Glossary	xxiii
Chapter 1	1
1.1 Introduction	1
1.1.1 Isoelectric Focusing	1
1.1.2 Carrier Ampholytes	4
1.1.3 Capillary Isoelectric Focusing	5
1.1.3.1 Two-step CIEF	11
1.1.3.2 Single-step CIEF	14
1.1.3.3 Whole Column Imaging Detection	14
1.2 Detection Techniques	16
1.2.1 UV/Vis Detection	16
1.2.2 Fluorescence detection	17
1.3 Vibrational Spectroscopy	18
1.3.1 Raman Spectroscopy	21
1.3.1.1 Theoretical overview	24
1.4 Thesis Objectives and Overview	28
Chapter 2 Inexpensive and high performance Raman spectrometer using volume phase holographic diffraction grating	29
2.1 Introduction	29

2.2 Experimental	32
2.2.1 Outline of the new instrument.....	32
2.2.1.1 Volume phase holographic (VPH) diffraction grating.....	35
2.2.1.2 Detector.....	39
2.2.1.3 System Calibration.....	41
2.2.1.4 Laser line and edge pass filters.....	41
2.2.1.5 Integrating cavity cell.....	42
2.2.1.6 Data collection.....	42
2.2.1.7 Data processing.....	42
2.2.2 Materials and Chemicals	43
2.2.3 Sample Preparation	43
2.2.4 Theoretical Calculation	44
2.3 Results and Discussion	44
2.4 Conclusions	54
Chapter 3 Application of High Performance Liquid-Core Waveguide	
Raman Spectroscopy for Protein-drug Characterization	55
3.1 Introduction	55
3.2 Experimental	61
3.2.1 Apparatus.....	61
3.2.1.1 Raman instrumentation	61

3.2.1.1.1 Raman spectroscopy using 632.8nm excitation.....	61
3.2.1.1.2 LCW sample delivery.....	61
3.2.1.1.3 LCW-RS system from a distance of 70cm	62
3.2.2 Data collection.....	64
3.2.3 System calibration.....	64
3.2.4 Raman signals.....	65
3.2.5 Data processing.....	65
3.2.6 Raman liquid waveguide assembly.....	67
3.2.6.1 Cartridge assembly for fluorescence measurement.....	69
3.2.7 Materials and chemicals.....	70
3.2.8 Solutions and sample preparations.....	70
3.3 Results and Discussion.....	71
3.3.1 Raman measurement of HSA, oxaliplatin and HSA-oxaliplatin complex using 633nm excitation.....	71
3.3.1.1 Disulphide Bridges.....	71
3.3.1.2 Amide-I and III.....	74
3.4 Liquid core waveguide (LCW) using high performance Raman spectroscopy under illuminated conditions from a distance of 70 cm using 785nm laser line.....	78
3.4.1 Intensity of Raman radiation.....	78
3.4.2 Raman spectral features of Teflon AF 2400 tube and water.....	78
3.4.3 Remote spectral measurements with fibre-optic coupled with LCW-RS from a distance of 70 cm.....	83

3.5 Application of CIEF-LCW by the combined Raman/fluorescence spectrometer to measure fluorescence spectra of proteins using 488nm excitation line.....	89
3.6 Limitations of LCW-RS.....	93
3.7 Conclusions.....	94
Chapter 4 Investigation of interaction between human hemoglobin A₀ and platinum anticancer drugs by capillary isoelectric focusing with whole column imaging detection*.....	96
4.1 Introduction.....	96
4.2 Experimental.....	102
4.2.1 Aparatus.....	102
4.2.2 Chemicals.....	104
4.2.3 Solutions and sample preparation.....	104
4.2.4 Incubation of Hb with Oxaliplatin and Cisplatin.....	104
4.2.5 Preparation of Erythrocyte samples from patients and healthy volunteer.....	105
4.3 Results and Discussion.....	105
4.3.1 Oxaliplatin- Hb interaction.....	105
4.3.2 Cisplatin- Hb interaction.....	112
4.3.3 Cisplatin and oxaliplatin – adducts in Erythrocytes of Cancer Patiens undergoing oxaliplatin and cisplatin treatment.....	117
4.4 Conclusion.....	119

Chapter 5 Human serum albumin interaction with oxaliplatin studied by capillary isoelectric focusing with the whole column imaging detection and spectroscopic method*	121
5.1 Introduction	121
5.2 Experimentals	125
5.2.1 Chemicals.....	125
5.2.2 Solutions and Sample Preparation.....	125
5.2.3 Incubation of HSA with oxaliplatin.....	126
5.2.4 Preparation of Metal Colloid.....	126
5.2.5 Characterization of Silver Colloids.....	126
5.2.6 CIEF system.....	127
5.2.7 UV/Vis absorption measurement.....	128
5.2.8 Fluorescence quenching measurement.....	128
5.3 Results and Discussion	129
5.3.1 CIEF Investigation of Oxaliplatin- HSA Interaction.....	129
5.3.2 UV/Vis spectra of HSA and HSA-oxaliplatin adducts.....	135
5.3.3 Fluorescence quenching spectra and quenching mechanism.....	139
5.3.4 Influence of silver colloid on protein's <i>pI</i>	143
5.4 Conclusion	146
Chapter 6 Capillary isoelectric focusing coupled with dynamic imaging detection: a one-dimensional separation for two-dimensional protein characterization*	148
6.1 Introduction	148

6.2 Experimental	153
6.2.1 Apparatus.....	153
6.2.2 CIEF Method	153
6.2.3 Materials and Chemicals.....	154
6.3 Results and Discussion	154
6.3.1 Diffusion Coefficient for Proteins and Peptides.....	154
6.3.2 Diffusion Coefficient of Small Molecules.....	162
6.4 Conclusions	166
Chapter 7 Summary and Recommendation for Future Studies	167
7.1 Summary	167
7.2 Future Studies	171
References	173

LIST OF FIGURES

Figure 1-1. The harmonic approximation for a diatomic molecules.....	20
Figure 1-2. Energy level diagram showing the basic transitions involved in Raman scattering of a vibrational energy level of hv_k , when excited by energy of hv_0	24
Figure 2-1. Schematic of VPH based line imaging / multichannel spectromete....	32
Figure 2-2. The schematic diagram of Raman spectrometer system using VPH based grating.....	34
Figure 2-3. Illustration of VPH and Relief gratings.....	36
Figure 2-4. Configuration of an assembled Volume Phase Holographic (VPH) grating.....	38
Figure 2-5. Quantum efficiency curve of deep depleted CCD detector. Reprinted courtesy of Princeton Instrument.....	40
Figure 2-6. The calculated DFT Rama intensities Tylenol and molecular structure.....	46
Figure 2-7. Raman spectra from Tylenol regular tablet in the 200-2000 cm^{-1} region. The excitation laser line is 785nm.	47
Figure 2-8. Raman spectra of Tylenol regular strength and Lifebrand solid tablet.....	52
Figure 2-9. Raman spectra of seven acetaminophen-containing Tylenol tablets; curves (1-7), Tylenol regular strength, Pharmasave, Rexall, Compliment, Life Brand, Exact and Cold Extra.....	53
Figure 3-1. Schematics of Liquid core optical fibre. The waveguide extends the laser light path length through total internal reflection inside the Teflon tubing.....	56
Figure 3-2. Schematic diagram of Raman system equipped with 632nm excitation line.....	62
Figure 3-3. Schematic diagram of Raman spectrometer showing the fibre coupled to the VPH grating.....	66

Figure 3-4. Schematic drawing for apparatus for the measurement of Raman spectra. For Raman signal collection, the optical fiber impinged on the Teflon tube.....	66
Figure 3-5. Schematic and image of the liquid-core waveguide system from a distance of 70 cm using 785 nm laser line. LCW, AF-2400 tubing (i.d., 150 μm ; o.d., 360 μm , length, 5 cm).....	69
Figure 3-6. Raman spectrum (300-800 cm^{-1}) of HSA ($5.0 \times 10^{-5} \text{ M}$) in phosphate buffer at pH 7.40. The spectrum acquisition time was 20sec.....	72
Figure 3-7. Analysis of the S-S Raman band of HSA ($5.0 \times 10^{-5} \text{ M}$) , with oxaliplatin in 1:10 molar ratio. The spectrum was collected under physiological conditions (in phosphate buffer at pH 7.40, 0.10M NaCl).....	73
Figure 3-8 Raman spectrum of HSA ($5.0 \times 10^{-5} \text{ M}$) in the range of 1000-2000 cm^{-1} before incubation with oxaliplatin. The spectrum has been smoothed and baseline corrected using the Origin software package.....	75
Figure 3-9. Raman spectrum of HSA after incubation with oxaliplatin. HAS ($5.0 \times 10^{-5} \text{ M}$) was incubated in 1:10 molar ratio with oxaliplatin ($5.0 \times 10^{-5} \text{ M}$). The incubated solution was kept at 37 ⁰ C for 1h before being inserted into the Teflon tube.....	76
Figure 3-10. Raman spectra of HSA before and after incubation with oxaliplatin in molar ratio 1:10.....	77
Figure 3-11. Relation between NA and RI of an optical fibre.....	79
Figure 3-12. Raman spectrum of empty Teflon® tube AF 2400 acquired with 785 nm excitation line. The inset in Figure 3-11 shows Teflon AF polymer structure.....	81

Figure 3-13. Comparison of source and target spectrometers, based on a view of comparable spectra. (A) Cyclohexane fingerprint spectrum from Sigma-Aldrich® ³² . (B) Cyclohexane spectrum in 5 cm long, 150µm i.d., 360µm o.d. acquired with $\lambda=785$ nm , the laser power at the sample was 15mW and the acquisition time was 1s.....	85
Figure 3-14. Standard Raman spectra of six alcohols.....	88
Figure 3-15. CIEF of FITC-labeled HSA 10µg/mL. The sample containing 2% pharmalytes (pH 3–10) and 0.5% PVP. Separation capillary: 5 cm , 150 ID Teflon® AF 2400 capillary. Applied voltage: 0–5 min, 1 kV; 5–15 min, 3 kV. Excitation: Argon ion 488 nm at 5-10 mW.....	90
Figure 3-16. CIEF of RPE sample 5µg/ mL RPE; containing 2% pharmalytes (pH 3–10) and 0.5% PVP. Separation capillary: 5-cm x150µm ID Teflon AF 2400 capillary. Other conditions as in Fig. 3-12.....	92
Figure 4-1. Major oxaliplatin and cisplatin metabolites.....	98
Figure 4-2. The schematic diagram of the whole column imaging detection for CIEF.....	103
Figure 4-3. The CIEF analysis of Hb A ₀ (10µmol/L) incubated for 3 days at 37°C. For the CIEF analysis, a sample solution (400µL) containing 2% pharmalytes (pH 3.0-10.0), pI markers (pI 6.14 and 8.40) and 0.5% PVP was injected into the capillary by pressure using a syringe. The catholyte and anolyte were 100mM NaOH and H ₃ PO ₄ consecutively. The focusing voltage was set at 500V for 2min and 3000V for the remainder of the focusing period.....	107
Figure 4-4. Electropherograms representative of binding of human hemoglobin A ₀ with oxaliplatin : (a) 1:1 ; (b) 1:10 ; (c) 1:50 and (d) 1:100 molar ratios . The drug-protein mixture were incubated for 3 days at 37°C. Appropriate amounts of	

the incubated samples were removed and mixed with 0.5% PVP, 2%
pharmalytes.....110

Figure 4-5. CIEF electropherograms of human hemoglobin A₀ incubated with cisplatin for 2 days at 37°C, at (a) 1:1; (b) 1:10; (c) 1:50 and (d) 1:100 molar ratios. Separation conditions as given in Section 2.2 (i.e. cisplatin, 10µmol/L; Hb A₀ , 0-100 µmol/L; 2% pharmalytes , pH 3-10;0.5% PVP; pI markers, pI 6.14 and 8.40; catholyte, 100mM NaOH; anolyte, 100mM H₃PO₄). The observed pI variations may rise from small changes of the capillary inner wall properties during successive runs. Separation voltage was set to 500V for 2 min and 3000V for the remainder of the time. For peak identification, see Table 1.....113

Figure 4-6. CIEF of Hb (1:100 ratios) incubated with oxaliplatin for 0 and 60 minutes at 37°C. The profiles displayed change of the peak area after 60 minutes incubation time. The separation conditions are described in Figure 4-3.....115

Figure 4-7. CIEF profile of Hb from cancer patients (lung and colorectal) undergoing oxaliplatin and cisplatin treatment : (a) from healthy volunteers; (b) colorectal; (c) lung cancer.....117

Figure 5-1. Atomic force microscopy (AFM) topographic and lateral force images of the silver nanoparticles.....127

Figure 5-2. The CIEF analysis of HSA (10µmol L⁻¹) incubated for 72hr at 37°C. For the CIEF analysis, a sample solution (400µL) containing 2% pharmalytes (pH 3.0-10.0), pI markers (pI 6.14 and 8.40) and 0.5% PVP was injected into the capillary by pressure using a syringe. The catholyte and anolyte were 100 mmol L⁻¹ NaOH and H₃PO₄ consecutively. The focusing voltage was set at 500V for 2min and 3000V for the remainder of the focusing period. The

observed pI variations may arise from small changes of the capillary inner wall properties during successive runs.....130

Figure 5-3. Electropherograms representative of binding of HSA with oxaliplatin: (a) 1:1 ; (b) 1:10 ; (c) 1:50 and (d) 1:100 molar ratios. The drug-protein mixtures were incubated for 3 days at 37°C. Appropriate amounts of the incubated samples were removed and mixed with 0.5% PVP, 2% pharmalytes (pH 3.0-10.0) and pI markers (4.65, 7.05, 8.40 and 9.77) for each CIEF run. Catholyte and anolyte were 100 mM NaOH and H₃PO₄. On electropherogram c and d, the pI markers were not mixed with the running sample due the formation of fragments after 24 and 48hr incubation time. For all solutions, the total concentration of HSA was constant: 5.0 x10⁻⁵mol L⁻¹.The separation conditions are described in Fig5-1.....132

Figure 5-4. The absorption spectra of HSA and tryptophan in the presence of oxaliplatin incubated in phosphate buffer at room temperature. For all solutions, the total concentration of HSA was constant: 5.0 x10⁻⁵mol L⁻¹ (a) HSA-oxaliplatin molar ratios at 0:1, 1:0, 1:1, 1:10 , 1:50 and 1:100 incubated molar ratios; (b) Tryptophan- oxaliplatin mixtures were (curves 12 to 1): 1:0, 1:1, 1:2 ,1:4,1:6,1:8,1:10,1:12,1:14,1:16,1:18 and 1:20 molar ratios.....136

Figure 5-5. The UV/Vis spectra of HSA-oxaliplatin in (a) 1:1, (b) 1:10, (c) 1:50 and (d) 1:100 molar ratio and the reaction mixtures incubated for 0, 1, 6, 12 and 24hours at 37⁰C in water bath. The incubated buffer contained 5.0 x10⁻⁵M HSA with oxaliplatin concentration varied from 5.0 x 10⁻⁵ to 5.0 x 10³mol/L.....137

Figure 5-6. Fluorescence spectra of HSA (5.0 x 10⁻⁵ mol L⁻¹) in the present of oxaliplatin (5.0 x 10⁻⁵ mol L⁻¹) at 47⁰C; curves (1-14), 0,1,0,2,0,4,0,6,0,8,0,10,0,12,0,14,0,16,0,18,0, 20.0 , 50.0 and 100.....140

Figure 5-7. Fluorescence spectra of HSA ($5.0 \times 10^{-5} \text{ mol L}^{-1}$): oxaliplatin ($5.0 \times 10^{-5} \text{ mol L}^{-1}$) : curves (1-14), 0, 1.0,2.0,4.0,6.0,8.0,10.0,12.0,14.0.16.0, 18.0,20.0,50.0 and 100.0, respectively; (a) 25°C , (b) 37°C141

Figure 5-8. Stern-Volmer plot for the binding of HSA-oxaliplatin at different temperatures (298, 310 and 320K).....142

Figure 5-9. The observed pI shift of hemoglobin A₀ upon incubated with Ag colloid for a short period of time. 0.3mg/mL of hemoglobin A₀ mixed with 20, 40, 80, 160, 320, 640 and 1000 μL of citrate colloid ($5.00 \times 10^{-3}\text{M}$)144

Figure 5-10. The Ag solutions which are prepared by the Lee procedures. The greenish yellow solution is prepared by citrate reduction procedures. This solution may show a strong SERS activity (Fig5-9). However, the second solution (the colloid particles collapsed) shows no SERS activity.....145

Figure 5-11. The optical absorption of silver colloidal particles.....146

Figure 6-1. The principle of the 2D protein characterization approach using CIEF- WCID. (a) CIEF experiment to measure the peak position in the pH gradient; (b) calibration curve of the pH gradient; (c) dynamically monitoring the diffusion of the protein band; (d) measuring the diffusion coefficient by plotting σ^2 against the separation time (t) ; (e) calibration curve for molecular weight measurement.....155

Figure 6-2. Measurement of diffusion coefficient of protein by CIEF-WCID. (a) The electropherograms at different separation times (the focusing was terminated at 7 min); (b) the plot of σ^2 against separation time. $\sigma^2 = -6.14 \times 10^{-4} (\pm 1.16 \times 10^{-5}) + 1.84 \times 10^{-6} (\pm 1.95 \times 10^{-8})t$, $r^2 = 0.9995$, $\text{SD} = 4.49 \times 10^{-6}$, $n = 7$. σ was calculated from the peak width at half peak height ($W_{1/2}$) according to $\sigma = W_{1/2}/2.35$. To simplify the data-processing, the separation time instead of the

diffusion time was used to perform the linear fit, which contributes an intercept in the resulting equation but makes no difference on the slope.....157

Figure 6-3. Calibration curve for the molecular weight estimation. $M^{-1/3} = 5.77 \times 10^{-4} (\pm 5.67 \times 10^{-4}) + 3.30 \times 10^4 (\pm 3.17 \times 10^2) D$, $r^2 = 0.9987$, $SD = 1.53 \times 10^{-3}$, $n = 16$158

Figure 6-4. The correlation between $M^{-1/3}$ and D when considering all proteins tested as monomers. The use of incorrect oligomeric states led to a degraded correlation (refer to Figure 4). $M^{-1/3} = 5.03 \times 10^{-3} (\pm 1.56 \times 10^{-3}) + 3.17 \times 10^4 (\pm 8.72 \times 10^2) D$, $r^2 = 0.9894$, $SD = 4.21 \times 10^{-3}$, $n = 16$159

Figure 6-5. Measurement of diffusion coefficient using capillary zone electrophoresis. (a) The electropherograms at different separation times; (b) plot of peak variance (σ^2) against separation time. Separation parameter; 50 mM, Phosphate Buffer, pH= 8.04 and samples injected from Anode ; 1.5kV applied voltage.....165

LIST OF TABLES

Table 2-1 Comparison of VPH and standard relief gratings.....	38
Table 2-2 Predicted frequencies and Raman Intensities associated with the stretching modes of the OH, NH, and CO Chemical Functions and the CH stretching modes of the CH ₃ group and the phenol ring of acetaminophen in the optimized structure from the DFT-B3PW91 methods.....	47
Table 2-3 Tablets that contain acetaminophen-based Tylenol.....	50
Table 3-1 Refractive indices of various solvents and cell materials.....	82
Table 3-2 Observed Raman frequencies of cyclohexane.....	86
Table 4-1 Experimental values of the pI shifts of Hb after Hb-oxaliplatin adducts formation.....	116
Table 5-1 Stern-Volmer dynamic quenching constants and quenching rate constant of HSA and oxaliplatin at different temperatures.....	142
Table 6-1 Experimental Diffusion Coefficients, Estimated Molecular Weights, and Associated Errors.....	160
Table 6-2 Diffusion coefficient of test compounds measured by capillary zone electrophoresis (CZE).....	164

GLOSSARY

C	Concentration
CAs	Carrier ampholytes
CZE	Capillary zone electrophoresis
CCD	Coupled charge detection
CE	Capillary electrophoresis
CIEF	Capillary isoelectric focusing
CW	Continuous wave
D	Diffusion coefficient ($\text{m}^2 \cdot \text{s}^{-1}$)
D_{exp}	Diffusion coefficient experimental
D_{lit}	Diffusion coefficient literature
DACH	Trans-1-(R,R)-1,2-diaminocyclohexane
E	Electric field ($\text{V} \cdot \text{m}^{-1}$)
EOF	Electro-osmosis flow
F_0	Fluorescence intensities
<i>ggg</i>	Gauche-gauche-gauche
I	Current intensity (A)
i.d.	Internal diameter
IEF	Isoelectric focusing
Hb A	Human hemoglobin a
J	Current density ($\text{A} \cdot \text{dm}^{-2}$)
K_a	Acidic dissociation constant ($\text{mol} \cdot \text{dm}^3$)
K_b	Basic dissociation constant

K_q	Quenching rate constant
kV	Kilo volts
K_{SV}	Stern-Volmer dynamic quenching constant
LCW	Liquid-core waveguide
LIF	Laser-induced fluorescence
M	pH gradient
$M^{-1/3}$	Molecular weight
MS	Mass spectrometry
pI	Isoelectric point
pK	Dissociation constant
PVP	Polyvinylpyrrolidone
RI	Refractive index
r	Internuclear separation
SNRs	Signal to noise ratios
SPME	Solid phase microextraction
SERS	Surface enhanced Raman spectroscopy
SD	Standard deviation
τ_0	Average lifetime
TIR	Total internal reflection
t	Time
UV/VIS	Ultraviolet-visible
η	Viscosity
VPH	Volume phase holograph

V	Volume (dm ³)
W _{1/2}	Half peak height
WCID	Whole column imaging detection
X	Distance from the anode (cm)

CHAPTER 1

1.1 Introduction

1.1.1 Isoelectric Focusing

Isoelectric focusing (IEF)¹ is an electrophoretic focusing technique by which amphoteric compounds (proteins, enzymes, peptides, etc) are fractionated according to their isoelectric points (pI), which is directly related to the structure of the molecules and their acid–base properties along continuous pH gradients²⁻⁵. IEF has become a valuable tool on account of its high resolving power for the separation of protein mixtures. The method has long been used to separate, isolate, purify and analyze a variety of proteins. Historically, this simple technique is carried out either in vertical polyacrylamide rod gels or in horizontal polyacrylamide or agarose slab gels. These gels are polymerized on a support film. In the beginning of this technical innovation, sucrose concentration gradient columns in liquid phase was used to separate analytes⁶. After the first application to the separation of proteins performed by Svensson³, it became a powerful analytical separation technique and was used routinely in several research areas. The separation of amphoteric species is achieved efficiently by carrier ampholytes, which can generate a stable pH gradient throughout the separation gel when an electric field is applied to them. Amphoteric species can carry positive, negative or zero charge depending on the electrical charge they experience when rubbed out on a gel. Basically the technique exploits the differences in pI of different amphoteric species. After a pH gradient is created in analytical agarose, sephadex or

polyacrylamide gels by carrier ampholytes, analytes are separated on the basis of their isoelectric points (pI), moving in the gel matrix to the pH where their positive charge balances their negative charge. During migration through the pH gradient, if a protein has a net negative charge, migration is toward the anode, and it thus encounters a lower pH, so that it picks up more positive charge. The reverse happens when the protein has a net positive charge. Eventually, the protein will reach the point in the pH gradient where the net charge is zero. Therefore, at isoelectric point, the protein is uncharged, and since the migration ceases, it is focused in a narrow zone. After the protein is focused, any movement from the focused zone will gain a net charge and cause it to migrate back to the zone. Hence, a dynamic equilibrium is established in the mass transport due to diffusion and electromigration. The following differential equation describes the equilibrium between the electrophoretic and diffusional mass transport³:

$$C\mu E = DdC/dx \quad (1)$$

where μ is the mobility (m^2/Vs), C is the component concentration, D is the diffusion coefficient (m^2/s), E is the electric field strength (V/m), and x is the distance along the focusing axis. Integration of the above equation leads to a Gaussian profile. Therefore, sharper bands are obtained if the diffusion coefficient is low. This equation also demonstrates the different mobility when $pH=pI$. If the analytes diffuse out from their pI toward the anode, it will gain a

positive charge and start to migrate to the cathode and refocus at $pH=pI$. The same phenomenon happens if the analyte gains a negative charge. Thus, for a sharp band, the refocusing process should be faster than the rate of diffusion.

IEF demonstrates a higher resolution than other modes of electrophoresis. The resolution of IEF is determined by the slope of the pH gradient and the electric field applied. It has been demonstrated that proteins differing by 0.001 pI can be separated by IEF.⁷ However, routinely IEF provides a resolution of 0.1 to 0.01 pI units. For this technique, proteins (including enzyme isoforms, polyclonal and monoclonal antibodies, hemoglobin variants, and recombinant-DNA proteins), viruses, bacteria and peptides are most exclusively the samples which are characterized by IEF, due to their amphoteric nature generated by the presence of carboxylic and amino groups.

It is important to realize that IEF technique has several limitations: the precipitation of proteins at their pI and their intolerance of salt. Since amphoteric species have no charge and are electrically neutral at the pI point, the possibility of precipitation is very high at the pI point. High molecular weight proteins are highly susceptible to precipitation. Salt also interferes with the smooth gradient formation and the conductivity of the medium, due to the presence of highly conductive salt ions.

1.1.2 Carrier Ampholytes

Carrier ampholytes (CA) are a mixture of specially designed low molecular mass polyamino-polycarboxylic acids with slightly different pI values. These molecules exist as either anions or cations depending on the surrounding environment. When carrier ampholytes are subjected to an electrical field, the molecules rearrange in such a way that the lowest pI s migrate to the anode and those with the highest pI s move to the cathode, thus producing a smooth pH gradient. The carrier ampholytes continue to move through the capillary until each one reaches a place in the capillary where the pH of the solution equals the pI of the ampholyte; then a steady state is achieved. According to Svensson, a good carrier ampholyte should meet the following criteria: the isoionic solutions of these molecules should show a good buffering capacity, conduct in their isoelectric state, so that they can carry electric current and maintain the pH gradient and be highly soluble in water. In early work by Svensson^{3,8}, he clearly defined the requirements to make IEF a valuable technique to fractionate proteins. However, he could not find the appropriate compounds in the available catalogues to meet all the criteria he outlined in his theoretical work. Instead, Vesterberg⁸ first had the idea of random polymerization of pentaethylene hexamine with acrylic acid to produce a complex mixture of amino-oligocarboxylic acids which demonstrate the characteristics defined by Svensson. Since the mixture of these CA permits the establishment of pH gradients over a large pH range, CA contains from 50-1000 species per pH unit are in order to create a linear pH gradient⁹.

Furthermore, at least 30 ampholytes per pH unit are required in order to achieve a smooth pH gradient. Because of this large number of components with isoelectric points ranging from pH 3-10, many amphoteric analytes can be separated. However, the usual practice in the laboratory is to keep the concentration of the carrier ampholytes between 1 and 2%. The practical work was first performed by Vesterberg and Svensson ¹⁰ while the mathematical explanation was first reported by Hjerten ¹¹.

1.1.3 Capillary Isoelectric Focusing

IEF is a high resolution separation mode for the separation and analysis of amphoteric biomolecules on the basis of differences in their isoelectric points in an electric field. This powerful technique has been used since the first paper published by Svensson in 1961³. The method has long been used to separate, isolate, purify and analyze a variety of proteins. However, these methods are limited by a number of factors such as Joule heating, difficulty in quantification, and the time and labour required for analysis. Joule heating refers to the rising of temperature inside the separation column due to the application of an electric field. The development of capillary electrophoresis (CE) paved the way to the performing of IEF in a capillary. Then Hjerten and coworkers introduced IEF in a capillary format (CIEF)¹¹⁻¹⁴ in attempting to overcome the drawbacks with conventional gel IEF techniques. As in gel IEF, CIEF is a CE separation technique for proteins and peptide based on differences in isoelectric point (pI), and is characterized by high resolution and spontaneous focusing of analytes. This technique can be used also for the determination of

isoelectric point of proteins. Capillary isoelectric focusing (CIEF) combines the high resolving power of conventional gel IEF with the automation and quantization advantages of capillary electrophoresis instrumentation. CIEF is also advantageous in terms of requirement of small sample volume, effective Joule heat dissipation and real-time data acquisition. The narrow diameter capillary is responsible for the use of minute samples for analysis. The use of a narrow capillary can greatly reduce the Joule heating generated by the electrophoresis process. In CIEF, the entire capillary (50 to 100 μm) is initially filled with a solution containing the analyte of interest and carrier ampholytes; the carrier ampholytes establish a pH gradient within the capillary column during the focusing process. Before the focusing begins, one end of the capillary is immersed in a vial containing an anolyte solution (typically phosphoric acid) and the other in a catholyte solution (typically sodium hydroxide). Normally 0.02 M of phosphoric acid (H_3PO_4) and sodium hydroxide (NaOH) are used for the CIEF separation. The pH of phosphoric acid should be lower than the pI of the most acidic protein (ampholyte), and the pH of sodium hydroxide is higher than the pI of the most basic ampholytes. Thus, during the focusing process, the two extreme buffers prevent the ampholyte from exiting through the two ends of the capillary.

When proteins are carried through a capillary, under the influence of an electric field, electro-osmotic flow can interfere with the focusing procedure. Electro-osmotic flow (EOF) is caused by the absorption of analytes onto the

capillary wall. Since the surface of bare fused silica contains silanol (Si-OH) groups, when an acidic analyte passes through the capillary, the silanol group is ionized to negatively charged silanoate (Si-O⁻) groups. These negatively charged groups attract a positively charged group of the analyte of interest. However, the positively charged group attracted by the silanoate group is not enough to neutralize all the silanoate group so that a loose second layer is formed which attracts the opposite charge of the analyte-buffer composition. Thus, when an electric field is applied, this positively charged mobile layer (loosely attached to the capillary wall) is, attracted to the cathode, thus causing electro-osmotic flow. In CIEF, the presence of electro-osmotic flow interferes with the focusing process by causing zone broadening (distortion) and the formation of multiple peaks due to the incomplete formation of focusing of the nascent bands at both capillary ends ¹⁵. Therefore, the coating of the capillary before being used for separation can reduce the analyte-wall interaction and thus EOF. Since most of the CIEF separation is conducted in a small diameter capillary, the possibility of adsorption on the wall of the capillary is higher. At least two coating techniques have been recommended and implemented to overcome EOF: dynamic coating and chemical coating. Typically in dynamic coating, a coating agent such as a polymer or additives rinse through a capillary are mixed with the running buffer ¹⁶. Since coating agents such as polymers bind strongly to the silica surface, the column coated with polymer shows great stability ¹⁷. Unlike dynamic coating, chemical coating (permanent wall coating) required three steps : capillary pretreatment, introduction of double bonds to the capillary

wall, and binding of a polymer to the intermediate layer¹⁷. In the first step, the column etching using concentrated sodium hydroxide is followed by leaching with hydrochloric acid¹⁸. Then the column is coated by attaching a polymer by using a reactive bifunctional silane such as γ -methacryloxy propyl trimethoxy silane to the surface of the capillary. Finally the attachment of a polymer is achieved by using a free radical polymerization reaction with the established reactive olefinic sublayer on the silica surface. Even though this method shows variability in the coating thickness due to the formation of unreacted monomer residues, Righetti and co-worker resolved this problem by adding 3% short chains of polyacrylamide to the running buffer¹⁹. The other potential parameter contributing to good reproducibility is making a fresh solution of electrolyte, specially sodium hydroxide, which can absorb carbon dioxide if there is exposure to air which interferes with the focusing process²⁰.

The ampholyte composition is selected to achieve the desired resolution. For instance, for complex samples with a wide distribution of isoelectric points, a broad range of ampholyte (pH 3-10) is typically used. When a voltage is applied, the analyte of interest and carrier ampholytes migrate through the capillary until they reach a point where their charge is neutral (pI). At this point the separation current decreases significantly which indicates that the system has reached a steady state. The decrease in the current is due to the depletion of charge carriers as the protein is close to the pI point.

The resolving power for two species can be defined as follows ¹⁰:

$$\Delta pI = 3 \sqrt{\frac{D(dpH / dx)}{E(d\mu / dpH)}} \quad (2)$$

where D is the diffusion coefficient of the focused bands, E is the field strength, μ is the mobility of the protein, $d\mu/dpH$ expresses the mobility-pH relationship, and dpH/dx expresses the relationship between the changes of buffer pH per unit of capillary length. This equation shows how the resolution is increased by selecting an appropriate ampholyte pH range ². In the experiment the two variables (E and dpH/dx) can be manipulated in order to optimize the resolution. Higher voltage invokes an increased resolution and a narrow pH gradient leads to the same result. The other variables which are intrinsic to the sample are the diffusion coefficient and the rate of change of the mobility of the sample near its isoelectric point. It is apparent that a low diffusion coefficient and a large change of mobility with pH is desirable for higher resolution ². In addition, an ampholyte with a narrow pH range is selected to maximize the resolution. However, to separate wide pI ranges of analytes, broad ranges of ampholyte or mixtures of several ampholytes are typically used. If all the other parameters are well optimized, a resolution of 0.02pH unit can be obtained for the separation of amphoteric species.

The theoretical calculation of the isoelectric point for a simple amino acid can be obtained by averaging the two pK values:

$$pI = \frac{1}{2}(pK_i + pK_j) \quad (3)$$

where K_i and K_j are the dissociation constants of the two ionizations involving the carboxy and amino groups. For instance, (the amino acid glycine (Gly)), the isoelectric point of (Gly) can be calculated by averaging its two pK values. The pK of the carboxylic acid of Gly is 2.35 and the amino group is 9.78, thus yielding a pI of glycine $(2.35 + 9.78)/2 = 6.07$.

However, when the molecules contain several basic and acidic groups such as large peptides and proteins, the following equation must be used to estimate the pI²¹:

$$\text{Net charge} = \sum_i \frac{n_i}{\frac{K_i}{[H^+]} + 1} - \sum_j \frac{n_j}{\frac{[H^+]}{K_j} + 1} \quad (4)$$

where the molecule has i weakly basic groups (N-terminus) and j weakly acidic groups. Typically, $i=4$ arising from the N-terminus group, which includes the ϵ -amino group of lysine, the guanidinium group of Arg and the imidazole group of histidine and $j=5$, arising from the C-terminus (α -carboxylic) group, which includes, the β -carboxyl group of aspartic acid, γ -carboxyl of a glutamic acid, the phenolic group of tyrosine and the thiol of cysteine. This equation assumes that the dissociation constant, K , are the same for all side chains on the polypeptide or protein.

The CIEF method can be considered as complementary to IEF rather than a competitive technique, because the method exhibits specific ranges of applicability, with advantages and disadvantages. Even though the CIEF technique provides extremely high separation efficiency, quantitative information is chiefly provided by other techniques. The two disadvantages of this technique are protein precipitation at the pI and salt intolerance.

1.1.3.1 Two-step CIEF

Every commercial CE instrument is equipped with an on-line detection technique at a fixed point along the capillary²². Thus, it is necessary to have a method to transport the focused analyte zones toward the detection point and to pass to the detection window. This focusing and mobilization technique is called a two-step procedure. Three different techniques have been used to mobilize the focused bands: chemical, hydraulic and electro-osmotic mobilization techniques^{12, 23}. In chemical mobilization, the chemical composition of anolyte or catholyte solution is replaced with a solution of neutral salt such as NaCl, acid or base in one of the vials, after the separation voltage is turned off, which occurs when the drop off of the current is observed. This shows the completion of the focusing process. The choice of the anodic or cathodic mobilization and the choice of mobilizing agents depend on the analyte of interest and its pI point. Typically, proteins have isoelectric points between 5 to 10, thus mobilization toward a cathode is more practical²⁴.

The most common mobilization technique is the addition of NaCl to the analyte or catholyte vials. Usually solutions of H₃PO₄ (10 to 20 mM) and 20 to 40 mM of NaOH are used as anolyte and catholyte respectively. When the mobilization process is initiated, sodium serves as the non-proton cation in anodic mobilization, while chloride ion functions as the non-hydroxyl anion in cathodic mobilization. At the initial stage of the mobilization, the current stays low but gradually increases as the chloride ion enters the capillary. Similar to the focusing process, the mobilization applied electrical field ranges from 300 to 1000V/cm. Once the chloride ions are distributed throughout the capillary, the mobilization current starts to rise rapidly which indicates the end of the mobilization process. This process was first described by Hjerten et al ¹¹ with the following equation:

$$C_{H^+} + \sum C_{NH_3^+} = C_{OH^-} + \sum C_{COO^-} \quad (5)$$

where C_{H⁺} is the concentration of protons, C_{OH⁻} hydroxyl ions, C_{NH₃⁺}, C_{COO⁻} are positive and negative groups in the ampholytes, respectively ¹¹. For anodic mobilization, the non-proton reagent added to the anode, expands the left side of equation 5 by introducing an X_{n⁺} term. Thus, the above equation can be rewritten as follows:

$$C_{X_{n^+}} C_{H^+} + \sum C_{NH_3^+} = C_{OH^-} + \sum C_{COO^-} \quad (6)$$

However, if the salt (anion) is added to the catholyte, the above expression becomes

$$C_{H^+} + \sum C_{NH_3^+} = C_{OH^-} + \sum C_{COO^-} + C_{Y^{m-}} \quad (7)$$

where $C_{Y^{m-}}$ is an anion with valence m^- . The added salt competes with OH^- for electromigration to the separation capillary. For this reason a few hydroxyl ions enter the capillary, and as a result, the pH decreases. Similarly, the addition of non-proton cations into the capillary cause the pH to increase due to the reduction of proton concentration.

The other mobilization technique is hydraulic mobilization. In this technique, the focused bands move past the detector by physical means (pumped or aspirated). During hydraulic mobilization, band broadening is avoided by applying the focusing voltage during the elution. The advantage of leaving the focusing voltage during the mobilization is to maintain the resolution of the focused band²⁴.

The quest for a simple (one step) mobilization drives researchers to find an alternative technique, which applies without impairing the resolution of the focused band. The electro-osmotic mobilization technique is one which is often used. In this approach, EOF is used to mobilize the focused band²⁵. The mobilization procedure can be applied to both coated and uncoated separation capillaries.

1.1.3.2 Single-step CIEF

In single-step CIEF, focusing and mobilization steps occur simultaneously. In this mobilization technique, the whole content of the capillary moves to the detector, while focusing occurs simultaneously²⁵. After the capillary is filled with the sample of interest, the capillary is placed between the catholyte and anolyte, and an electrical field is applied to focus the analytes. Meanwhile, the focused bands are swept to the detector using EOF. Both coated and uncoated capillaries can be used for the single step CIEF method.

1.1.3.3 Whole Column Imaging Detection

Capillary isoelectric focusing (CIEF) is a CE separation technique for proteins and peptides based on differences in isoelectric point (pI) and is characterized by high resolution and spontaneous focusing of analytes. Analytes focus into narrow zones at different positions inside the capillary corresponding to their different pI values. Normally CIEF is performed using a common CE instrument with a 20- 50 cm long capillary with a single-point and on-column detection system. Eventually, the focused bands are mobilized to pass through the column to the detection point. The mobilization process can be accomplished by electrophoretic force, hydrodynamic flow, or electro-osmotic flow techniques. However, this traditional mobilization technique has some limitations associated with the mobilization process. Some of the limitations include the following: it takes longer time for the focused bands to move to the detection window^{11,12}; once a sample is injected into the separation column,

the separation process, peak broadening, sample absorption and the dynamics of the focusing cannot be monitored with the traditional detection techniques. In order to resolve these drawbacks, a new method called whole column imaging detection (WCID) was developed in our laboratory. Whole column imaging detection (WCID)²⁶⁻³⁰ is an attractive detection scheme for CIEF measurement. In CIEF–WCID, unlike single point detection, amphoteric analytes are focused into narrow stationary bands, followed by imaging detection with a CCD camera. As WCID eliminates the mobilization step required by the conventional single point detection, CIEF–WCID possesses three advantages over single point detection. First, the inherent characteristics of CIEF (high efficiency and high resolution) are maintained. Second, the optimization of separation conditions is simplified and the total separation time is greatly reduced. Third, the CIEF profiles at different focusing times can easily be obtained, which is suitable for dynamic monitoring of protein–protein and protein–drug interactions. Due to the growing interest in the separation science for such a unique technique, CIEF–WCID has found applications in the separation and characterization of small molecules³¹, peptides^{32,33}, proteins³²⁻³⁴, antibodies^{33,35}, viruses³⁵⁻³⁷ and cells³⁸. It has been demonstrated to be a powerful tool for the study of reactions of proteins³⁹, rapid two-dimensional characterization of proteins⁴⁰ and characterization of protein–DNA interactions³⁸.

1.2 Detection Techniques

In capillary electrophoresis, the common detection technique is UV/vis absorbance due to its ease of operation. This technique is easily adapted from high performance liquid chromatography (HPLC). In general, the most common detectors in CE are UV/vis absorbance, fluorescence (direct and indirect), laser-induced fluorescence, mass spectrometry, conductivity, amperometry (direct and indirect), radiometry and refractive index measurement. Several criteria should be fulfilled when a detector is used for sample analysis. Such criteria include sensitivity, linear dynamic range, selectivity, low noise and the ability to provide qualitative data²⁰.

1.2.1 UV/Vis Detection

UV-absorbance detection is the most widely used and the choice for the CE technique^{11, 12, 41}. This detection scheme is very popular so that almost all commercial instruments are equipped with UV/Vis detector. Light of intensity I_{in} from a source (lamp) is imaged on a capillary, where the sample absorbs some of the light. The transmitted intensity (I_{out}) from the capillary is detected with a photomultiplier tube or silicon photodiode. This transmitted intensity is then converted to an absorbance value :

$$T = I_{out}/I_{in} \quad (8)$$

where T is the transmittance.

There are different light sources used in absorbance detectors. These include broad band light produced from xenon and arc lamps. In HPLC, absorbance

detection at 280nm is typically used to monitor sample separation. Thus, the development of the CE detector is attributed to the ease of adaptation from the HPLC detector. For CE application, a high quality fused-silica capillary is necessary, since fused silica has a UV cutoff of approximately 170 nm⁴². This detection scheme is popular because no derivatization is needed. However, although UV/Vis is the choice of detection for several applications, this detection scheme is limited by the available path length and concentration sensitivity. For example, for some biologically active molecules, the concentration is too low (10^{-11} to 10^{-13} mol/L)⁴³ to detect by CE using an UV/Vis detector. A possible approach is to use a light source with high intensity and a better focus.

1.2.2 Fluorescence Detection

Fluorescence is the second most popular detection method implemented in the CE technique⁴⁴. Fluorescence provides high sensitivity and extremely low limits of detection for analytes separated by CE, but the technique gives little structural or diagnostic information. The choice of excitation sources is lamp or laser depending on the application of interest. Even though laser radiation is not available in a broad range of wavelengths (tunable lasers are still expensive), one can use continuous wave laser. In a capillary, although the amount of light absorbed is affected by the path length as in UV/Vis, the decrease in fluorescence intensity can be compensated by increasing the laser

power. This highly selective and sensitive technique is especially important for biological applications.

1.3 Vibrational Spectroscopy

Vibrational spectroscopy has been well established as a useful tool for the analysis of organic and inorganic substances, whether of biological, geological or synthetic origin. The vibrational spectroscopy of molecules can be determined by two spectroscopic techniques: infrared⁴⁵ and Raman spectroscopy⁴⁶. These two complementary techniques are well established for studies of the vibrational properties of molecules in gas, liquid and solid phases. The study of molecular vibrational frequencies, vibrational intensities, line shape/width, polarization of IR and Raman modes, and potential energy surfaces (force constants) are important for understanding several physical properties of molecules^{47, 48}. The information content of both techniques are complementary and equally important for the vibrational analysis of molecules, and is information that can be used for both qualitative and quantitative purposes. Infrared and Raman both depend on the interaction of electromagnetic radiation with molecule. However, the physical interaction of matter with electromagnetic radiation is different in the two techniques. In infrared spectroscopy, absorption occurs when the frequency of the incident radiation matches the vibrational frequency of a particular mode of vibration. Molecules are promoted to vibrational excited states after the energy is absorbed. IR activity is usually associated with changes in the dipole moment of the molecule

related to the vibrational motion. For infrared spectroscopy, the radiation covers a wide range of infrared energy. In contrast, in Raman spectroscopy the sample is irradiated with a single wavelength source, and the scattered photons from the sample are captured by an appropriate detector. Raman scattering arises from the distortion (changes in polarizability), of electron clouds around the nuclei after light interacts with a molecule. The IR and Raman activity of a given vibration also depends on the symmetry of the species.

Molecular vibrations can range from a simple oscillation of the two atoms in diatomic molecules to much more complex motions in polyatomic molecules. Each atom in a molecule has three degrees of freedom since it can move independently along the axes of a Cartesian coordinate system. If n atoms constitute a molecule, the $3n$ total degrees of freedom define the form of its normal modes. Normal modes are a set of collective atomic displacements which may be superimposed to describe the overall vibrational motion of a molecule⁴⁹. Three of these modes are involved in the translation of the entire molecules along the x , y and z -axes and the other three degrees of freedom involve the rotations of a molecule about the three principal axes of inertia. The remaining vibrational degrees of freedom (vibrational modes), are responsible for distance changes between atoms, such as the length of chemical bonds and the angles between them. Thus, for a non-linear molecule, the number of fundamental vibrational modes is $3n-3-3=3n-6$ and for a linear molecule, the number of modes is $3n-3-2=3n-5$ since linear molecules have only two

rotational degree of freedom, because the moment of inertia along the molecular axes is zero⁵⁰⁻⁵⁴.

The simplest way to describe and approximate the vibrational motion of a diatomic molecule is the cartoon picture of two masses (m_1 and m_2) attached with an elastic spring (Fig 1-1).

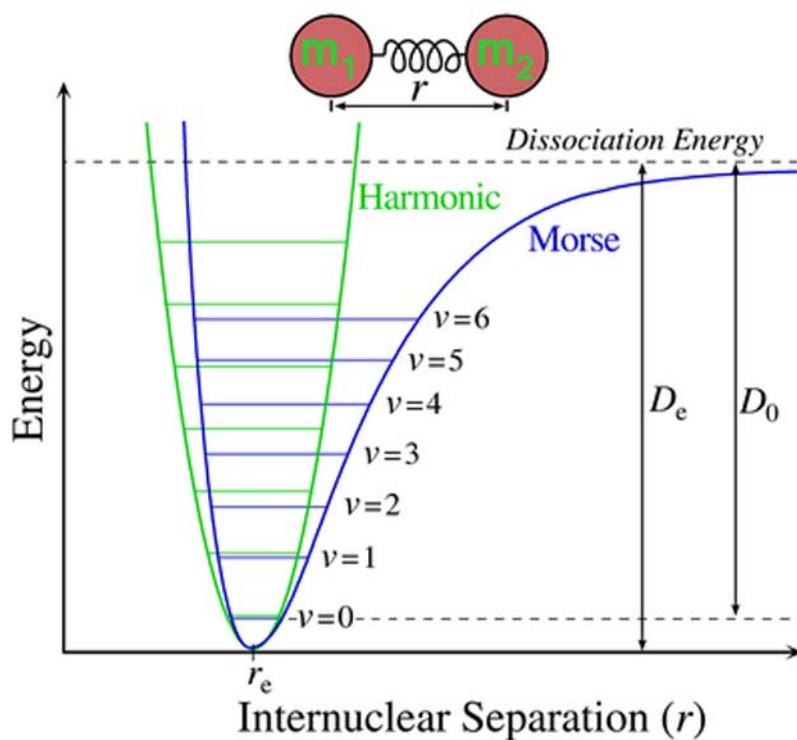


Figure 1-1. The harmonic approximation for a diatomic molecule.

This model will oscillate about the equilibrium position with a frequency proportional to the force constant f .

$$Force = -fr \quad (9)$$

f is a force constant, which is a measure of the strength of the bond and r is the displacement from equilibrium. Since force equals mass times acceleration, equation 9 becomes ⁵⁵:

$$Force = -fr = -\frac{\partial V^2}{\partial r^2} \cdot r = \mu \frac{\partial^2 r}{\partial t^2} \quad (10)$$

where $\mu = m_1 m_2 / (m_1 + m_2)$ is the reduced mass of diatomic molecule and t represents time. The solution of the above second order differential equation is:

$$r = r_0 \cos(2\pi\nu t + \theta) \quad (11)$$

where ν is vibrational frequency and θ the phase angle. Equation 11 describes the motion of the atoms as a harmonic oscillation. Finally we obtain the equation to describe the frequency of the vibrations of diatomic molecule:

$$\frac{\nu}{c} = \bar{\nu} = \frac{1}{2\pi c} \sqrt{\frac{f}{\mu}} \quad (12)$$

Where ν is the frequency of the vibration and $\bar{\nu}$ is the wavenumber, measured in cm^{-1} . In vibrational spectroscopy, it is a common practice to use wavenumber units instead of frequencies.

1.3.1 Raman Spectroscopy

The first experimental Raman effect was discovered by Raman and Krishnan in 1928⁴⁶. Before the experimental discovery of Raman scattering, several groups had predicted the Raman phenomenon. Historically, Raman

spectroscopy has been difficult to perform due to the high level of instrumental complexity. However, the continuing advance and improvement of lasers, highly sensitive detectors, holographic filters and the modern commercialization of the Raman system make this technique as useful and practical as infrared spectroscopy.

Raman scattering is used to obtain information about the structure and physical properties of the vibrational energy of a molecule. Since every compound has a unique spectral fingerprint, *and* since no two molecules give exactly the same Raman spectrum, and since the intensity of the scattered light is related to the amount of material present, it is easy to obtain both qualitative and quantitative information about a sample.

The Raman effect has a low photon scattering efficiency since only about 1 in 10^7 incoming photons interact inelastically with a molecule. The Raman activity arises from interactions of the electric field of electromagnetic radiation with electrons and when the nuclei start to move at the same time. The incident electromagnetic field will induce an oscillating dipole (μ), which will re-emit (scatter) at the frequency of the dipole oscillation. The light scattered by the induced dipole consists of both Rayleigh (elastic) and Raman (inelastic) scattering. Rayleigh scattering corresponds to scattered light which has exactly the same energy (frequency) as the original incident radiation, whereas the scattering from the light-induced oscillation from the electron cloud is called

Raman scattering. The intensities of Raleigh and Raman scattered light is directly proportional to the number of molecules exposed to the electromagnetic radiation. In Raman scattering, the incident photon causes the energy of the molecule to increase from ground state to the 'virtual state' and form a complex. This complex formation is very short lived and not stable, and the energy is released as scattered radiation. Hence, the Raman radiation is shifted in frequency (energy) from the frequency of the incident radiation.

A simple classical electromagnetic description of Raman scattering can be used to obtain a basic understanding of the scattering properties of molecules. The simplest way to understand the Raman mechanism is to use an energy level diagram as shown in Fig.1-2. This energy level diagram illustrates that the energy difference between the scattered photons and the incident photons occurs as the result of coupling between the incident radiation and the quantized states of the scattering molecule. The energy difference between the incident and scattered photons is represented by arrows of different lengths. Incident photons either lose energy (Stokes shift) or gain energy (anti Stokes shift) when they interact with a target molecule. Generally, the intensity of the anti-Stokes Raman spectrum is weaker than the Stokes-shifted spectrum, as anti-Stokes scattering occurs from the excited states ($v=1$). According to the Boltzmann distribution these are less populated than the ground states ($v=0$) at room temperature. In general, Raman scattering is usually assumed to be Stokes shifted Raman scattering.

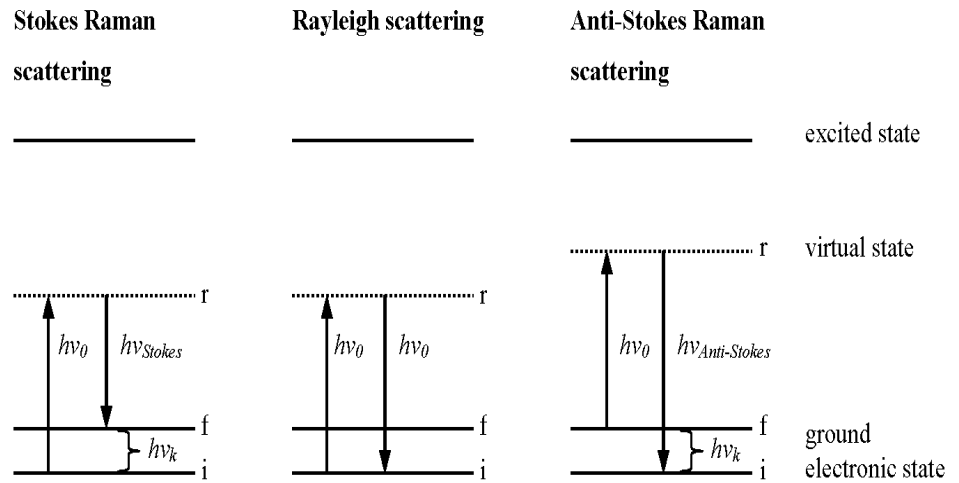


Figure 1-2. Energy level diagram showing the basic transitions involved in Raman scattering of a vibrational energy level of $h\nu_k$, when excited by energy of $h\nu_0$. The virtual state is lower in energy than a real electronic transition.

1.3.1.1 Theoretical Overview

The classical treatment of Raman scattering is based on the concept that scattered light is generated by oscillating electric dipoles induced by the electric field of incident radiation. When electromagnetic radiation is incident upon a molecule, the induced electric field is described by the following equation:

$$E = E_0 \cos 2\pi\nu_0 t \quad (13)$$

where E is the time-dependent amplitude, E_0 is the maximum amplitude, and ν_0 is the frequency of the laser light. When this field interacts with a molecule, it induces a dipole μ such that

$$\mu = \alpha E = \alpha E_0 \cos 2\pi\nu t \quad (14)$$

where α is a constant proportionality (3 x 3 tensor) called polarizability. The molecular polarizability depends on the cloud of electrons surrounding the central nucleus, that changes with normal coordinates during the vibrations of a molecule. According to classical electromagnetic theory, a dipole oscillating with frequency ν emits radiation of this frequency, with an intensity given by⁵⁰:

$$I_R = \frac{16\nu^4}{3c^3} \nu^4 \mu_0^2 \quad (15)$$

Where μ_0 is the amplitude of μ . In equation 15, the scattered light has the same frequency as the incident. The induced dipole moment in equation 15 can be written in terms of Cartesian components if we restrict our discussion to the linear term of the equation. The three forms of the linear equations are as follows:

$$\begin{aligned} \mu_x &= \alpha_{xx} E_x + \alpha_{xy} E_y + \alpha_{xz} E_z \\ \mu_y &= \alpha_{yx} E_x + \alpha_{yy} E_y + \alpha_{yz} E_z \\ \mu_z &= \alpha_{zx} E_x + \alpha_{zy} E_y + \alpha_{zz} E_z \end{aligned} \quad (16)$$

where α_{ij} are the components of polarizability of the molecule, and the first subscript i refer to the direction of the induced dipole in the molecule, and the second subscript j refer to the polarization of the incident light. The above equation can be rewritten as a matrix equation as $\mu = \alpha E$. Thus, the polarizability of the molecule is a tensor.

$$\begin{bmatrix} \mu_x \\ \mu_y \\ \mu_z \end{bmatrix} = \begin{bmatrix} \alpha_{xx} & \alpha_{xy} & \alpha_{xz} \\ \alpha_{yx} & \alpha_{yy} & \alpha_{yz} \\ \alpha_{zx} & \alpha_{zy} & \alpha_{zz} \end{bmatrix} \begin{bmatrix} E_x \\ E_y \\ E_z \end{bmatrix} \quad (17)$$

For almost every case, the polarizability tensor can be described by a real symmetric matrix where $\alpha_{ij} = \alpha_{ji}$, etc. Thus it has at most 6 independent components: 3 diagonal and 3 off-diagonal. This matrix is necessarily symmetric only in the case of non-resonant Raman scattering.

Now let the scattering body be not just a polarizable sphere but possessing vibrational modes of its own; the normal mode Q is described by

$$Q_k = Q_k^0 \cos 2\pi\nu_k t \quad (18)$$

The modulation of the polarizability of a molecule is affected by the oscillation of the normal modes, and can be written as

$$\alpha = \alpha_0 + \left(\frac{\partial \alpha}{\partial Q_k^0} \right) Q_k + \text{Higher order terms} \quad (19)$$

Here Q_k represent the normal coordinate and α_0 is a constant. Then the molecule shows an induced dipole moment when equation 19 is multiply by E

$$\alpha E = \mu = \alpha_0 E + \left(\frac{\partial \alpha}{\partial Q_k^0} \right) Q_k E \quad (20)$$

The expression for μ becomes

$$\mu = \alpha_0 E_0 \cos 2\pi\nu t + E_0 Q_k^0 \left(\frac{\partial \alpha}{\partial \mu_k} \right) [\cos 2\pi\nu t + \cos 2\pi\nu_k t] \quad (21)$$

Finally using the trigonometric identity for the product of two cosines, equation 1.9 can be rewritten as follows:

$$\mu = \alpha_0 E_0 \cos 2\pi\nu t + E_0 Q_k^0 \left(\frac{\partial \alpha}{\partial \mu_k} \right) [\cos 2\pi(\nu + \nu_k) t + \cos 2\pi(\nu - \nu_k) t] \quad (22)$$

Therefore, equation 22 shows that when a molecule vibrates with frequency ν_k , the induced dipole oscillates not only with frequency ν_0 but also with two more frequencies. The above three terms of equation 22 represent the three major phenomena observed in a Raman spectroscopy experiment. The first term in equation 22, the radiation scattered at the frequency ν_0 (the Rayleigh scattering) and is a coherent type of scattering since it is in phase with the incident radiation. The second term of frequency $\nu + \nu_k$ is anti-Stokes Raman scattering and the third term is Stokes Raman scattering (Fig. 1-2). For a transition to be observed, it is clear from equation 22 that those vibrations for which $\alpha'_k = 0$, are inactive in Raman scattering, and those normal vibrations for which at least one element of α'_k differs from zero, are Raman active^{50-52, 56} :

$$\alpha'_{ij}_k = \left(\frac{\partial \alpha_{ij}}{\partial Q_k} \right)_0 \neq 0 \quad (23)$$

Raman scattering can be described both in terms of ‘classical theory’ and ‘Quantum theory’. The classical theory is based on the wave theory of light and it doesn’t take into account the quantized nature of vibrations thus fails to

account for the presence of anharmonicity. Therefore, the better description of anharmonicity is attained with the Morse potential (Fig 1-2). A more thorough discussion of quantum theory expression is beyond the scope of this thesis , but can be found elsewhere ^{57, 58}. The inharmonicity further describes the vibrational modes of the overtones and combinations.

1.4 Thesis Objectives and Overview

The overall objective of this thesis was investigation and characterization of protein and protein-drug interaction using two completely different techniques (CIEF and spectroscopy) and adapt the high performance Raman spectrometer developed by P&P Optica® Inc. for liquid core waveguide (LCW) experimental configuration . Accordingly, chapters 2 and 3 focus on the development and application of high performance Raman spectrometer based on VPH (volume phase holographic) grating. Chapter 2 discusses the novelty and the overall optical components configuration of the system and chapter 3 describes application of LCW- Raman spectroscopy (RS) and successful implementation of LCW cell for the Raman system. Chapters 4 and 5 describe the application and result of CIEF and CIEF with Fluorescence detection for the investigation and characterization of protein and protein-ligand interaction. Finally, conclusions the future directions are drawn in chapter 7. The development and the applications of the two dimensional separation technique to determine the diffusion coefficient, molecular weight and *pI* of polypeptide and protein are discussed in Chapter 6.

CHAPTER 2

INEXPENSIVE AND HIGH PERFORMANCE RAMAN SPECTROMETRY USING VOLUME-PHASE HOLOGRAPHIC DIFFRACTION GRATING

2.1 Introduction

Raman spectrometry using a volume-phase holographic (VPH) diffraction grating is well suited for providing real-time quantitative analyses of chemical compositions in gas, liquid and solid mixtures, albeit usually with only modest sensitivity, limited by the low Raman scattering cross sections of most substances. The technique measures the vibrational frequencies of molecules as related to their molecular structures. Raman spectra provide both the unique fingerprints and quantitative information of the molecules present in a sample under examination. Laser Raman spectrometry is particularly advantageous for monitoring samples because of its excellent differentiation among species compared with techniques of comparable sensitivity such as mass spectrometry and gas chromatography.

This versatile technique has been frequently applied for the investigation of molecular species. When compared with conventional reagent-based analytical techniques, the Raman technique offers the advantages of speed and low operation cost over the long term. Thanks to advances in technology during recent years, primarily the fast development of a sensitive detector, notch filter, inexpensive lasers and new data analysis software, Raman spectroscopy has become widely

used in many scientific disciplines, especially in pharmaceutical, biological and chemical research. Over the past 10 years, Raman spectroscopy has gained increasing prominence as a quantitative tool for the analysis of biological samples. The technique is regularly used for identification, characterization and investigation of new chemical substances or pharmaceutically active compounds. Raman measurements of metabolites and therapeutic drugs were performed in solutions of water or single solvents. However, a few drawbacks make the conventional Raman systems impractical in clinical practice. For such analytes, the signal acquisition time must be longer since Raman scattering is a weak phenomenon. The other obstacle is the small concentration of desired analyte relative to the background spectra. Fluorescence in particular creates a problem, and thus, vigorous sample processing is required to remove the interferences.

Finally, for quantitative measurements, reproducible laser delivery is required for consistent data. Thus, the quest for building a simple, portable, high resolution, user-friendly configuration with broader applications and flexibility for other possible configurations has been a driving force in the development of a better Raman system.

In this chapter, we discuss the design and implementation of a new Raman system with a VPH grating-based Raman spectrometer, as a possible solution to overcome the aforementioned problems. The present technique differs from commercial Raman instruments, because it uses less expensive and high-quality optical components, and the system incorporates a more versatile optical design, in which the focus of the Raman excitation laser may be independently aligned to the reference window (integrated cell) and the sample.

The system ensures freedom from daily adjustment and alignment of the optical components. Moreover, this method requires no special sample preparation and is compatible with a high-speed analysis subtraction procedure, which may be conveniently used to both calibrate the sample and remove background peaks from the sample spectrum. Thus, this combination of hardware and software promises to be widely applicable in a variety of academic, industrial and chemical analysis applications.

Finally, the research described here has been performed at the P&P Optica Inc Laboratory. Several aspects of this study have been supported by collaboration with this company. The VPH grating-based Raman spectrometer has developed by P&P Optica Inc., which is based in Kitchener, Ontario, and the company is based around the technical expertise and experience of Dr. Pawluczyk. Dr. Pawluczyk is a senior scientist and a pioneer with an extensive research and academic experience in the field of modern optics. He is the inventor of 30 high quality patents¹⁻⁴ and the author of 90 scientific journal articles. Our group has been benefitted from the technology and expertise the company provides through our research collaboration. This collaboration represents a big step forward for our labs and lines up with our focus on continuous improvement of our spectroscopy division and positively impacts the effectiveness and quality of our research.

P&P Optica Inc, develops customized spectrometers for a variety of applications, primarily compact and inexpensive instruments. This small company with an innovative work environment placed a strong emphasis on

working together and sharing ideas and knowledge. Exploring diverse areas as mathematical modeling of physical processes, signal and image processing. The company also provides consulting support, maintains facilities for customer support or local follow up as needed.

2.2 Experimental

2.2.1 Outline of the new instrument

A schematic of the high-performance Raman spectrometer is shown in Fig. 2-1. It was designed to measure Raman spectra and fluorescence emission. The diagram illustrates the schematic and key components of the Raman spectrometer system equipped with a VPH diffraction-grating combined with refractive optics. The system consists of three main parts: (1) the spectrometer, which includes the VPH grating, illumination optics and focusing optics, (2) laser filter and detector, (3) integrating cavity cell¹ which is designed using Teflon to hold the sample. Each of the major components of a VPH-based Raman spectrometer shown in Fig. 2-1 is discussed separately in the following paragraphs, followed by a discussion of the application of the system.

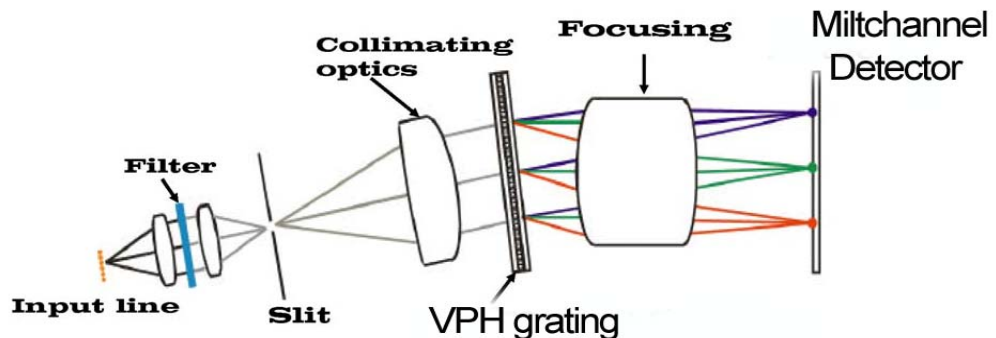


Figure 2-1. Schematic of VPH-based line imaging / multichannel spectrometer^{3, 5, 6}.

In simple design (Fig.2-1), light from a continuous wave (CW) argon ion laser ($\lambda = 488 \text{ nm}$, Cyonics) and a diode laser operating at 785 nm is directed at the sample holder (integrating cavity cell) using an optical fibre (0.2 mm core diameter). Two optical fibres are used to direct and collect the laser radiation from the sample holder. The use of fibre optics for light transmission has several advantages. The excitation radiation can be efficiently coupled into a single fibre that will efficiently transport the photons to the. The Teflon-based integrating cavity cell is constructed in such a way that both fibres are connected to the same cell for the excitation and collection of photons that are scattered from the sample. The cell also allows Raman-scattered light from every position from the sample to enter the collecting optical fibre. Both ends of the fibres are connected to an FC/PC connector to simplify the connections to the laser and to the sample holder. This also provides stability for the optical fibres from the mechanical movement of the sample holder. The fibres in the bundle are also arranged linearly at the entrance of the spectrograph, thereby allowing the Raman-scattered light to be focused on the slit. This is an important part of the instrumental configuration because the intensity of the scattered light is maintained. This may also be one of the major reasons for problems that create distortions in the spectra, thus resulting in poor reproducibility if configured improperly.

The refractive optics specifically designed to produce a straight image of the slit ($10 \text{ }\mu\text{m}$) for each wavelength and straight spectral line for each point of

the slit. The scattered light then passes through an entrance slit and disperses on a collimating mirror. Each point at the entrance slit creates a separate spectrum, which registers on a separate row of a detector array. For instance, if multiple fibres are placed along the slit, the spectrometer provides a separate spectrum for each fibre. The collimated beam then strikes the VPH grating, which is close because of the collimating optics. The VPH grating is transmission based. For the collimating optics image, the input slit is positioned in such a way that monochromatic images of each point of the slit are produced with minimal aberrations at the detector end, allowing for high spatial and spectral resolution. In most CCD-based spectrometers, such a configuration is absent.

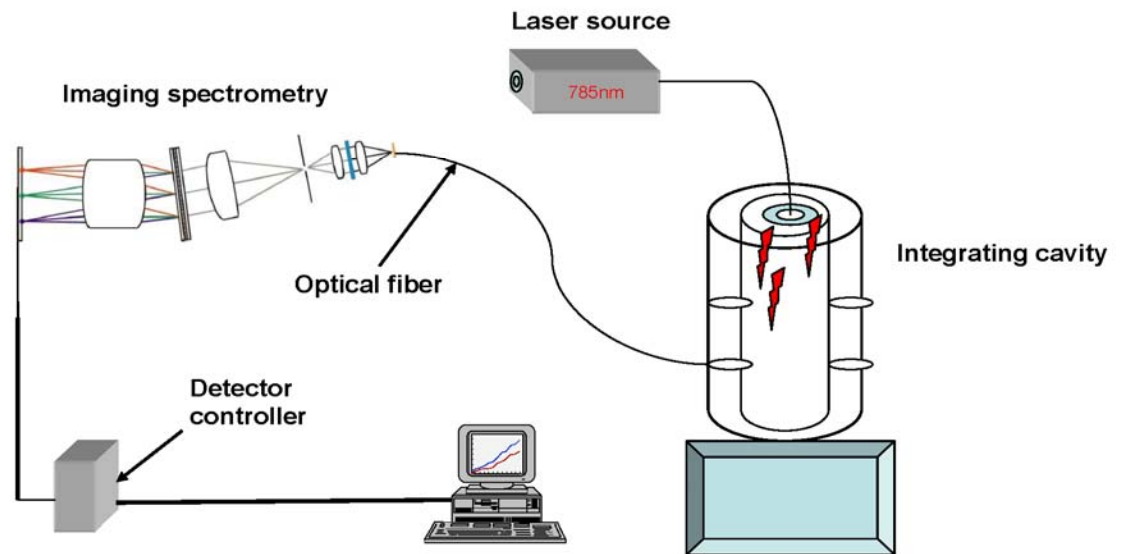


Figure 2-2. The schematic diagram of Raman spectrometer system using VPH-based grating.

The excitation sources are a CW argon ion laser ($\lambda = 488 \text{ nm}$, Cyonics) and a diode laser operating at 785 nm at 10-100 mW laser power. The laser intensity is adjusted depending on the power requirement. For data consistency, laser power is periodically measured at the sample using a LaserCheck (COHEREnT) pocket power meter.

2.2.1.1 Volume phase holographic (VPH) diffraction grating

In the modern information age, it has become very important to acquire data rapidly, especially in the optical communication field, where high-speed spectral analysis is needed. New applications require that instruments are always increasing in efficiency, reduce size, bandwidth, wavefront and thermal behaviour. Usually, an optical dispersion system, such as a monochromator, is used in experiments. The optical dispersion element, a grating or prism, will be mechanically rotated continuously or in very fine steps to scan the wavelength and achieve high spectral resolution in the measurement. The production method of most gratings is either a process involving the mechanical scratching of the surface of a substrate or exposure of a photoresist layer deposited on a substrate (glass or Perspex), where the interference pattern produced by two coherent light beams is used to expose the photoresist. Depending on whether the light is reflected from the grooved surface or transmitted through it, the grating is called either a reflection or transmission diffraction grating. The diffraction efficiency or the percentage of light that is angularly separated by the grating partially depend not only by the spatial frequency, and the angle of

incidence of the incoming light and the optical properties of the grating material. In particular, the diffraction efficiency of reflecting relief gratings is determined by the shape of the grooves and the reflectivity of the grating. While efficiency of transmission grating also depend on the shape of the grooves and refractive index of the material, in both cases, the diffraction efficiency also depends strongly on the polarization of the incident light. Another alternative diffraction grating has recently become available through advances in holographic technology. These gratings, called VPH, show superior performance over surface relief gratings in many applications⁷.

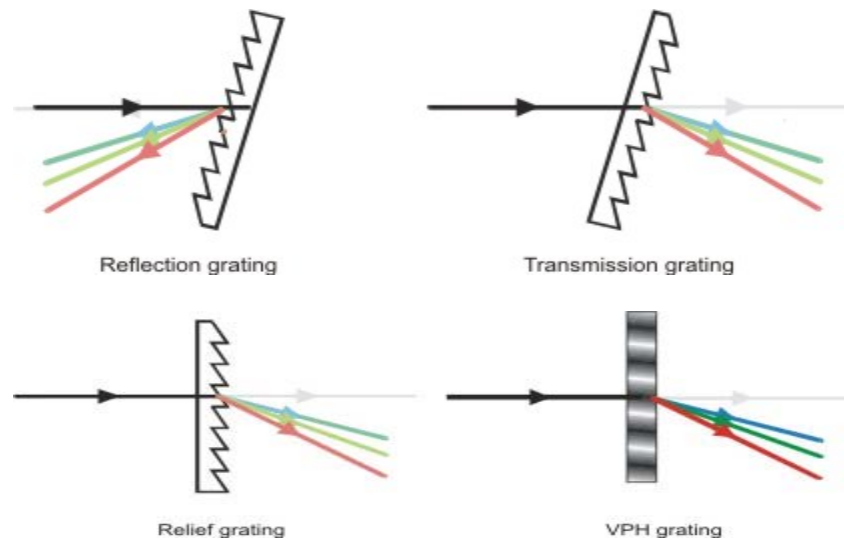


Figure 2-3. Illustration of physical structures of different ⁵ (Reprinted courtesy of P&P Optica Inc) gratings.

A VPH works on a different principle. It involves a sensitive layer (dichromated gelatin, silver halide sensitized gelatin or photopolymer) deposited

on a substrate. The output from a laser source splits into two beams, which cross each other inside the photosensitive media (volume), thus creating an interference pattern in the space shared by both beams. The film then responds to the exposure by a change in the area where the interference is constructive. Then this change in density causes the gel to undergo a slight modulation of its refractive indices. The exposed film goes through a chemical process (depending on the nature of the sensitive layer) to amplify this refractive index modulation. In such a way photosensitive layer exposed to a periodical modulated light intensity becomes a diffraction active structure with periodically modulated refractive index when such a layer exposed to light beam and it acts as diffraction grating separating spectral components of different wavelengths. Usually, the optical layer of a VPH is encapsulated with a hard transparent cover to protect it from environmental damage.

VPH gratings potentially have many advantages over classic surface-relief gratings. The major advantage of VPH over the classic type is the tunability nature, which allows more versatility with a single dispersive element than achieved with classical gratings,⁵ resulting in the desired wavelength being observed with the desired dispersion. Additionally, VPH grating structures can be stacked to produce complex gratings capable of directing the diffracted light in ways that classical gratings cannot. Performance parameters include diffraction efficiency, spectral coverage and angular coverage, etc. which are listed in Table 2-1.

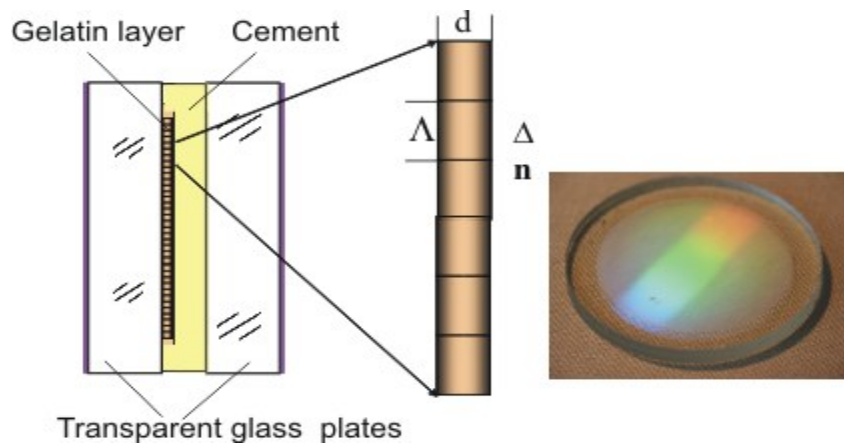


Figure 2-4. Configuration of an assembled VPH grating.

Table 2-1. Comparison of VPH and standard relief gratings (HRR) ⁵

Tested Parameter	Performance	
	HRR	VPH
Efficiency, narrow band (tens of nm)	~ 90%	Close to 100%
Average efficiency, (one octave)	20% - 30%	> 60%
Band and efficiency product	Hardly controlled	Well controlled
Efficiency, as a $f(\text{dispersion})$	Decreasing	Increasing
Polarization dependency	Strong	Weak
Efficiency curve $f(\text{wavelength})$	Irregular curve	Regular
Scattered light	At detectable limit	Below detectable limit
Focusing ability (no additional optics)	Over the entire spectral range	Limited capabilities
Imaging quality, focusing grating	Strongly astigmatic	Astigmatic
Imaging quality, plane grating	Diffraction limited	Diffraction limited
Work in high dispersion Littrow configuration without additional optics	Possible in whole spectral range	In limited part of visible and short NIR range
Work in high dispersion Littrow configuration with additional optics	Limited efficiency in whole spectral range	Highly efficient in whole spectral range
Multiple function in a single element	Impossible	Possible

Stacking of multiplicity of elements	Impossible	Possible
Surface protection	Impossible	Can be fully protected
Temperature range	Standard	Up to above 100°C
Humidity	Non-condensing	Boiling water (with surface protection)
Power resistant	Limited	High, depends on spectral range
Production technology	Mature, well established	Limited number of experienced companies
Pricing	Established price	Higher, low volume production
Price of imaging gratings	High	Competitive
Price of plane gratings (replica)	Low	Higher (if protected)

The experimental set up is shown in Fig 2.2. The excitation source is 600 mW semi-conductor diode (785nm) CW lasers. The laser beam is coupled with an optical fibre coupler on one side of the Teflon tube. The scattered photon flux is collected and collimated by three different mirrors and directed to the VPH. The focusing optics located before the detector focus the scattered photons on the detector. The detector (Princeton) is described below. The instrument was designed by P&P Optica Inc.⁵

2.2.1.2 Detector

The light spatially dispersed by grating, and collected by focusing optics and recorded on CCD (Princeton Instrument/Acton, Model PIXIS 256). The CCD is cooled thermoelectrically down to -75⁰C to provide the lowest dark current (~0.006 e⁻pixel sec⁻¹). This high-performance detector provides excellent response from UV to NIR. The back-illuminated and deep depletion with anti-etaloning technology gives the detector additional sensitivity in the near IR

region while the special coating for UV allows use in the deep UV region (Fig 2-5). In an imaging array with 1024 x 256 pixels, each pixel has a dimension of 26 μm x 26 μm .

A collection time of 10 to 20 s with a laser power of 150 mW or 200 mW at the sample are used in all Raman measurements. Standard computer software (Winspec, Princeton Instruments, Inc.) is used for data acquisition and Octave (a free open source software) is used for spectral subtraction and normalization.⁸ Raman frequency shifts are calibrated using a cubic polynomial fit to neon emission lines.

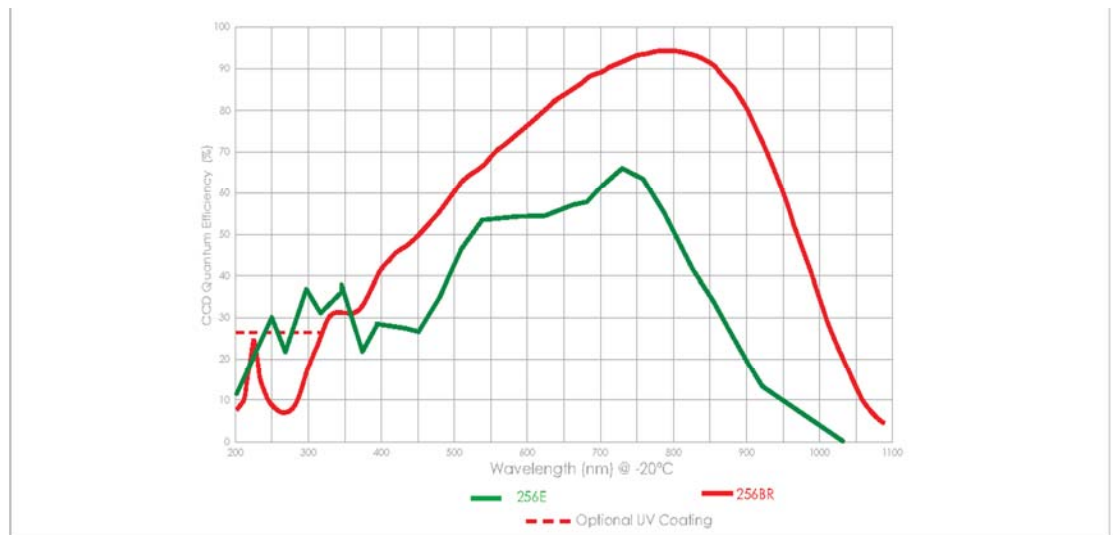


Figure 2-5. Quantum efficiency curve of a deep depleted CCD detector.

Reprinted courtesy of Princeton Instruments.

2.2.1.3 System Calibration

When using an excitation laser with a fixed frequency, such as the 785 nm laser used in this work, it is more convenient to use a standard emission source such as a neon lamp, which has numerous sharp lines of known wavelength in the Raman Stokes shifted spectral region. We have fit several such atomic transitions lines to a Gaussian peak shape in order to accurately determine the peak position of each line with a resolution of better than one CCD pixel. The resulting values of pixel peak position are plotted against the known wavelengths of each neon line and fit to a cubic polynomial in order to determine the pixel-to-wavelength calibration function. The Raman shift frequency at each CCD pixel is obtained by converting the wavelengths corresponding to each pixel to frequencies and then subtracting the frequency of the narrow spectral band semi-conductor ($12,738.85 \text{ cm}^{-1}$) laser.

2.2.1.4 Laser line and edge pass filters

The laser radiation is directed toward the slit by the use of a Laser line Filter (Raman filter 785 nm, Iridian Spectral Technology Ltd., Ottawa, Canada). This filter performs two functions: First, it narrow emission band of Raman excited laser line and cleans up the beam by blocking wavelengths, which are at fluorescence wavelengths. Secondly, this filter also provides further filtering of ambient and plasma light. The instrument also equipped with a long pass band filter (edge pass filter) which provide a sharp cut-off either above or below of

785 nm laser line. This filter is useful to isolate specific regions of the spectrum. The transmission wavelengths (794.5-1200nm) is 90%.

2.2.1.5 Integrating cavity cell

Because the Raman signal is scattered in all directions, for weak scattering one needs to use a sample holder that can minimize photon loss. For these reasons, special cylindrical-shaped sample holders made from a Teflon material were built.

2.2.1.6 Data collection

Tylenol spectra were collected using a 100-200 mW solid-state excitation laser with 10 to 20 sec integration time.

2.2.1.7 Data processing

First, high quality Raman spectra are collected before and after placing the sample into the integrating cavity cell. The spectrum obtained with an empty Teflon tube represents the Teflon reference spectrum. The spectrum obtained from the filled tube and the cell contains both sample and Teflon spectral features. The Octave software is subsequently used to subtract the Teflon reference spectrum from the mixed spectrum. After Teflon subtraction, the sample spectral intensity is normalized by dividing the sample spectrum by an appropriate coefficient, which represents the Teflon window intensity. Thus, the resulting sample spectrum contains no Teflon spectral features and is normalized to correct for any changes in either laser intensity or collection efficiency of the Raman spectrometer.

In addition, a measurement was made on the CCD full pixels at room temperature to monitor the readout noise from the CCD. Indeed, a dark noise collected without light displayed fluctuations in the baseline signal. This noise is very common in scientific instruments and increases as the exposure time is longer. During the data processing, the noise spectra from the CCD were subtracted and corrected from the collected spectra of the analytes.

2.2.2 Materials and Chemicals

Commercial acetaminophen-based tablets were purchased from different drug stores. Tylenol, Pharmasave, Rexall, Compliments, Life Brand and Exact regular strength tablets (manufactured by McNeil consumer healthcare) were purchased from Shoppers Drug Mart Inc. All the samples were used without further treatment.

2.2.3 Sample preparation

Tablets containing acetaminophen (Tylenol, Pharmasave, Rexall, Compliments, Life Brand and Exact regular strength) were prepared using a direct blend technique. The target tablet mass was 0.36 g. The coating of some of the tablets was systematically removed using a surgical blade. The samples mass, manufacturer, chemical composition and content of acetaminophen are given in Table 2-3. All samples were used without further treatment except that the coating of some of the tablets was removed to minimize the complexity of the Raman spectra.

2.2.4 Theoretical calculation

Theoretical calculations were performed using density functional theory (DFT) of Becke's three-parameter functional including the correlations functional of Lee, Yang, and Parr (B3LYP)⁸ with Lanl2dz basis set, to help the assignment of the Raman spectral peaks of acetaminophen. DFT theory describes a class of methods in which exchange and correlation contributions have been formulated based on solution of the Schrodnger Equaation for a free-electron gas. The predicted wavenumber values have to be scaled with a general scaling factor (0.96)⁹ to adjust observed experimental wavenumber values. It was found that the calculated Raman vibrational wavenumbers are in good agreement with experimental values. The calculations were carried out using Gaussian 03¹⁰ software for Windows.

2.3 Results and Discussion

The application of a high performance Raman spectrometer has been adapted for measuring spectra in the UV, visible and NIR spectral ranges with the implementation of appropriate filters. This spectrometer was demonstrated to have superior stability, simplicity, accuracy, large throughput capacity, cost efficiency and sensitivity comparable to that of a multichannel dispersive commercial Raman spectrometer. Such an imaging system was initially intended to monitor multispectral fluorescence imaging. The laser, filter, laser-focusing lens, VPH grating and detector were initially assembled and aligned to achieve a Raman signal from different Tylenol-based powders. Alignment and

control procedures have been developed to achieve an enhancement of Raman scattering light.

To test the ability of the Raman system, Tylenol tablets were used as a model compound. The detectability of a trace component in different acetaminophen-based Tylenol brands by Raman spectrometry is governed by the Raman-scattering signal from these components which are almost identical in chemical composition and which have observed with the same Raman spectral fingerprints. Table 2-3 shows the chemical composition of the acetaminophen-containing tablets used in this experiment. Acetaminophen has a chemical formula $C_8H_9NO_2$. These tablets were manufactured by a different pharmaceutical company. Visual examination of the spectra collected from all seven samples show similar fingerprints, while minor spectral differences are observed upon closer examination. By analyzing the spectra of all six samples and comparing with the regular Tylenol, it appears that there is a slight difference in the relative Raman shift values.

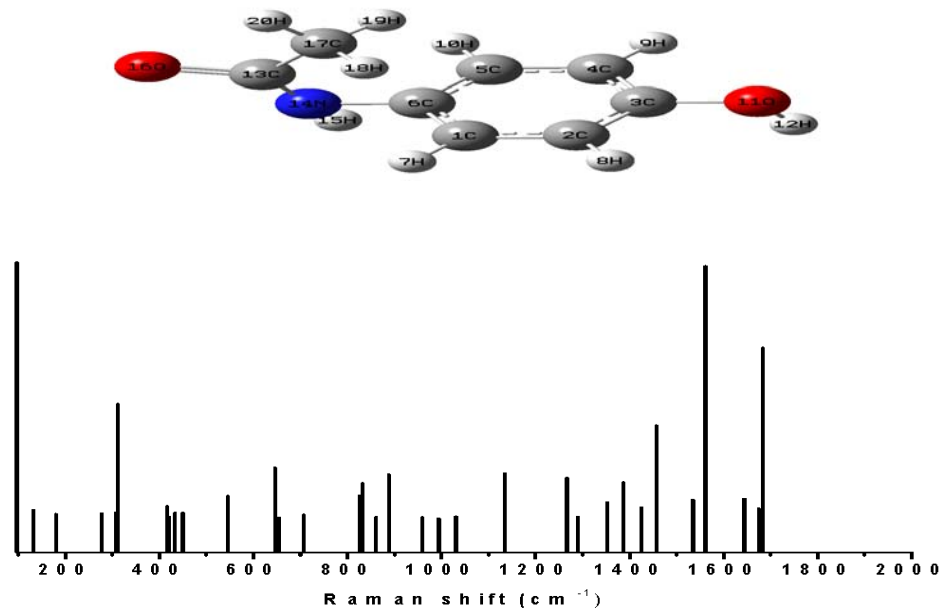


Figure 2-6. The calculated density functional theory (DFT) Raman intensities of Tylenol regular strength and molecular structure.

All of the spectra contain features associated with the solid mixture as well as the spectrum of the integrating cell (Teflon) as shown in Fig 2-9. The Teflon cell spectra were subtracted from that of the Tylenol powder spectra using a software subtraction. Only the spectral region between 250 cm^{-1} and 2000 cm^{-1} was used in implementing the subtraction, as this region contained the major Teflon peaks. Note that there is not much overlap between the Teflon and Tylenol peaks, and so it was very easy to subtract the two spectra accurately. Normalization was performed using the Teflon peak at 724.76 cm^{-1} . Even if the Teflon spectra were very intense; the Tylenol peaks were clearly observable in spite of underlying broad Teflon bands.

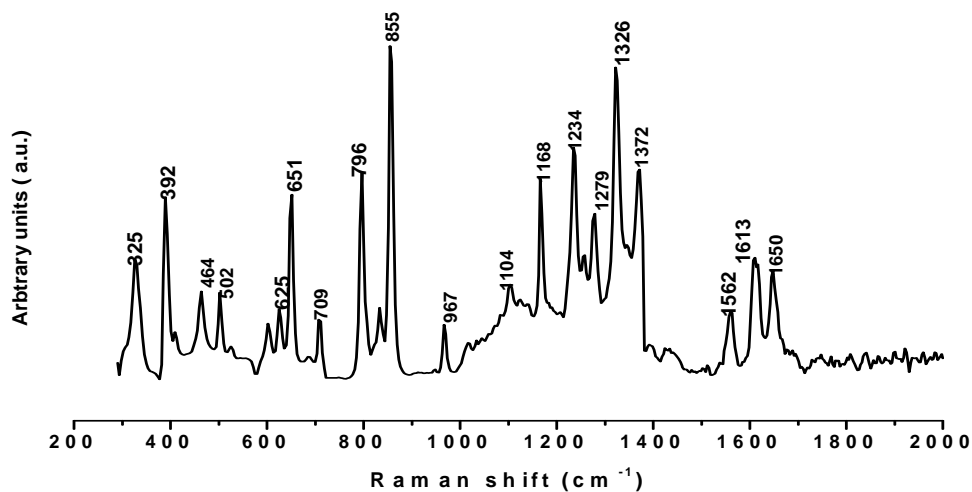


Figure 2-7. Raman spectrum of Tylenol regular strength tablet in the 200 to 2000 cm^{-1} spectral region. The excitation laser line is 785 nm.

Table 2-2 Predicted frequencies and Raman intensities associated with the stretching modes of the OH, NH, and CO chemical functions and the CH stretching modes of the CH_3 group and the phenol ring of acetaminophen in the optimized structure from the DFT- B3LYP methods.

Calculated cm ⁻¹	Intensity KM/mole	Tablet (cm ⁻¹)	Approximated assignment
66.1878	3.0426		Ring deformation
132.0998	12.5642		Ring deformation
179.7619	6.9586		
277.5637	7.7		Ring def, ring CH wagging
307.513	8.9666		
311.7993	169.8838	325	Ring deformation,O-H wagging
416.39	18.5396	392	Ring def
421.2618	2.2959		Ring def
433.1068	8.8299	464	Ring def
450.4276	8.9355	502	Ring dis
545.8999	33.6041		Ring dis
645.9714	75.743	625	Ring def,N-H bending
653.4761	1.8247	651	Ring dis
706.9466	6.047	709	Ring def
825.9316	34.205	796	Ring dis
831.9097	52.7648	832	Ring def,ring C-H bending
861.3466	2.5734	855	Ring dis
888.345	65.6365		Ring C-H bending
958.2629	2.1014	967	Ring C-H antisymmetric str
994.1738	0.2204		
1028.687	1.6904	1016	Ring dis
1030.443	3.2572	1104	Ring C-H antisymmetric str
1134.856	66.9448	1168	Ring breathing
1267.208	60.3871	1258	Ring C-H in phase symmetric stretching
1290.498	3.0471	1279	Ring breathing,N-H bending
1353.311	24.2986	1326	Ring C-H antisymmetric C-H stretching
1387.392	53.9112	1372	Ring def, O-H bending stretching
1425.583	16.646	1429	Ring def, C=O bending
1456.476	137.979		Ring C-H wag
1535.364	0.6595		

1560.913	70.1245	1562	Ring def
1643.504	31.3323	1613	Ring def, N-H bending, O-H bending
1674.062	126.1479	1650	Ring def, N-H bending, ring C-H bending
1683.072	63.8111		

- **Def= deformation dis=distortion**
- **str= stretching**
- **Wag=wagging**

The Raman spectrum of acetaminophen-based Tylenol regular is illustrated in Fig 2-7, which shows several bands. An examination of the Raman spectra which excitation laser 785 nm (Figure 2-7) shows a typical Raman spectrum of acetaminophen-based Tylenol tablets. Thus, all of the spectra contain features associated with acetaminophen. Note that the chemical compositions of these tablets are based on this compound and some added additives such as a narcotic. Depending on the brand of a particular tablet, the concentrations of these additives varied from brand to brand. The detailed assignment of all these bands of Tylenol has been made on the basis of the theoretical prediction of acetaminophen (Table 2-2). The assignments of the observed vibrational bands of the title compound are also listed in Table 2-2.

Table 2-3. Tablets that contain acetaminophen-based Tylenol⁵.

Product	Medical ingredients	Non-medicinal ingredients	Manufacturer	Weight of tablet (mg)
TYLENOL Regular Strength Acetaminophen	Acetaminophen (325mg)	Cellulose, corn starch, sodium starch glycolate	McNeil Consumer Healthcare	0.3900
Pharmasave Regular Strength Acetaminophen	Acetaminophen (325mg)	NA	JAMP Pharma Corporation	0.3650
Rexall Regular strength Acetaminophen	Acetaminophen (325mg)	NA	Apotex Inc.	0.3540
Compliments Regular Strength Acetaminophen	Acetaminophen (325mg)	corn starch, providone, stearic acid	Vita Health Product Inc.	0.3600
Life Brand Regular Strength Acetaminophen	Acetaminophen (325mg)	NA	Pharmetics Inc.	0.3622
Exact Regular Strength Acetaminophen	Acetaminophen (325mg)	Pregelatinized corn starch, corn starch, stearic acid, providone	Pharmetics Inc.	0.3633

In the Raman spectrum of acetaminophen, the band which appear at 1649 cm^{-1} is due to the C=O stretching vibrational modes. The band -NH deformation mode occurs near 1612 cm^{-1} , and HN-C=O bend at 1562 cm^{-1} . The band observed at 799 cm^{-1} is attributed to the phenyl ring-stretching mode. Other Raman vibrational modes between 1350 to 1180 cm^{-1} region are due to N-H bending and C-H deformation vibrational modes. All the observed vibrational bands are in close agreement with the reported literature¹¹. However, clear assignments for the other bands are presently uncertain.

The detection capability of our system was determined not only by measuring the Raman spectrum of a single tablet (Tylenol regular), shown in

Fig. 2-8, but also by collecting Raman spectra from two Tylenol tablets from different brands. Since the concentration of acetaminophen is very high in all the tablets, the overall spectral features are dominated by this compound. The Raman spectra measured at room temperature reveal several peaks corresponding to acetaminophen. These spectra underlines the major peaks that are typical Raman vibrational modes of Tylenol.

Raman spectra of the Life Brand and Tylenol regular strength tablets were collected and compared. Fig. 2-7 shows the resulting spectrum containing the typical acetaminophen features. The intense background in the ranges 400 to 1000 cm^{-1} is from the Teflon background. Two different spectral ranges of 400 to 800 cm^{-1} and 1100 to 1500 cm^{-1} are used to evaluate the spectral features of the two tablets. There are two bands absent for the Life Brand tablet at 1143 and 1427 cm^{-1} but they appear in the Tylenol regular strength tablet, demonstrating a minor difference between the two tablets. The other striking observation is the higher intensity observed for the Tylenol regular strength compared to the Life Brand. Note that the observed Raman intensities of the two peaks are very weak, which may give insight into the chemical compositions of the two tablets. In addition, three more peaks at 410, 510 and 1400 cm^{-1} were observed for Life Brand but not for other sample. These results support the high performance sensitivity of the Raman system.

By the same argument, all seven spectra are superimposed and illustrated in Fig 2-9. The Raman features of acetaminophen appear dominant

due to its high concentration in all tablets. Note that the baseline of each spectrum shown in Fig. 2-9 is filtered to a third order polynomial and the resulting baseline model is subtracted from the spectrum to generate the baseline-corrected spectrum. As mentioned earlier, closer examination of the seven spectra reveal a minor difference in intensity, peak area and position observed on the shoulder of the intense peaks near 400, 600 and 800 cm^{-1} (Fig. 2-8). This further demonstrates the hypersensitivity of the Raman system.

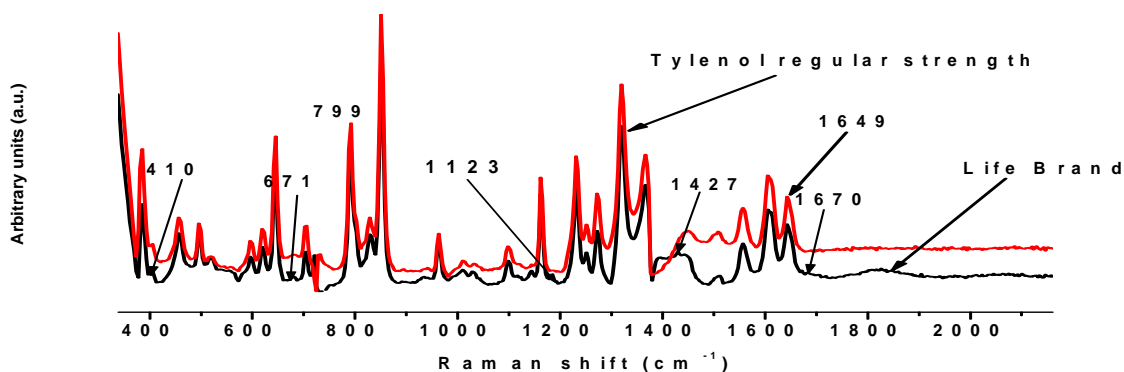


Figure 2-8. Raman spectra of Tylenol regular strength and Life Brand tablets.

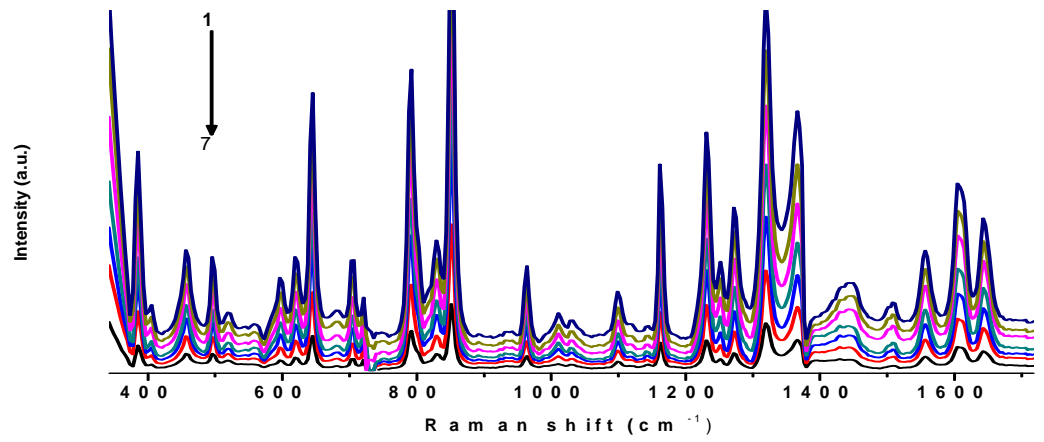


Figure 2-9. Raman spectra of seven acetaminophen-containing Tylenol tablets. ; curves (1-7), Tylenol regular strength, Pharmasave, Rexall, compliment, Life Brand, exact and cold extra.

2.4 Conclusion

High performance Raman spectrometry has been adapted for measuring spectra in visible and NIR spectral ranges. This spectrometer was demonstrated to have superior stability, simplicity, wavenumber accuracy, large throughput, cost efficiency and sensitivity comparable to that of a multichannel dispersive Raman spectrometer. The laser, filter, laser-focusing lens, VPH grating and detector were assembled and aligned to achieve a Raman signal from different acetaminophen-based powders. Alignment and control procedures have been developed to achieve an enhancement of Raman scattering light.

The performance evaluation measurement was performed using Tylenol tablets with minor differences. Thus, this new Raman spectrometer certainly provides various physicochemical properties, which are not obtainable with a commercially available Raman spectrometer. This advantage can be extended to other heterogeneous samples, such as pharmaceuticals or biological samples. However, much work remains to be done before this system can be used for very low analyte concentrations. Thus, in the future, it would be beneficial to perform more experiments in order to gain a better understanding of the system and to improve it. Finally, the results of this study demonstrate the promising future for coupling the Raman system to capillary isoelectric focusing (CIEF) and solid phase micro extraction (SPME) to analyze a wide range of molecules.

CHAPTER 3

APPLICATIONS OF HIGH PERFORMANCE LIQUID-CORE WAVEGUIDE RAMAN SPECTROSCOPY

3.1 Introduction

Since the discovery of light guiding in liquids by Colladon¹, Babinet², and Tyndall³ in the mid 19th century, the phenomenon of liquid-core guiding has attracted attention both in and outside the scientific community. By end of the 20th century, this effect was widely known due to its usage in illuminating fountains⁴. Since then a number of liquid-core fibers, consisting of small diameter glass tubes, were developed with high refractive index solvents. These liquid-core fibers performed well with minimum radiation loss (8dB/km) when near infrared radiation was used⁵.

A liquid-core waveguide (LCW) can be made from an optical grade tubing material, in which the wall of the material has a lower refractive index than the liquid-core material. Under this physical condition, it is possible for light to propagate down into the core of the waveguide and be guided over a significant length. To achieve this effect, light goes through a total internal reflection (TIR) at the interface between the wave guide tubing walls and the sample which flows through the hollow core of the Teflon tube. Such a situation is achieved if the light carrying liquid core is bounded by optically transparent walls that are made of a material with a refractive index (RI) less than that of the liquid of interest. This phenomenon can be explained using Snell's law:

$$n_1 \sin \Theta_1 = n_2 \sin \Theta_2 \quad (1)$$

$$\sin^{-1}(n_{\text{clad}}/n_{\text{core}}) = \Theta_{\text{critical}} \quad \text{or} \quad \sin \Theta_{\text{critical}} = n_{\text{clad}}/n_{\text{core}} \quad (2)$$

where n_2 is the index of the cladding material and n_1 is the index of the fluid-core. According to the above equation, light travelling through the liquid core at an angle less than Θ_{critical} will be trapped in the core resulting in TIR. However, light travelling through the core at higher angles than Θ_{critical} can travel into the cladding and in the core. Furthermore, the propagated light will exit the fiber, if $n > n_{\text{critical}}$ and the angle of refraction of light is greater than Θ_{critical} (Fig3-1). For Teflon AF 2400 ($n=1.29$) and water ($n=1.33$), Θ_c is 14.1° .

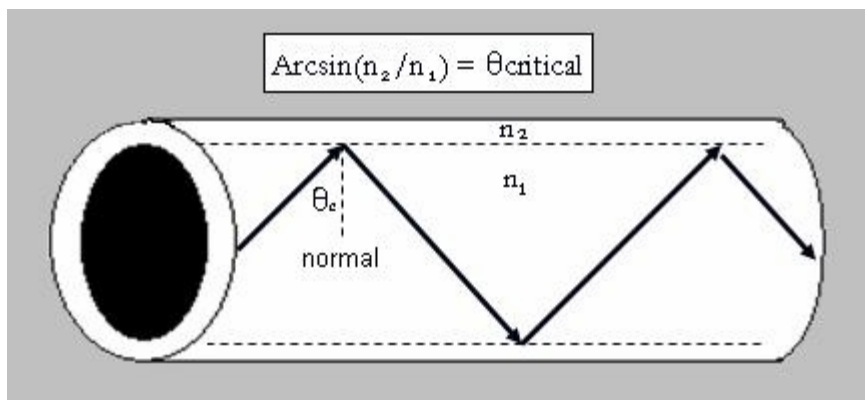


Figure 3-1. Schematics of liquid core optical fibre. The waveguide extends the laser light path length through total internal reflection inside the Teflon tubing.

Most waveguide spectroscopy is performed using plastic capillaries. In addition to their excellent performance, they are extremely flexible and breakage resistant and contain light entirely within the core liquid. Within the

last six years, several liquid core waveguides for use with water have been fabricated from amorphous copolymers such as fluoropolymers 2,2-bis(trifluoromethyl)-4,5-difluoro-1,3-dioxole⁶ and polytetrafluoroethylene (PTFE) and are now commercially available. This later polymer is called by its trade name Teflon AF and has been used as an aqueous-core optical waveguide for signal enhancement due to its low refractive index (RI) (1.29-1.31)⁷, which is slightly lower than that of water (1.33). In recent years, Teflon AF has become a leading polymer with n_d lower than most known materials, which facilitates waveguiding through aqueous media at standard temperature and pressure. The number 2400 refers to the glass transition temperature (T_g) in degrees Celsius. The T_g of AF is 240⁰C and it has $n_d=1.29$. Teflon® AF not only possesses the above listed properties, it is also physically and optically stable and transparent (> 96% transmission) in the spectral range from 200 to 2000 nm⁸. In addition, Teflon AF is chemically resistive and very flexible, so that it can be readily coiled for applications that demand long path lengths.

Teflon-AF 2400 based systems have been widely used for absorbance spectroscopy⁹, fluorescence^{10,11}, liquid chromatography¹², gas chromatography¹³, Raman spectroscopy in long fibers¹⁴⁻¹⁶ and capillary electrophoresis¹⁷. Signals such as Raman or fluorescence are enhanced by LCW due to the ability to excite a greater number of molecules along the path of the laser. Depending on the length of tube and specific application, signals can be collected from the entire volume of the wave guiding region. The main advantages using LCW

with Teflon AF are that high spontaneous Raman intensities can be obtained from a long path with minimum radiation loss from a small volume of sample, and the system does not require complicated optical configurations. In addition, the use of small samples is particularly important for valuable samples in areas such as medical, forensic, biological, and environmental analysis.

The first Raman application using LCW based on Teflon AF 2400 was reported by Altkorn et al.^{14,15}. However, prior to Altkorn's work, Walrafen and Stone used long path liquid core waveguide cells made of PTFE (silicon tube) to characterize benzene and tetrachloroethylene^{18,19}. The spectra collected from the two analytes were of good quality with low noise. Some extra features appeared which had never been observed before. Furthermore, Walrafen and Stone reported an intensification factor of 3000 for benzene in a 15-m fiber, while the intensification factor for tetrachloroethylene performed in a 25-m fiber was 300. Even though excellent enhancement and reproducible data were observed for the above techniques, the system was not immune to a loss of radiation²⁰. These losses were observed because of the extraordinary care the PTFE required when used as a cell for LCW at a later time, Schwab and McCreety performed a similar experiment as Walrafen using a thin-wall glass tube as LCW, attached to a remote spectrometer through a fiber bundle²¹. In this system, they used one fiber brought to the excitation source and 18 parallel fibers for Raman scattering collection. However, more recently, a simple inexpensive Raman spectrometry was used with a simple configuration of two

fibers (one transmitter, one receiver)²². In this configuration, a CCD detector and a diode laser were used for detection and excitation of samples from LCW.

As already mentioned in the previous paragraph, the major advance in LCW-based spectroscopy of aqueous solutions was the introduction of a new amorphous fluoropolymer, Teflon AF. The commercial availability of tubing manufactured from Teflon AF led to a surge in the development of LCW. LCW cells have contributed greatly to enhancing Raman signals as well as several other applications. Raman signals can be observed from liquids forming the high-index core of a light guiding system. If a laser beam is propagating down a liquid core fiber, all the Raman photons emitted into a certain solid angle will be similarly propagated. However, photons emitted by impurities also propagate down the fiber and contribute to the overall collected signals. In principle, it is possible to overcome such extraneous signals by using good data processing software. When light propagates through the LCW fiber, some light is scattered outside the TIR acceptance angle, and so it does not reach the detector. The light scattered within the capillary TIR and guided within the capillary significantly contributes to the Raman signal.

Raman spectroscopy has been employed extensively to study the conformation of the disulphide bridge in proteins and peptides, because the frequency of the S-S stretching mode of the S-S bridge is sensitive to its

conformations²³. These disulphide pairs are located between helical segments of domains.

The investigation of the disulphide bridges of human serum albumin (HSA) is our principal target, because the S-S stretching modes are very sensitive to the conformational change of HSA. X-ray crystallographic studies of HSA confirm that all the disulphide bonds are *gauche-gauche-gauche* (*ggg*) conformation.²⁴ However, other conformers were reported for bovine serum albumin (BSA) such as *ggg* (SS stretching band at 505 cm⁻¹) and *gauche-gauche-trans* (*ggt*) 520 cm⁻¹²⁵. In this study, a strong Raman band at 492-431 cm⁻¹, assigned to *ggg* geometry, predominated in the Cys-SS-Cys residues, while weaker features at 454, 507 and 518cm⁻¹ indicate other conformations of the CCSSCC chains, respectively having *tgt* and *ggt* geometry.

In the present study, the structural change of HSA in solutions has been investigated by LCW-Raman spectroscopy in order to explore whether the interaction of HSA with oxaliplatin is responsible for the breakage of the S-S bridge and thus the conformational change of the protein structure.

3.2 Experimental

3.2.1 Apparatus

3.2.1.1 Raman Instrumentation

3.2.1.1.1 Raman Spectroscopy using 632.8nm excitation

Raman spectra were recorded on a Dilor-Jobin Yvon-Spex HR 800 Raman spectrometer, equipped with an Olympus BX 40 system microscope with 10, 50 and 100x objectives (Fig.3-2). A He–Ne laser system with excitation line at 632.8 nm and an excitation power of 10-20mW was used in the measurements. Spectra shown below are the accumulated averages of 10–15 exposures of 5-10 seconds each at room temperature 21–23 °C. Average spectra were smoothed by a 5 cm⁻¹ filter and were corrected by a polynomial baseline using LabSpec (Dilor-Jobin Yvon-Spex, France) software. The second derivative analysis of Raman spectra was made using Origin 8.0 software (Microcal Origin, USA). The obtained second derivatives of the spectra were applied to detect the positions of overlapping bands. Some spectral regions were analysed by the normalised least-squares curve-fitting procedure (PeakFit module of Origin 8.0) using multiple Voigt (Gaussian-Lorentzian mix) curves.

3.2.1.1.2 LCW sample delivery

A small amount of sample was transferred into a capillary tube, which was placed on the stage of the microscope. With the help of an internal light, it was possible to focus the microscope on the liquid in the centre of the capillary. To

acquire a spectrum, the internal light, and all other ambient light, was shut off, and laser light was then allowed to strike the sample.

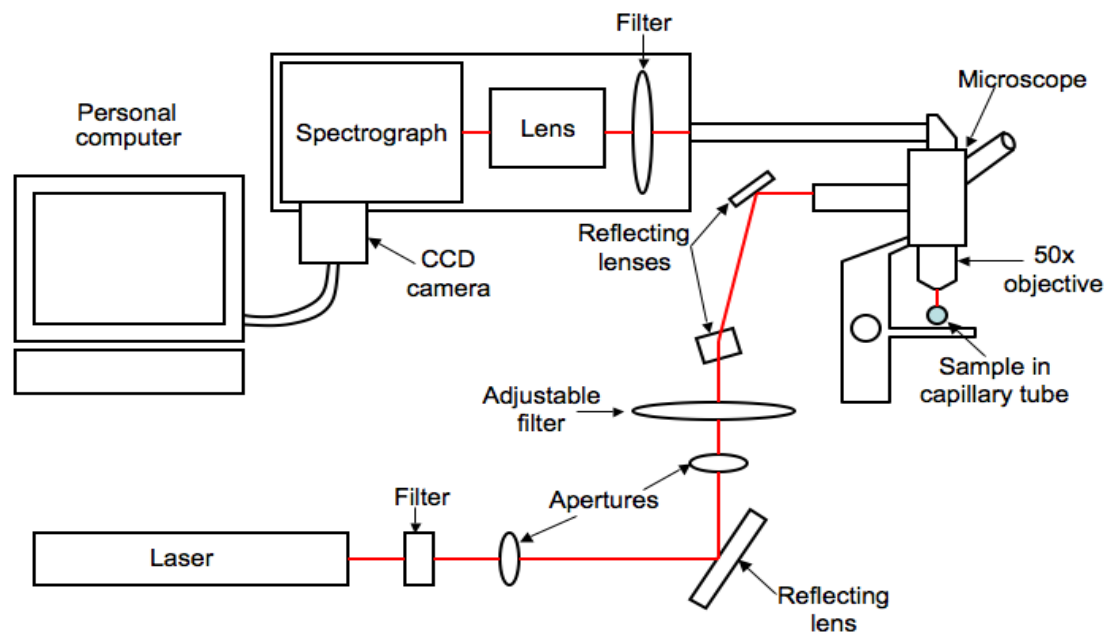


Figure 3-2. Schematic diagram of Raman system equipped with 632nm excitation line.

3.2.1.1.3 LCW-RS system from a distance of 70 cm

Two different instrumental configurations were designed and are shown in Fig.3-3 and 3-4. Both figures illustrate the schematic and key components of the LCW-RS system. The system consists of three main parts, namely, the spectrometer which includes the volume-phase holographic (VPH), transmission lenses, laser filter and detector, LCW cartridge, which is designed using Teflon AF (150 μm inside diameter (i.d.) x 360 μm outside diameter (o.d.) tube, and the optical fiber coupler containing the laser filter and the two laser sources. In the first configuration, a single mode polarization-maintaining optical fiber that was suited for $\lambda=785$ nm was polished and directly inserted

into the Teflon tube. A laser beam, from a continuous wave (CW) Argon ion laser ($\lambda=488$ nm, Cyonics) was launched into the free-space fiber coupler (KT110), which is equipped with a focusing aspheric lens (C230TM), a laser line filter and iris diaphragm. The beam from the laser is sent through a narrowband interference filter which cleans up the beam by blocking emission line of laser plasma tubes. The aspheric lens is selected so that it gives the best result for visible and near IR lasers that have beam diameters around 1 mm. The iris diaphragm is used on the input end of the coupler to ensure laser beam transmission through the optical fiber. By adjustment of the iris, the laser beam can be centered on the aperture of the FC/PC (fibre channel/physical contact) receptacle. Since the fiber coupler has an optical axis that is 3.7", the height of the laser beam was setup from 3.5" to 3.9" above the surface of the optical table. Note that only one end of the optical fiber is connected to the FC/PC connector to simplify the connections to the laser. This coupler is equipped with an XYZ translator which is movable and threaded at the center section of the device. The XYZ translator which hold the LCW cartridge, align the fibre optic coupler in three dimensions to fit the laser beam in such a way to obtain an optimum coupling.

The laser beam guided by the optical fiber is injected into the Teflon AF tube coupled with the optical fiber coupler to illuminate the Teflon AF (50 mm) cartridge that is mounted on the XYZ translational stage. The schematic description of the sample cartridge can be found in section 3.2.5 of this chapter. However, for this configuration, the sample was placed 80 cm from the entrance

slit of the spectrometer. For Raman signal collection, the entrance of the spectrometer is equipped with a lens with focal length of 105 mm.

For the second instrumental configuration (Fig. 3-4), a short Teflon tube as the LCW was attached to a simple two-fiber (one transmitter, one receiver) for Raman signal collection. The attached optical fiber was connected to a FC/PC connector and transmitted the scattered signal from a small area from the Teflon tube to the entrance of the spectrometer.

3.2.2 Data collection

Spectra are recorded with a Princeton Instrument/Acton Model Pixis 256 camera (1024 x 256 array) a collection time of 10- 20 s with a laser power of 10 to 20 mW at the sample are used in all Raman measurements. Standard computer software (Winspec, Princeton Instruments, Inc.) is used for data acquisition, and Octave (a free open source software) is used for spectral subtraction and normalization.⁸ Raman frequency shifts are calibrated using a cubic polynomial fit to Ar-Hg emission lines.

3.2.3 System Calibration

When using an excitation laser with a fixed frequency, such as the 785 nm laser used in this work, it is more convenient to use a standard emission source such as an Ar-Hg, which has numerous sharp lines of known wavelength in the Raman shift spectral region. We have fitted several such atomic transitions lines to a Gaussian peak shape in order to accurately determine the peak position of each line, with a resolution of better than one CCD pixel. The resulting values of pixel peak position are plotted against the known wavelengths of each neon

line and fit to a cubic polynomial in order to determine the pixel-to-wavelength calibration function. The Raman shift frequency at each CCD pixel is obtained by converting the wavelengths corresponding to each pixel to wavenumbers and then subtracting the wavenumber of the He–Ne laser line 632.8 nm ($15,802\text{ cm}^{-1}$), Argon ion, 488 nm ($20,491.80\text{ cm}^{-1}$) and diode, 785 nm (12738.85 cm^{-1}) laser lines.

3.2.4 Raman Signals

For the measurement of each sample, the power of the laser remained at 10-20 mW. It was found that the 1-10 sec acquisition time was adequate to record the spectral data with acceptable signal to noise ratios (SNRs), compared with the few minutes of acquisition time required by other Raman systems.

3.2.5 Data processing

First, high quality Raman spectra are collected before and after placing the solution of interest in the sample cell. The spectrum obtained with an empty Teflon tube represents the Teflon reference spectrum. The spectrum obtained from the sample filled tube contains both sample and Teflon spectral features. The Octave software is subsequently used to subtract the Teflon reference spectrum from the mixture spectrum. After Teflon subtraction, the sample spectral intensity is normalized by dividing the sample spectrum by an appropriate coefficient which represents the Teflon window intensity. Thus, the resulting sample spectrum contains no Teflon spectral features and is normalized to correct for any changes in either laser intensity or collection efficiency of the Raman spectrometer.

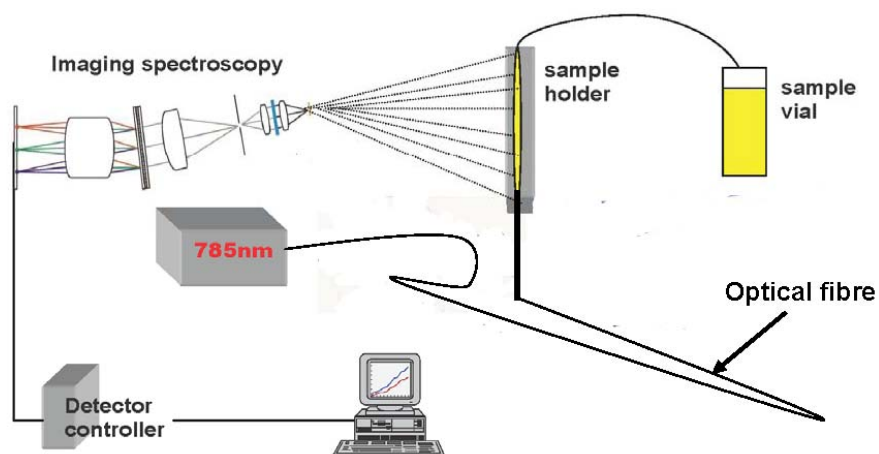


Figure 3-3. Schematic diagram of Raman spectrometer showing the fibre coupled to the VPH grating.

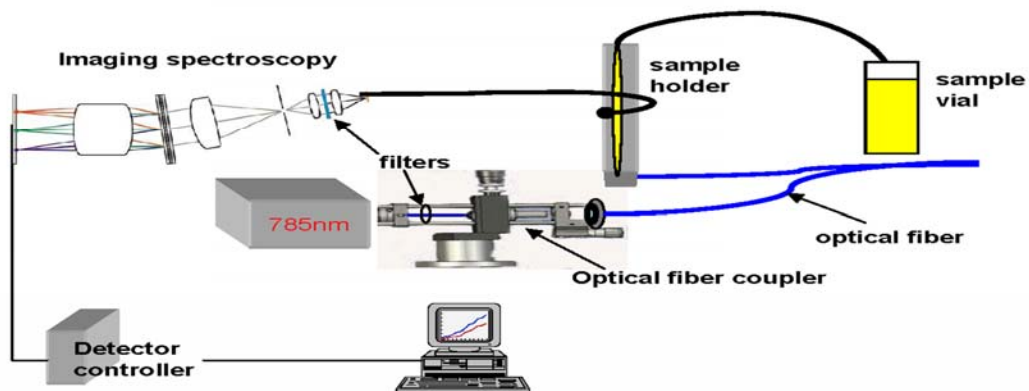


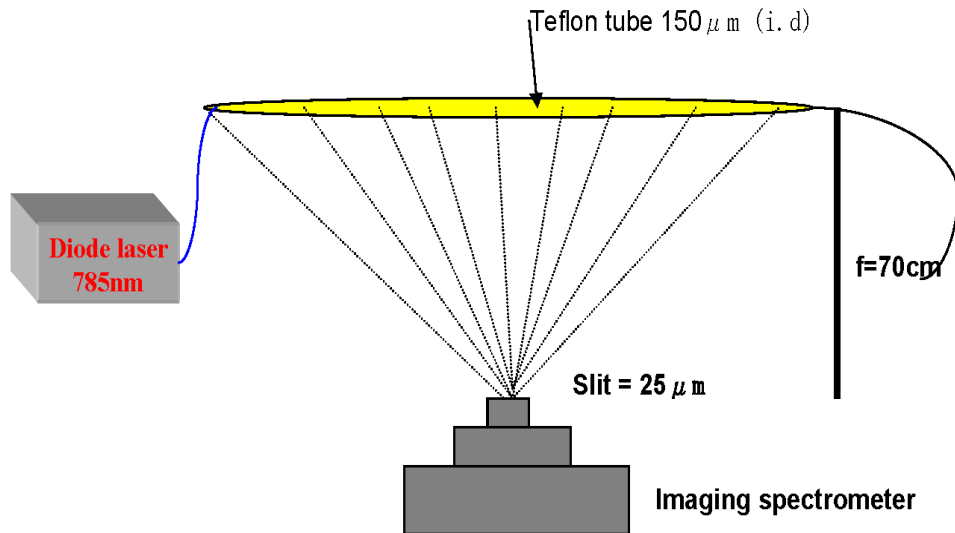
Figure 3-4. Schematic drawing for apparatus for the measurement of Raman spectra. For Raman signal collection, the optical fiber impinged on the Teflon tube.

3.2.6 Raman Liquid Waveguide Assembly

The schematic diagram of the cartridge that we have developed for characterization of protein-drug interaction is shown in Fig 3-5. An important aspect of this cell is the Teflon AF tube, which was based on the previous design in our laboratory. A Teflon® AF 2400 (150 μm i.d. x 360 μm o.d., ~ 5 cm) long was cemented on a glass slide. In order to effectively focus the excitation laser into the Teflon waveguide, the Teflon tube was sandwiched between two glass sheets which is 2 mm thick and 7 cm long. The distance between the edge of the two glasses to the tube remained the same. The issue of stability and alignment of the sample holder (cartridge) is very crucial, as the Teflon tube is imaged on the slit of the spectrometer which is 50 μm compared with the inner diameter of the Teflon tube which is 150 μm . A spectral resolution of 2 pixels was achieved by setting the entrance slits to 25 μm . The LCW end cell was placed approximately 70 cm from the spectrometer entrance slit. Light emitted from the LCW cell (Fig. 3-4) was imaged onto the entrance slit of the spectrometer with the use of an *Nikkor* camera lens ($f=105\text{mm}$) centered approximately 70 cm from the end cell, which produced in image magnification of 0.125 at the slit entrance. In order to obtain the maximum Raman intensity, the assembled cell was moved back and forth, in order to image the LCW on the slit effectively.

Therefore, to achieve the maximum detection of the Raman scattering of the sample, the sample holder and the spectrometer slit must be perfectly

aligned. A minor misalignment of the tube can make the data collection very time consuming and create spectral distortion. This cartridge is mounted on the XYZ stage with the option of moving it in three directions. Liquid samples were injected through the distal end of the tube using a syringe. Argon laser was injected into Teflon tube at the other end of the tube with a Ar⁺ ion laser operating at 20 mW or 785 nm diode laser operating at an average power of 20-30 mW at the sample. We use a syringe pump (Razel Pump Scientific) fitted with a Teflon tube to pump the sample into the liquid-core fiber , and we maintained the flow throughout the experiment. In this way, no void or bubbles were introduced into the tube.



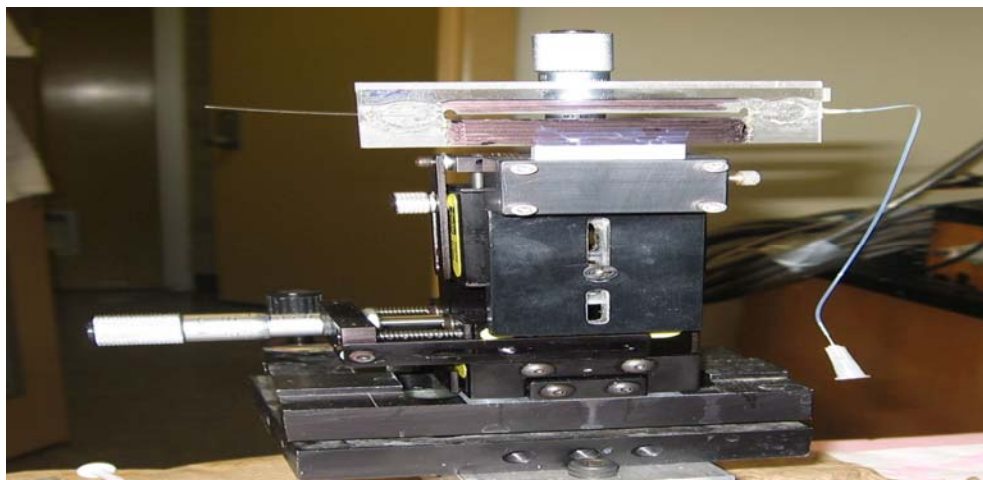


Figure 3-5. Schematic and image of the liquid-core waveguide system from a distance of 70 cm using 785 nm laser line. LCW, AF-2400 tubing (i.d., 150 μm ; o.d., 360 μm , length, 5 cm).

3.2.6.1 Cartridge assembly for fluorescence measurement

The anodic end was connected by glue with a piece of Teflon AF 2400 capillary and the cathodic end was connected by glue with a piece of fused-silica capillary, through two small pieces of microporous hollow fiber with a 30 nm pore size, 380 μm i.d., and 440 μm o.d. (Hoechst Celanese, Charlotte, NC, USA). Two polystyrene vials were glued on the ends of the separation capillary as electrolyte reservoirs, and the effective detection length of the capillary was 5 or 7.8 cm. The microporous hollow fibers functioned as physical barriers to prevent the macromolecule analyte from entering the electrolyte reservoirs but to allow small ions, such as protons and hydroxyl ions, to enter the separation capillary from the electrolyte reservoirs. A microtee (Upchurch Scientific, Oak Harbor, WA, USA) was used to couple the optical fiber into the cartridge from

the anode side and to introduce sample or solutions into the separation channel. The cartridge was mounted onto an *x-y* translational stage to facilitate adjustment of the cartridge to keep the separation capillary horizontal and parallel to the slit of the spectrometer. High voltage was provided with a RE-3002B regulated high-voltage supply (Northeast Scientific, Cambridge, MA, USA).

3.2.7 Materials and Chemicals

Teflon® AF 2400 tubing (150 µm i.d. x 360 µm o.d.) was purchased from DuPont. R-phycoerythrin (RPE) was purchased from Calbiochem–Novabiochem (La Jolla, CA, USA), at a concentration of 20 mg/mL. Oxaliplatin (99.9%), ethanol, 1-propanol, 1-butanol, 2-pentanol, 1-hexanol, cyclohexane (>99%), FITC-labeled human serum albumin (FITC-HSA) and human serum albumin (HSA, 70024-90-7, 98% purity, essential fatty acid free) were purchased from Sigma Chemical Company. All the chemicals were used without further purification, and the HSA molecular weight was assumed to be 66 500 g/mole to calculate the molar concentrations. All other reagents were of analytical grade, and doubly distilled water was used throughout all the experiments.

3.2.8 Solutions and Sample Preparations

The working solution of oxaliplatin (5.0×10^{-5} M) and HSA was obtained by appropriate dilution of the stock solution with phosphate buffer. Phosphate buffer solution containing 0.1 Mol NaCl was used to keep the pH of the solution

at 7.40. The prepared sample solutions were incubated in a water bath at 37°C prior to the experiment.

3.3 Results and Discussion

Raman spectroscopy has been shown to be a powerful tool in structural and conformational analysis of proteins²⁶. The application of this technique to study the interaction between oxaliplatin and HSA could help in the understanding of the mechanism of the interaction and action of the drug. The Raman spectrum of a protein such as HSA, arises from the peptide backbone and various amino acid side chain groups. Since the structure of HSA is stabilized by 17 disulphide bridges and one free Cys residue, the investigation of the change of the disulphide bond is very critical²⁷. Two groups of Raman markers of HSA are used to confirm the alteration of the HSA structure: (1) disulphide bridges and (2) Amide-I and Amide-III of the polypeptide chain of HSA. In the secondary structure of protein, bands related to amide-I attribute to C=O, while the oscillation of N-H contribute to Amide-III.

3.3.1 Raman measurement of HSA, oxaliplatin and HSA-oxaliplatin complex using 633nm excitation.

3.3.1.1 Disulphide bridges

Fig. 3-6 shows the Raman spectrum of HSA in the region of 300-800 cm⁻¹. The bands in the spectra range 400-700 cm⁻¹ are attributed to the stretching vibrations of C-S groups, and the vibrational modes in the range of 600-400 cm⁻¹ are attributed to the S-S groups²⁷. However, all these Raman bands

decreased after incubation with oxaliplatin, indicating distortion or breakage of the disulphide bridges (Fig 3-7). According to our previous work²⁸, using CIEF, UV/Vis and fluorescence, the structural distortion of HSA was demonstrated in a variety of incubation ratios.

In Fig 3-6, a weak Raman band observed at 507 cm⁻¹, attributed to ggg geometry, predominated in Cys-SS-Cys residues, while weaker bands at 540-536 cm⁻¹ and 518 cm⁻¹ indicated other conformations. As described above, we have identified two disulphide stretching bands at ~518 and ~507cm⁻¹ (Fig 3-6), and the Raman frequencies are similar to those reported previously²⁹.

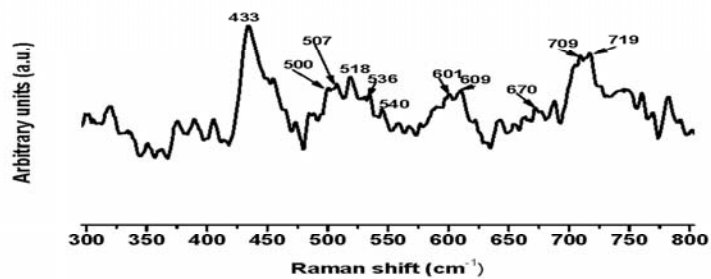


Figure 3-6. Raman spectrum (300-800 cm⁻¹) of HSA (5.0 x 10⁻⁵ M) in phosphate buffer at pH 7.40. The spectrum acquisition time was 20 sec.

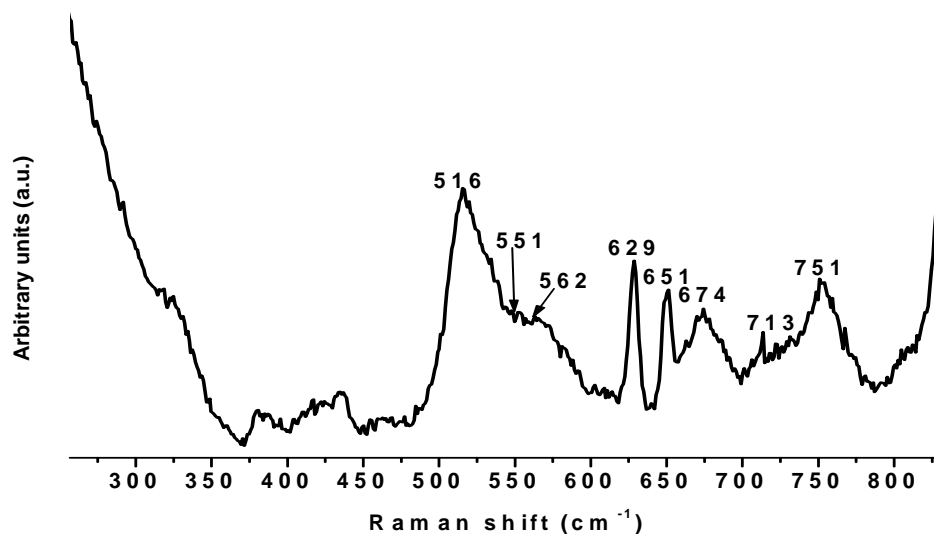


Figure 3-7. Analysis of the S-S Raman band of HSA ($5.0 \times 10^{-5}M$), with oxaliplatin in 1:10 molar ratio. The spectrum was collected under physiological conditions (in phosphate buffer at pH 7.40, 0.10M NaCl).

Monitoring the spectral range $300-800 \text{ cm}^{-1}$, results in a spectral evolution by which the protein S-S may be distorted or there is a breakage of the disulfide bridge. The interacted HSA shows a stronger and broader Raman band at 516 cm^{-1} , while new bands emerged near $600-700 \text{ cm}^{-1}$. HSA has several weak Raman features in the region $600-550 \text{ cm}^{-1}$ that could be attributed to aromatics. The unusual broad peak at 516 cm^{-1} may rather be a consequence of breakage of the S-S bonds. Indeed, the breakage of the disulfide bond can significantly affect the local couplings of the internal coordinates, thus modifying other vibrational modes. With respect to the peak identified here, the question remains as to whether it represents the complex formation between

HSA with oxaliplatin or whether it is the result of an arbitrary decomposition of the protein. In the same context, it is worth emphasizing that the appearance of new peaks in the range of 600-664 cm^{-1} is attributed to bands from the drug. However, a significant Raman shift was observed compared with the oxaliplatin spectrum prior to mixing with the protein (Fig 3-7). This result suggests that due to the presence of the drug, the HSA molecule may undergo a structural rearrangement and possibly structural decomposition under the drug load. Although the above conclusions are of intrinsic interest, they can probably be amplified by more extensive analyses of the spectra.

3.3.1.2 Amide-I and III

Concerning the binding of ligands to HSA molecule, there are conformation rearrangements, which can be rather considerable. Conformation rearrangements are possible in the whole molecule of HSA, not only in the binding region. For an estimation of the structural state of protein molecules oscillations of modes of Amide - I and Amide - III in the Raman spectra are used. These are oscillations of the main polypeptide chain.

The Raman spectrum of HSA is presented in Fig 3-8 which shows the strongest bands at 1655 cm^{-1} , 1276-1270 cm^{-1} (α -helix) and weak bands at 1264-1256 cm^{-1} (α -helix or random)³⁰. In addition, the line at 941 cm^{-1} is attributed to a CC stretching vibration, associated with helical conformation.

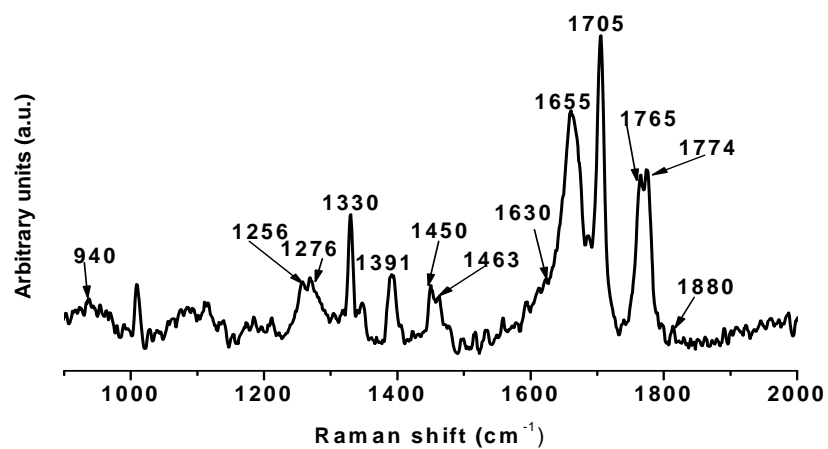


Figure 3-8 Raman spectrum of HSA (5.0×10^{-5} M) in the range of 1000-2000 cm^{-1} before incubation with oxaliplatin. The spectrum has been smoothed and baseline corrected using the Origin software package.

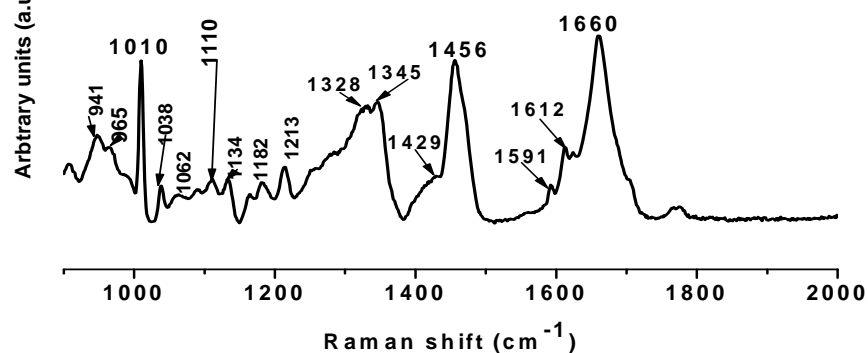


Figure 3-9. Raman spectrum of HSA after incubation with oxaliplatin.

HSA ($5.0 \times 10^{-5} \text{M}$) was incubated in 1:10 molar ratio with oxaliplatin ($5.0 \times 10^{-5} \text{M}$). The incubated solution was kept at 37°C for 1h before being inserted into the Teflon tube.

The analysis of the Raman spectrum of the native HSA in the amide I spectral region is shown in Figure 3-8. The amide I band of HSA, situated between 1610 and 1700 cm^{-1} , belongs primarily to the CO stretching mode and is dependent on the molecular environment of the protein. This mode is also sensitive to the protein secondary structure. This arises due to the dependence of the inter peptide vibration coupling and the arrangement of H-bonds on the secondary structure²⁹. The peak centered at 1655 cm^{-1} is sharp, and strong, and $1256\text{-}1276 \text{ cm}^{-1}$ is attributed to amide III. On addition of oxaliplatin at values of solution, intensity decreases for peaks in the ranges $1256 - 1276$

cm^{-1} and $1270 - 1280 \text{ cm}^{-1}$ are observed. This effect was also observed for peaks in the range $1645-1655 \text{ cm}^{-1}$. In addition, disappearance and appearance of peaks is observed for all the spectral ranges, while the area under the curve is increased for both amide I and III spectral regions. All these changes are related to the disassociation of the protein upon interaction with oxaliplatin. As already mentioned in the previous section, the breakage of the S-S bridge can significantly affect the local couplings of the internal coordinates. Many of these new peaks probably correspond to the protein, whereas others may be due to the structural modification undergone by oxaliplatin in the complex formation with HSA.

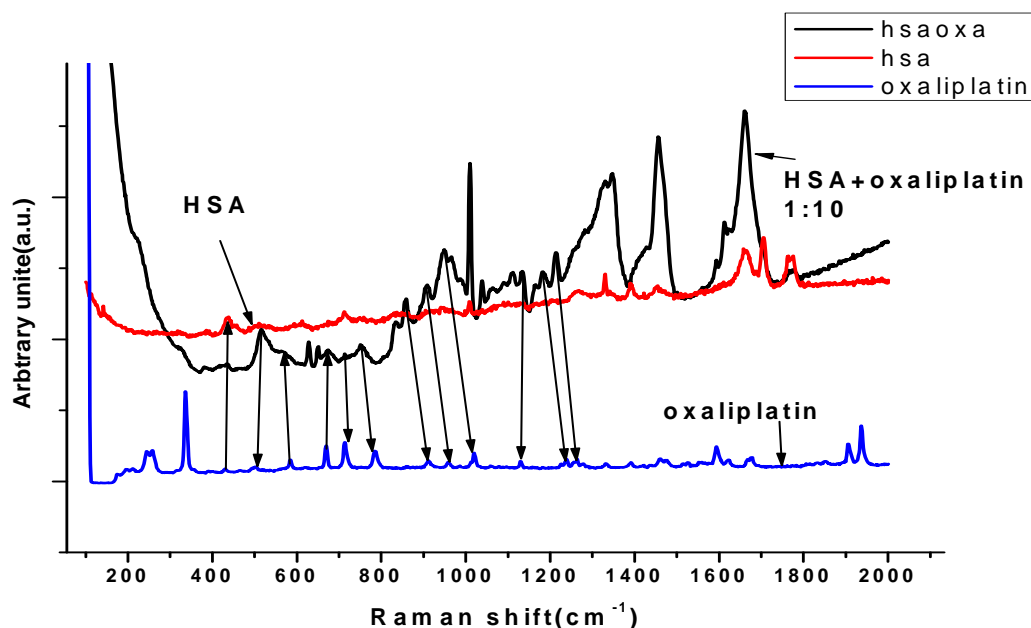


Figure 3-10. Raman spectra of HSA before and after incubation with oxaliplatin in molar ratio 1:10.

3.4 Liquid core waveguide (LCW) using high performance Raman spectroscopy under illuminated conditions from a distance of 70cm using 785nm laser line

3.4.1 Intensity of Raman Radiation

The intensity of Raman radiation produced by LCW tube in backscattering geometry has been predicted to vary with the length of the tube according to the following equation ²⁰

$$P_R = \frac{P_L K}{2\alpha} (1 - e^{-2\alpha x}) \quad (3)$$

Where P_R is the Raman power, P_L is the laser power, α is the (base-e) LCW loss coefficient, x is the LCW tube length, and K is a constant related to the scattering cross-section of the core liquid and collection angle inside the LCW tube. Equation 3 suggested that the loss coefficient is the same for both the laser and Raman scattered radiation.

3.4.2 Raman spectral features of Teflon® AF 2400 tube and water

Fluorescence background in Raman measurements is more common and more significant than with conventional small path length tubes. The numerical aperture (NA) of an optical fiber depends on the difference of the squares of the refractive indices of the clad and core regions (Fig 3-11). In this vein, the light

throughput in a liquid-filled AF tube is highly dependent on the refractive index of the liquid in the tube.

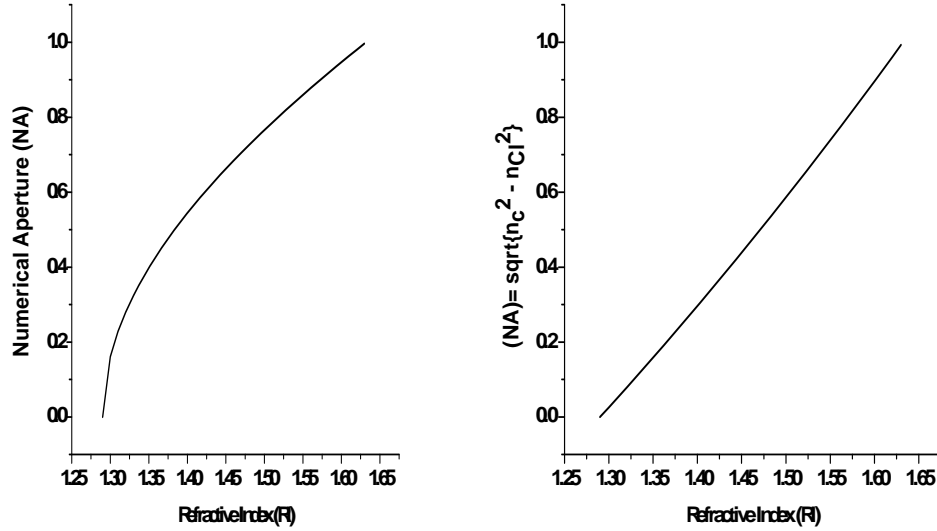


Figure 3-11. Relation between NA and RI of optical fibre.

The RI of the AF tube functioning as the “cladding” region of the optical fiber, of course, remains constant. The RI of the solution in the tube is always higher than the RI of the AF tube. Accordingly, the numerical aperture and the light throughput increase dramatically with increasing RI of the inner solution.

$$P \sim NA^2 \sim n_c^2 - n_{cl}^2 \quad (4)$$

Where P is the laser power, NA is the numerical aperture of the optical fibre, n_c and n_{cl} are the refractive index of the core and the clad of the optical fibre.

The Raman spectrum of Teflon® AF tube excited using 785 nm laser line is shown in Fig.3-10. The molecular structure of the Teflon AF 2400 and its Raman spectrum are shown in Fig 3-12. A major problem in LCW-RS is the background fluorescence from the Teflon tube and water, which easily masks the weak Raman signals. This broad band fluorescence covers most of the visible region of the spectrum and reaches a maximum near the center of the visible region. Fluorescence is often orders of magnitude stronger than the inherently weak Raman scattering effect, and broad and strong fluorescence bands due to the presence of one or several fluorophores often lead to detector saturation before adequate Raman signal intensity is obtained. Teflon-AF fluoresces strongly when excited with a visible laser lines such as 488 or 514 nm. As shown in the enlarged plots in Fig 3-11, Teflon-AF has Raman bands at 725, 788 and 843 cm^{-1} . These spectra clearly demonstrate that, peak overlapping is possible. However, there are two approaches we adapted to minimize this background: switching the excitation wavelength either to the (near)-IR region and using extensive Teflon-water subtraction criteria to minimize the interferences.

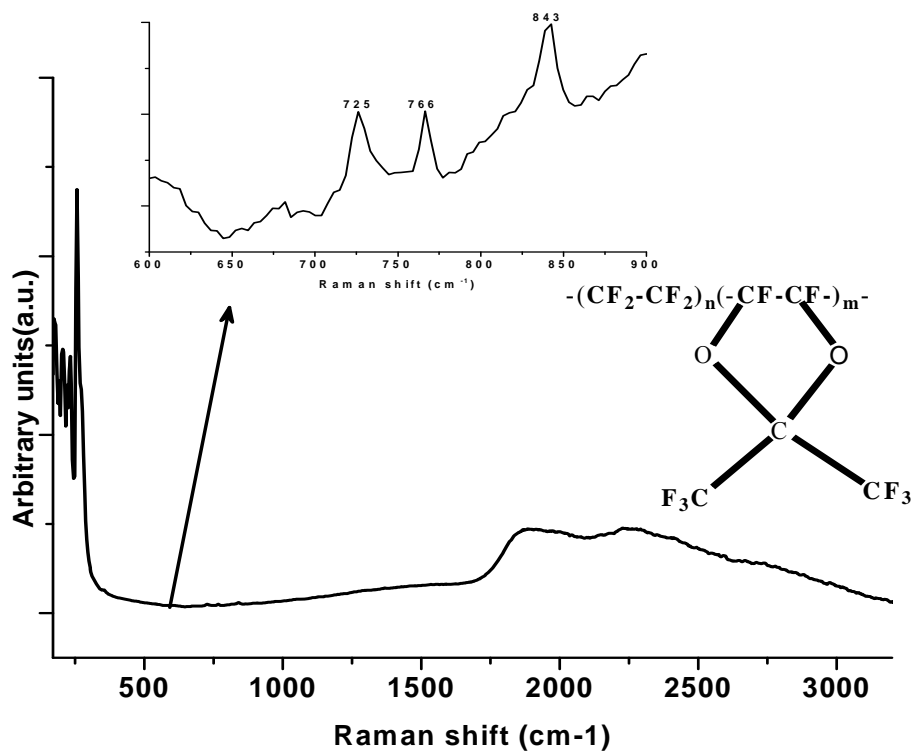


Figure 3-12. Raman spectrum of empty Teflon® tube AF 2400 acquired with 785 nm excitation line. The inset shows Teflon AF polymer structure.

The water Raman spectrum is relatively weak and flat at the fingerprint region of the spectrum which is 300 to 1500 cm^{-1} . We compared the Raman spectra of Teflon-AF collected with water and buffers. Water shows somewhat greater fluorescence intensity when compared with Teflon-AF when collected from the Teflon-AF tube. This indicates that our background intensity is primarily due to water itself, rather than to the Teflon-AF tube. There is a similar conclusion from the published Raman spectrum of water. In addition, the three Teflon-AF bands show minor or no interferences due to the weak signal compared to the sample peak.

Table 3-1. Refractive indices of various solvents and cell materials.

Solvents and cell materials	Refractive index (n_d)^a
Teflon® AF 2400	1.29
Teflon® AF 1600	1.31
Methanol	1.326
Water	1.333
FEP ^b	1.342
Acetonitrile	1.342
Ethyl ether	1.352
Acetone	1.357
Ethanol	1.359
PTFE ^d	1.35~1.38 ^c
Ethyl acetate	1.370
n-Hexane	1.372
2-Propanol	1.375
Methylethyl ketone	1.377
1-Propanol	1.383
4-Methyl-2-pentanone	1.394
1-Butanol	1.394
Cyclohexane	1.424
Chloroform	1.444
Quartz glass	1.458 (18°C)
Carbon tetrachloride	1.459
Borosilicate glass (Pyrex®)	1.474 ^c
<i>p</i> -Xylene	1.493
Toluene	1.494
<i>m</i> -Xylene	1.495
Benzene	1.498
Chlorobenzene	1.523
Acetophenone	1.587
Bromoform	1.587

^a **Note:** 25°C Unless otherwise stated. The values are cited from reference ³⁰.

^bFEP:

^cNo data on temperature

^d PTFE: poly(tetrafluoroethylene)

3.4.3 Remote spectral measurements with fiber-optic coupled with LCW-RS from a distance of 70cm

To demonstrate the signal enhancement made possible using the LCW-RS, Raman spectrum of cyclohexane aqueous solutions are shown in Figure 3-13. The Raman spectrum of liquid cyclohexane was collected in the 350-3200 cm^{-1} region. Most organic solvents are strong Raman scatterers and have several Raman bands; such features make them ideal for calibration purposes, and they are inexpensive. Note that the cyclohexane bands are relatively well separated from the Teflon AF tube bands, and should not interfere with the three bands. For this experiment, the laser power at the sample was maintained in the range of 10-20 mW. This range of power was kept throughout the experiment, since powers exceeding >20 mW can melt the Teflon tube. Smaller diameter LCW tubing usually generates high power density per unit cross section when exposed to high laser power. This power limitation often restricts to using higher laser power for the application of this technique to investigate protein samples such as hemoglobin or HSA. An attempt was made to measure Raman signals from a variety of protein samples. It was found that due to the structural complexity of the proteins, a high energy laser power is required to probe the Raman active species of the proteins. Additionally, low solubility and denaturing at high power limits the technique for biological applications.

The higher intensity Raman spectrum of cyclohexane, shown in Figure 3-13, was collected in a 5 cm, 150 i.d. Teflon AF waveguide at a distance of 70 cm from the collection lens using a hyper sensitive spectrometer by P&P Optica³¹. In this mode, 1 μ L sample was injected into a 5cm Teflon® AF tube using a disposable syringe (1mm). Measurements usually consisted of five replicate cyclohexane spectra. A sample of typical results is presented in Table 3-2. The positions of these Raman peaks shown in Fig.3-13 are within ± 2 cm^{-1} of the values reported in the literature³⁰. However, the lower intensity of cyclohexane spectrum, shown in Figure 3-13b, was due to the detector sensitivity weakening as we approach the CH asymmetric and symmetric bands (Fig.2-5). The strong Raman peak at 802 cm^{-1} (CH_2 deformation + ring mode) was used to evaluate the performance of the LCW-RS vs cyclohexane spectrum published by Sigma-Aldrich®³².

Fig 3-13 shows typical spectra of cyclohexane recorded with the LCW-RS fiber-optic coupled system collecting at a distance of 70 cm, where the strong fingerprint Raman lines of cyclohexane (385 and 1600 cm^{-1}) are well resolved. The Raman signal intensity from the spectrum of cyclohexane in the LCW-RS was greatly enhanced over the spectrum collected by Sigma-Aldrich. It should be noted that the cyclohexane spectrum was acquired with 1s exposure time. The intensities of the Raman peaks at 802 cm^{-1} were calculated after a background correction was performed to remove Raman scattering due to the water and the Teflon® AF tube. Even without the background subtraction procedure, the cyclohexane spectrum shows a good signal to noise ratio (S/N).

This may be due to the fact that the LCW provided an excellent enhancement effect due to the low refractive index of the Teflon AF tube compared with other solvents and materials (Table 1) . Once again, the distance Raman system has been shown here to detect all of the major Raman bands present in the sample in a very short period, including the Raman bands at 1500-2300 cm^{-1} which is absent in the spectrum published by Sigma-Aldrich³².

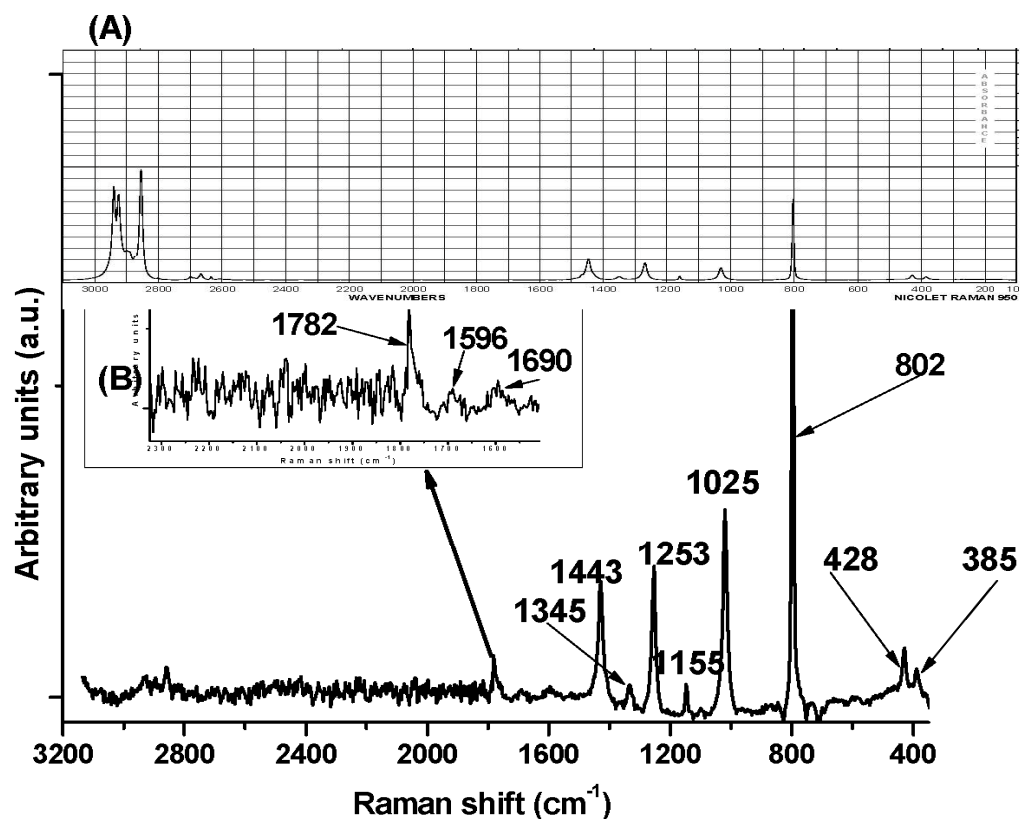


Figure 3-13. Comparison of source and target spectrometers, based on a view of comparable spectra. (A) Cyclohexane fingerprint spectrum from Sigma-Aldrich³². (B) Cyclohexane spectrum in 5 cm long, 150 μm i.d., 360 μm o.d.

acquired with $\lambda=785$ nm , the laser power at the sample was 15 mW and the acquisition time was 1 s.

A comparison of the two spectra in Figures 3-13(A-B) show that all features of the LCW-RS spectrum are both present and enhanced in the waveguide spectrum. The spectra compare quite favourably to those using conventional delivery and collection optics. Note, there are also no extraneous peaks in the waveguide spectrum from the Teflon AF tubing. When the laser is properly launched into the core of the waveguide, there is minimal Raman scattering collected from the Teflon AF waveguide cladding.

Table 3-2. Observed Raman frequencies of cyclohexane

Band (cm ⁻¹)	Symmetry Species	Assignment
385	a _{1g}	Ring mode
428	e _g	CCC deformation + CC torsion
802	a _{1g}	CH ₂ deformation + ring mode
1025	e _g	CH ₂ deformation + ring mode
1155	a _{1g}	CH ₂ deformation
1253	e _g	CH ₂ deformation
1345	e _g	
1443	e _g	CH ₂ scissors
1596	e _g	CH ₂ scissors
2855	a _{1g}	CH ₂ symmetric stretch
2895	e _g	CH ₂ stretch
2930	a _{1g}	CH ₂ symmetric stretch
2941	a _{1g}	CH ₂ symmetric stretch

To further demonstrate the effectiveness of the LCW-RS, a more complicated mixture of similar alcohols was investigated. Figure 3-14 shows the

Raman spectra obtained for a mixture of five to six alcohols injected into the Teflon AF tube, where the strong fingerprint regions of Raman lines of these alcohols ($400\text{-}1600\text{ cm}^{-1}$) are well resolved. Individual sample peaks are narrow relative to their target counterparts. However, such similar structural profiles pose great challenges to distinguish individual spectral features from the plot (Figure 3-13). The distinctive molecular fingerprint of each alcohol is evident from Figure 3-13. It is possible however to distinguish these alcohols with the same functional group, e.g., ethanol ($\text{C}_2\text{H}_6\text{O}$) and 1-butanol ($\text{C}_4\text{H}_{10}\text{O}$) from each other by using the positions of the fingerprint region. Figure 3-13 compares all the spectra of the six alcohols, which have hydroxide as the common functional group but different structures.

The Raman spectra of methanol, 1-butanol, ethanol, isopropanol, 5-pentanol and 1-hexanol are shown in Figure 3-14. The vibrational assignments are as follows: The region between ~ 1000 and $\sim 1260\text{ cm}^{-1}$ contains the bands associated with the C-C and C-O stretches.³³ The C-O-H bending band occurs between ~ 1200 and $\sim 1450\text{ cm}^{-1}$.³³ The CH_3 bend occurs at $\sim 1460\text{ cm}^{-1}$, and the bands associated with the C-H stretches appear between $\sim 2840\text{ cm}^{-1}$ and $\sim 3000\text{ cm}^{-1}$ (not shown).³³ Notice in Figure 3-14 and b the overlap of some of the bands when the data is plotted on the same axis. However, their distinct spectral features allow for positive identification using our high performance spectrometer coupling LCW (Figure 3-14(a-d)).

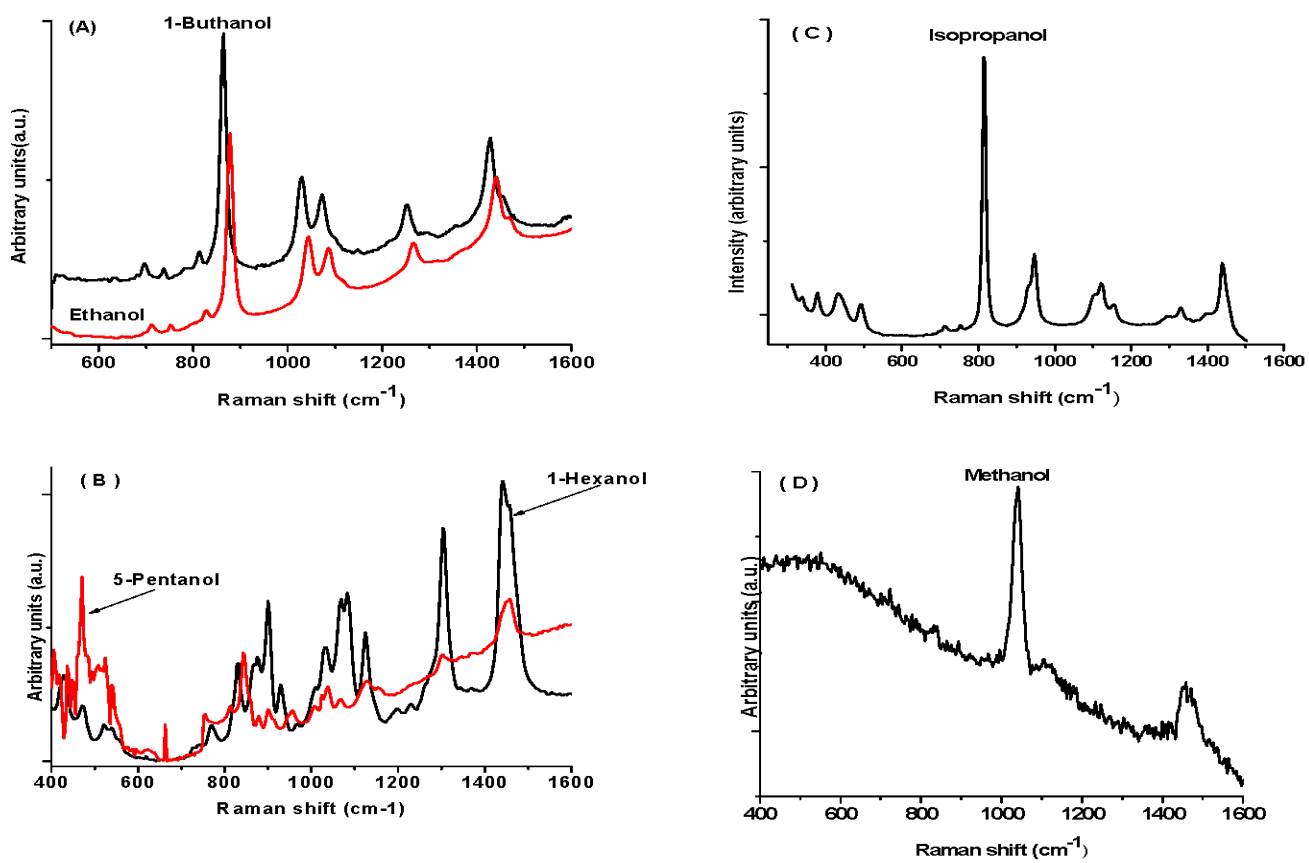


Figure 3-14. Standard Raman spectra of six alcohols.

3.5 Application of CIEF-LCW by the combined

Raman/fluorescence spectrometer to measure fluorescence spectra of proteins using 488nm excitation line

Raman spectrometers have a high spectral resolution of about 5 cm^{-1} over the wavenumber range of $788\text{--}1049\text{ nm}$ ($48\text{--}3206\text{ cm}^{-1}$), while fluorescence spectrometers have high spectral resolutions of 0.4 and 0.1 nm over the wavelength range of $486\text{--}757\text{ nm}$ ($84\text{--}7264.3\text{ cm}^{-1}$), respectively. In particular, the signal-to-noise ratio of Raman spectroscopy has been improved by using a volume phase holographic (VPH) diffraction grating and a liquid-nitrogen-cooled charge-coupled device detector. The performance of the combined spectroscopy system has been demonstrated by taking fluorescence measurement on highly fluorescent two diverse protein molecules, R-phycoerythrin (RPE) and fluorescein isothiocyanate (FITC)-labeled human serum albumin (HSA).

The details of the optical configurations of the apparatus and the separation cartridge will be described in detail in Chapter 4 (section 4.2.1). However, for the fluorescence measurements, the separation capillary was replaced by the Teflon AF tube. To discuss the results obtained from the fluorescence measurements it is necessary to consider two major factors that influence these values, i.e., the performance of the high sensitive spectrometer and LCW enhancement factor in the presence of high refractive index species (Table 3-2). As has been pointed out in previous sections, the high performance of our system was demonstrated using selected samples as an example. This is

especially important for the implementation of this technique to wide areas of applications.

The results of the capillary isoelectric focusing in the LCW tube with two different fluorescence proteins with ampholyte (pH 3-10) are shown in Figs. 3-15 and 3-16. These low molecular weight ampholytes help to facilitate the formation of stable gradients across the tube. The concentration of the two samples was kept very low to avoid sample absorption on the wall of the tube and attenuation of the laser intensity along the tube. Higher sample concentration also affects the TIR by absorbing the propagating light³⁴.

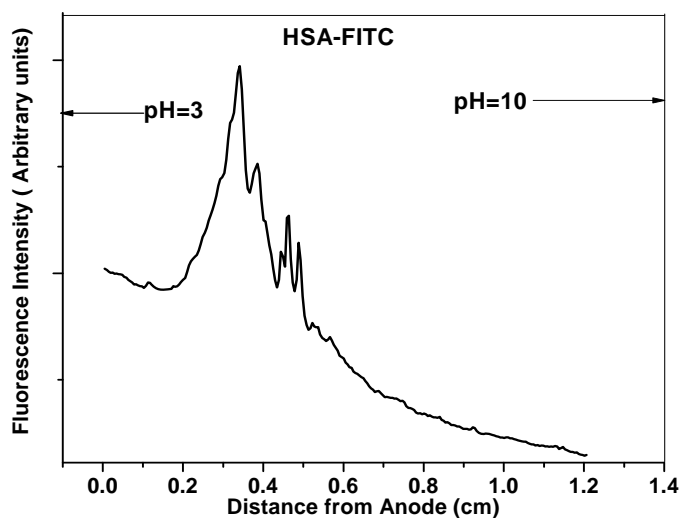


Figure 3-15. CIEF of FITC-labeled HSA 10 $\mu\text{g}/\text{mL}$. The sample containing 2% pharmalytes (pH 3–10) and 0.5% PVP. Separation capillary: 5 cm, 150 i.d. Teflon® AF 2400 capillary. Applied voltage: 0–5 min, 1 kV; 5–15 min, 3 kV. Excitation: Argon ion 488 nm at 5-10 mW.

As the result shows in Fig 3-15, the concentration of the protein was kept low to avoid the problems stated above. HSA-FITC is FITC labeled protein with a maximum excitation wavelengths 488 and 520 nm., respectively. FITC labeling is frequently used to improve sensitivity of protein analysis by capillary electrophoresis . After 10 min of focusing time, the fluorescence spectrum of HSA-FITC revealed a multiple peaks at its isoelectric point. Both proteins (HAS-FITC and RPE) were separated in an isoelectric focusing medium. The locations of the peaks match reasonably well to those published results, but the observed multiple peaks are not consistent with those that reported.³⁴ The main reason to such performance enhancement was the use of advanced optics and the unique system approach that dramatically improves the system efficiency.

The fluorescence spectrum shows several distinctive features. This provides evidence that more than one amine sight can be bonded with FITC during the derivatization procedure on the protein. The appearance of the multiple peaks also suggested the possible Raman scattering bands associated with the observed peaks. It has been reported that the Argon laser 488 nm line generates Raman scattering centered at 495 and 575 nm and these modes interfere with the fluorescence signal ³⁵. This interference can also generate a significant background signal associated with water or other solvent. The broad peak observed for HSA-FITC also likely due to the multiple labeling. The laser power was maintained throughout the experiment at 1-10 mW to avoid any sample damage due to photobleaching.

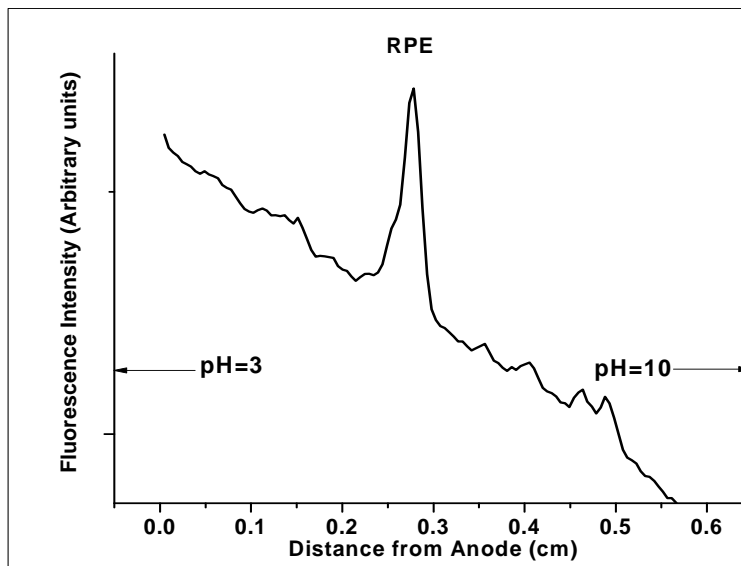


Figure 3-16. CIEF of RPE sample $5\mu\text{g/mL}$ RPE; containing 2% pharmalytes (pH 3–10) and 0.5% pvp. Separation capillary: 5-cm x150 μm i.d. Teflon AF 2400 capillary. Other conditions as in Fig. 3-15.

R-phycoerythrin (RPE) was selected as the second model protein to investigate the CIEF-LCW fluorescence capability of the instrument. An excellent separated with a good peak shape was obtained after 10 min focusing time (Fig3-16). Although, the fluorescence spectrum shows a good peak shape, similar to the previous result, a strong background was observed. As already discussed above, Raman scattering or Raleigh tail can be responsible for the observed background. This required more investigation to understand the nature of interference that contributes to such strong background.

3.6 Limitations of LCW-RS

While the LCW coupling with the Raman spectrometer system described here provides very accurate and sensitive Raman measurements of dilute aqueous samples, the field of waveguide-enhanced aqueous Raman spectroscopy is still in its infancy, especially for biological applications. One limiting factor is that techniques for manufacturing high-quality optical waveguides from Teflon-AF are not yet optimized. Sample absorption and degradation of the Teflon tube at higher laser powers also restrict the universal applicability of the LCW for biological applications.

3.7 Conclusions

The evaluation of a high performance LCW-RS can be characterized in a number of ways. During the course of our work developing and characterizing the new system, the simplicity of this method, the reasonable Raman signal enhancement, combined with the high degree of reproducibility with the analyte and small sample volumes required, make it a promising candidate for sensitive low-power identification of several species including biological samples.

The LCW-RS using a high performance spectrometer is a promising technique for studying protein characterization and investigation of drug-protein interactions. In this study the structural changes of HSA under action of the antitumor drug was investigated by the Raman spectroscopic method. Our high performance Raman spectrometer has been adapted for measuring spectra in visible and NIR spectral ranges. This spectrometer was demonstrated to have superior stability, simplicity and accuracy, large throughput, cost efficiency and sensitivity compared to those of a multichannel dispersive Raman spectrometer.

Using this technique, we have investigated the interaction of oxaliplatin with HSA through two different sites (S-S disulfide bridge and amide I and III). In the case of S-S, the spectral region of S-S disulfide bonds indicates the breakage of the bond that results in the rearrangement of the protein structure. Furthermore, the amide I and III regions indicate that, the drug induced a significant structural change when incubated with HSA for a short period of time.

Consequently, it has been demonstrated that the present system enables one to measure Raman and fluorescence signals with sufficient reproducibility from run to run. With use of this system, we measured the Raman signal and fluorescence at a distance of 70 cm. A comparison of the relative efficiency of the system compared to conventional techniques has been presented here. It should be noted that the present successive measurement has the advantage of observing Raman signals and fluorescence easily. In the traditional way for measuring Raman signals, expensive and complicated optical configuration is required. With the present system, on the other hand, relatively strong Raman signals are obtained with a simple optical configuration. We have also shown that simultaneous measurements of Raman signals and fluorescence signals (or absorption if necessary) can be achieved by removing only the laser filter. In particular, the combination of the LCW and the inexpensive high performance spectrometer can provide highly sensitive and convenient routine analytical systems.

Finally, this work describes the first step towards the potential application of the high performance spectrometer system for coupling with CIEF and at the same time perform Raman spectroscopy studies. The two dimensional array opens completely a new way to investigate or characterize proteins using CIEF. Furthermore, this spectrometer should replace the conventional detection techniques which employ a CCD camera.

CHAPTER 4

INVESTIGATION OF INTERACTION BETWEEN HUMAN HEMOGLOBIN A₀ AND PLATINUM ANTICANCER DRUGS BY CAPILLARY ISOELECTRIC FOCUSING WITH WHOLE COLUMN IMAGING DETECTION*

4. 1 Introduction

Platinum-based drugs are among the most active anticancer agents and have been widely used in the treatment of a variety of human tumors. Over the last 30 years, a large number of platinum analogues have been synthesized to enlarge the spectrum of activity, overcome cellular resistance, and/or reduce the toxicity of both first (i.e. cisplatin) and second generation (i.e. carboplatin) platinum drugs¹.

***The result presented in this chapter have been published:**

Tibebe Lemma, Rupasri Mandal , Xing-Fang Li, and Janusz Pawliszyn

Investigation of Interaction between Human Hemoglobin A₀ and Platinum Anticancer Drugs by Capillary Isoelectric Focusing with Whole Column Imaging Detection. *Journal Separation Science* ,21, 1803-1809, 2008

Unless otherwise stated, all of the work reported in this chapter was performed and analysed by the candidate

Of these platinum-based compounds, oxaliplatin, a novel compound containing a trans-1-(R,R)-1,2-diaminocyclohexane (DACH) (Fig.4-1) carrier ligand, has recently been approved for the treatment of metastatic colorectal carcinoma in conjunction with fluoropyrimidines². Oxaliplatin has shown *in vitro* and *in vivo* efficacy against many tumor cell lines and tumors, including those that are resistant to cisplatin and carboplatin^{1,3-5}.

In addition to its positive effects oxaliplatin also shows several toxic effects. The main cumulative dose-limiting toxicity of oxaliplatin is progressive peripheral sensory neuropathy^{6,7}. It is also associated with an acute neuropathy mild which reverses in several hours or days^{6,7}. Oxaliplatin can also produce diarrhea, vomiting and hematological suppression^{7,8}. However, the mechanisms of action and toxicity are not clear.

Pt-containing anticancer drugs are believed to induce apoptosis in cancer cells by covalently binding to DNA⁹⁻¹¹, however, they also react with a number of proteins and peptides, such as glutathione, which may also play a role in detoxification of oxaliplatin¹². In addition, after these drugs are introduced intravenously, 65 – 98% of the drugs are bound to blood plasma proteins¹³⁻¹⁵, and 40% of the blood platinum is found in erythrocytes^{15,16}. While it is widely accepted that Pt-DNA adducts are responsible for the drug's cytotoxicity, the role of Pt-protein adducts in the mechanism of action and toxicity of the drug remains unclear. Platinum-protein adducts are suggested to be the cause of the drug's side effects; however, there are also claims that they are important to the drug's activity¹⁷. Therefore, information on how

anticancer drugs interact with proteins is important for the understanding of the mechanisms of action and toxicity of a drug and the optimization of cancer treatments.

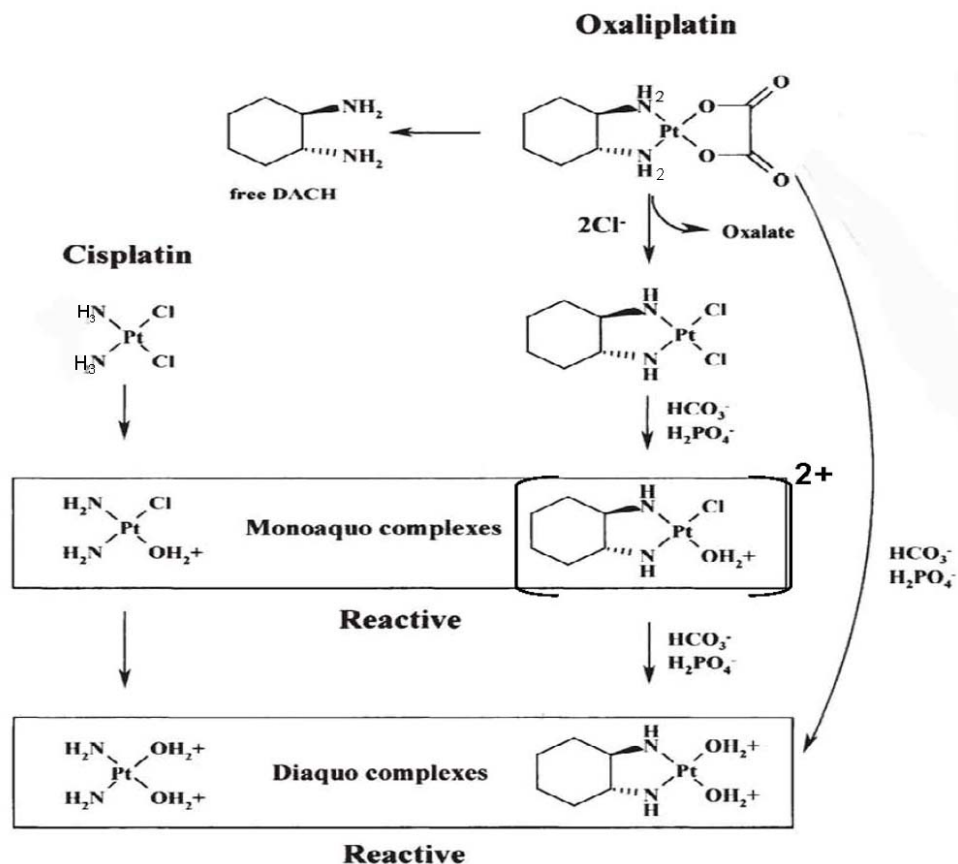


Figure 4-1. Major oxaliplatin and cisplatin metabolites.

The dominant adult hemoglobin (Hb A₀) exists as a noncovalent tetramer consists of two α (141 amino acids; 15 126.4 Da) and two β (146 amino acids; 15 867.2 Da) polypeptide chains and a heme group is bound to each of the chains through noncovalent interaction¹⁶. Recently, the formation of Hb-Pt complexes and the release of heme group from Hb was determined using size

fractionating, size exclusion, high performance liquid chromatography-inductively coupled plasma mass spectrometry (HPLC-ICPMS), and nanospray mass spectrometry (MS) ¹⁸. The information obtained from this study suggested the heme dissociation induced by Pt drugs may be important to improved understanding of side effects (e.g. anemia) of the cancer patients undergoing such treatment because the heme group binds molecule of oxygen and carrying oxygen from lungs to different tissues. Therefore, investigation of the structural alteration of Hb induced by Pt, and studying the nature of the complex formed will add significantly to the success of understanding the mechanism of action and toxicity of the drugs.

Advanced analytical techniques and methodologies are essential for obtaining this information. Nowadays, there is strong concern in the anticancer research community regarding improvement of the analytical techniques in use. This led in particular to a growing number of metallodrug-protein investigations performed using valuable techniques superior to contemporary methods in the field. A recent review summarizes the progress made in the applications of modern analytical methodologies for antitumor metallodrug-protein studies ¹⁹. Electrospray ionization mass spectrometry (ESI-MS) was recently shown as an extremely useful tool for studying the cisplatin-protein interactions ^{18, 20-24}. As well, high performance liquid chromatography (HPLC) ^{18, 23, 25-27} and a complementary high-resolution technique with an orthogonal separation mechanism, capillary electrophoresis (CE) ²⁸⁻³⁰, are growing in importance for characterizing the protein binding for different metal complexes. The potential

of resolving intact and protein-bound drug forms appears to be prominent when combined with a metal-specific mode of detection by using inductively-coupled plasma mass spectrometry (ICP-MS)^{18, 24, 26-28}.

Capillary isoelectric focusing (CIEF) provides high resolution separation of amphoteric biomolecular species based on differences of their isoelectric point in a pH gradient formed by carrier ampholytes, when an electric potential is applied³¹. This high-throughput technique offers greater resolving power and becomes a standard method for analysis of protein and protein-ligand interaction. The utilization of the whole column detection approach with UV WCID gives this separation technique a unique advantage over the conventional single point detection³¹⁻³⁴. For example, in single point detection, several problems are encountered during the sample mobilization process, including protein precipitation, long analysis time and distortion of pH gradient. In contrast, CIEF-WCID successfully eliminates the mobilization process by using the WCID technique.

Owing to the merit of on-column detection and the capability of attaining real-time monitoring of the changes in peak area, CIEF-WCID is suitable for protein-protein and protein-drug interactions. Recently CIEF-WCID has been successfully applied in our group to investigate protein-DNA³⁵, protein-amino acids³⁶ and protein-lipids³⁷⁻⁴⁰ interactions. Furthermore, we demonstrated the use of this technique to determine the molecular weight of unknown proteins⁴¹. CIEF-WCID is expected to make a unique contribution in proteomic research because of its ability to resolve wide ranges of proteins and protein complexes

that have small differences in pI in real-time. This technique is very important when one studies protein- ligand interactions such as protein-protein, protein-DNA and protein-drug.

The development of efficient and sensitive analytical methods for the separation, identification and quantification of drug-protein adducts is paramount for understanding the drug activity and toxicity. The objective of the preset study is to develop a CIEF-WCID to investigate the interactions of Pt-containing anticancer drugs, cisplatin and oxaliplatin with a model blood protein, human hemoglobin (Hb). The structural changes of the Hb is investigated by monitoring the pI during the incubation of oxaliplatin and cisplatin with Hb. CIEF is the highest efficiency single dimensional separation method available for the investigation of the interaction between proteins and ligands. This technique offers a number of advantages, including speed, high separation efficiency, short analysis time and reduced sample consumption. Although the CIEF technique shows a number of advantages, quantitative information was chiefly provided by other techniques.

To our knowledge, the investigation of cisplatin or oxaliplatin interaction with Hb by CIEF with WCID is the first report of this type of analysis. The development of a simple and reliable method to study drug-protein interactions is of great practical and theoretical importance.

4. 2 Experimental

4.2.1 Apparatus

The CIEF experiments were carried out on a commercial iCE₂₈₀ instrument (Convergent Bioscience, Mississauga, Canada). The system was equipped with a CCD camera for image collection. Separations were performed on commercial cartridges with silica capillary tubes (Convergent Bioscience), with an effective length of 5 cm, 100 μm I.D. and 200 μm O.D. The capillary wall was coated with fluorocarbon (Restek, Bellefonte, PA, USA) to suppress the electro-osmotic flow (EOF). Focusing was carried out for 2 min at 500V, and the system was set at 3000V for the remainder of the analysis. The catholyte and anolyte contained 1% PVP with 100 mM NaOH and 100 mM of H₃PO₄, respectively. The sample, which was mixed with 0.5% pvp and 2% ampholyte (pH 3 -10), was manually injected with a needle. To avoid inconsistent coating efficiency, all capillaries were dynamically coated with additives for thirty minutes prior to the experiment. During the focusing process, the current was decreased from 10.8 μA to 4.7 μA , prior to completion.

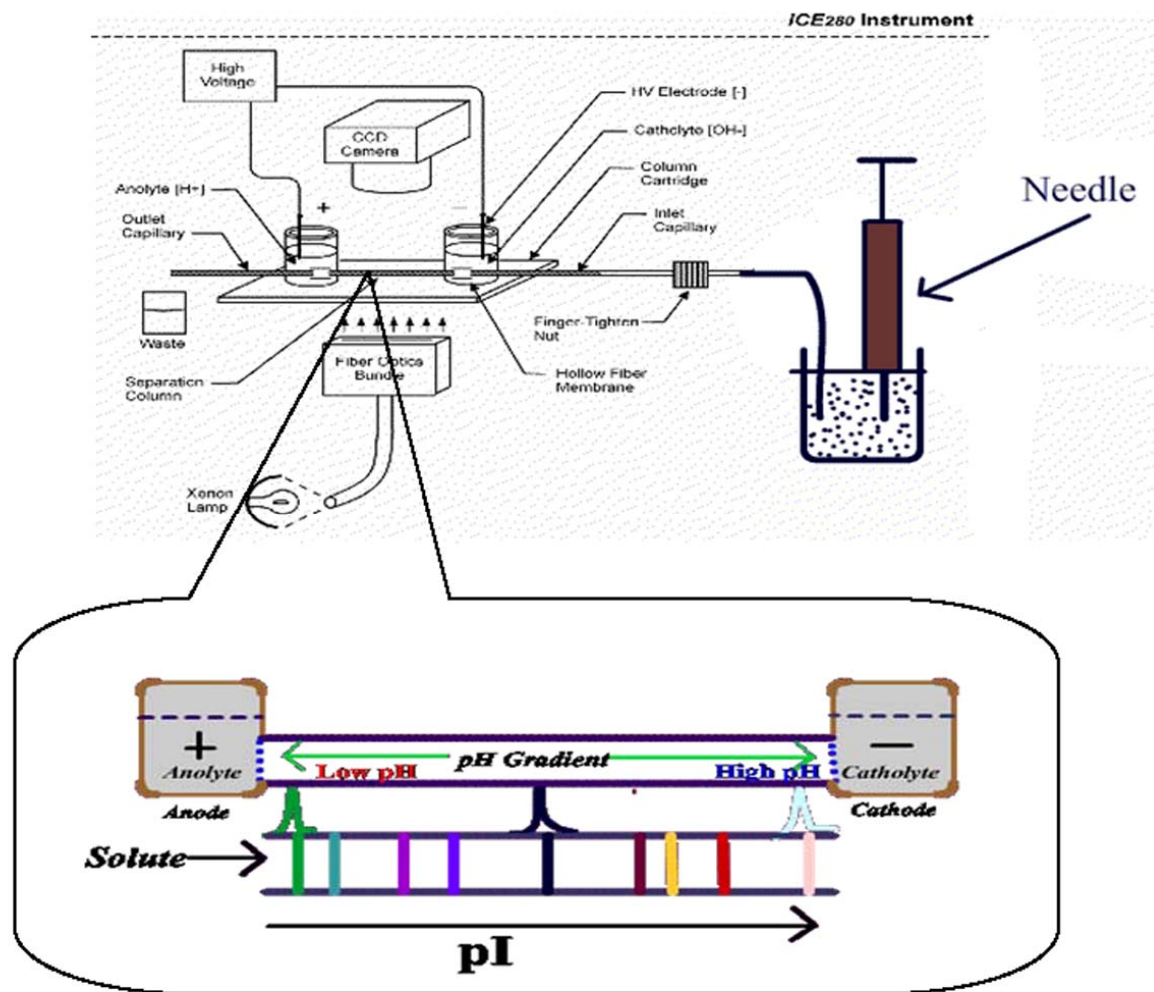


Figure 4-2. The schematic diagram of the whole column imaging detection for CIEF.

4.2.2 Chemicals

[SP-4-2-{1R-trans)]-(1,2-Cyclohexanediamine-N,N')
[ethanedioata(2-)-O,O']platinum (oxaliplatin) (99.9%), *cis*-Platinum(II)
diammine dichloride (cisplatin) (99.9%), carrier ampholytes (Pharmalytes 3.0-
10.0), and human hemoglobin A₀ were purchased from Sigma (St. Louis, MO,
USA). Polyvinylpyrrolidone (PVP) was purchased from Aldrich (Milwaukee,
WI, USA). Water was purified with a NANOpure water system
(Barnstead/Thermolyne, Dubuque, IA, USA) and had a minimum resistivity of
18.0MΩ-cm.

4.2.3 Solutions and Sample Preparation

Stock solutions of oxaliplatin and cisplatin were prepared with a
concentration of 5 mmol/L. The Hb stock solution was prepared with a
concentration of 25μmol/L. The stock solutions were freshly prepared every day.
All reaction mixtures were prepared in duplicate.

4.2.4 Incubation of Hb with Oxaliplatin and Cisplatin

Samples containing a fixed concentration of Hb (10μmol/L) and different
concentrations of oxaliplatin and cisplatin (0-100μmol/L) were incubated at
37°C for a maximum of 3 days. The concentrations of the drugs used in this
study were below and above the drug content in the blood. The solutions of Hb,
oxaliplatin and cisplatin were prepared in 0.1M phosphate buffer pH 7.4
containing 10 μ mol/L NaCl. The pH values of all reaction mixtures were

maintained at pH 7.4 to mimic physiological conditions. The molar ratios of the incubated protein:drug solutions were 1:1, 1:10, 1:50 and 1:100. The high drug-protein ratios were used to ensure the complete (equilibrium) binding conditions.

4.2.5 Preparation of Erythrocyte Samples from Patients and Healthy Volunteers

Blood samples from colorectal and lung cancer patients were collected 1 and 48 h after the first infusion of oxaliplatin⁴². The dosage of oxaliplatin was 100 mg/m² in 500 mL of 50g/L dextrose in water, infused over 120 min. Written informed consent was obtained from the patients. The protocol was reviewed and approved by the Research Ethics Board of the Alberta Cancer Board. In addition to the samples from cancer patients, blood samples from healthy volunteers were also collected as controls. Wholeblood samples from both patients and volunteers were collected in lithium heparin-coated tubes. All samples were centrifuged at 2500g for 15 min. The erythrocyte layer was separated from the plasma layer according to the published method⁴³. The erythrocyte and plasma samples were placed separately in cryovials and then stored at -35 °C until analysis.

4.3 Results and Discussion

4.3.1 Oxaliplatin- Hb interaction

The applicability of the CIEF-WCID technique for the study of the

interaction of two anticancer drugs (cisplatin and oxaliplatin) with Hb at near physiological conditions was evaluated. For this work, mixtures containing a constant concentration of Hb (10 μ mol/L) and different concentrations of oxaliplatin (0-100 μ mol/L) were incubated at 37°C for a variety of incubation periods. The experiments in this study were performed in parallel with a control Hb sample (drug free Hb), incubated under the same conditions as the sample mixtures. The reaction mixtures of Hb-oxaliplatin were injected into the separation column by pressure using a syringe.

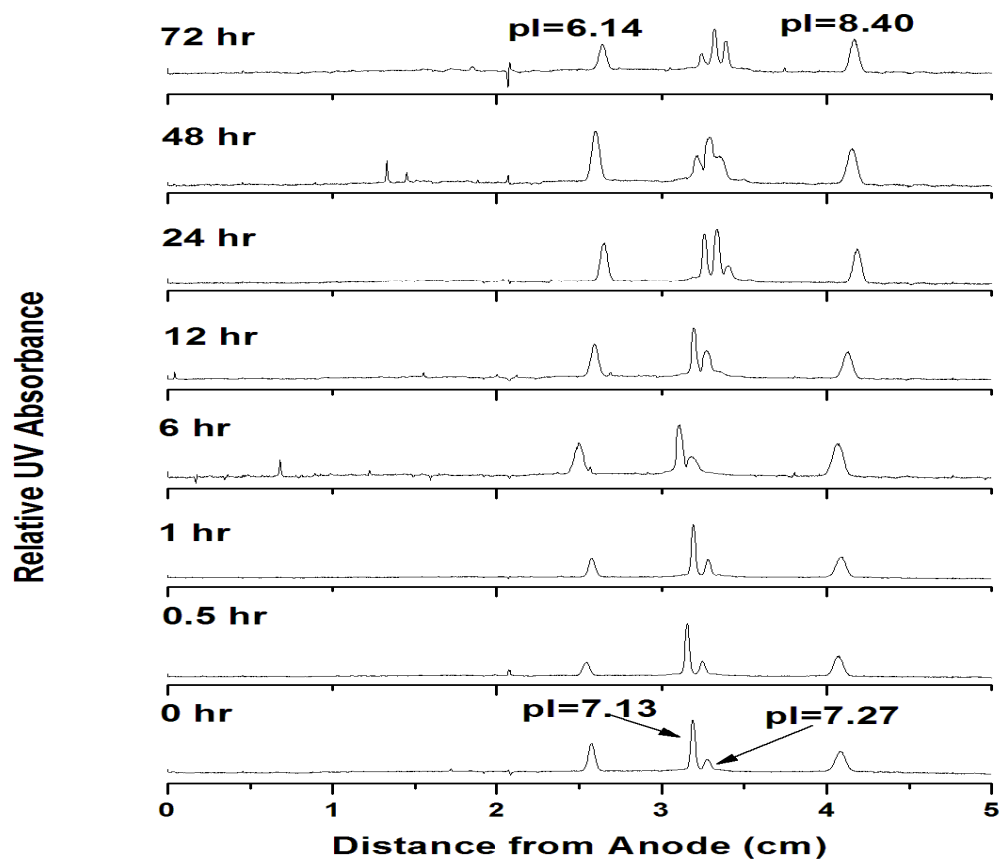


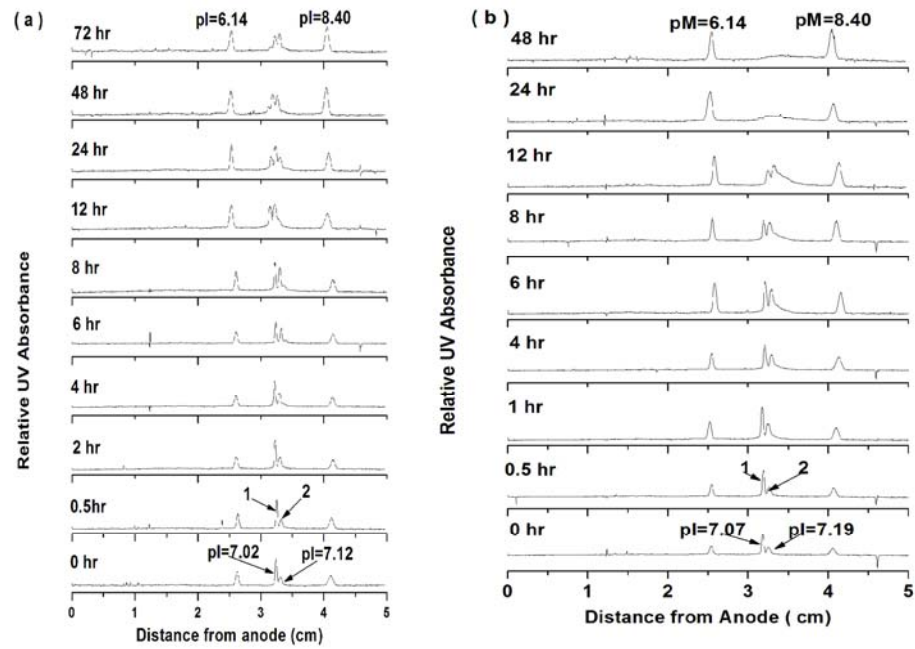
Figure 4-3. The CIEF analysis of Hb A₀ (10 μmol/L) incubated for 3 days at 37°C. For the CIEF analysis, a sample solution (400 μL) containing 2% pharmalytes (pH 3.0-10.0), pI markers (pI 6.14 and 8.40) and 0.5% pvp was injected into the capillary by pressure using a syringe. The catholyte and anolyte were 100mM NaOH and H₃PO₄ consecutively. The focusing voltage was set at 500V for 2min and 3000V for the remainder of the focusing period.

Figure 4-3 illustrates drug free Hb (control) separated by CIEF containing two pI markers (6.14 and 8.40). It should be mentioned that the two pI markers were used to observe possible pI shifts during the incubation

progress. In the absence of the drug, the electropherogram contains two distinctive peaks, which are characteristic of Hb. The pI values of the two peaks are 7.13 and 7.27. As shown in Fig.4-3, no structural change was observed for the first 12 hours of the incubation period. However, as time progressed (after 24 h), the two peaks began to change profiles and a third peak became visible. This may suggest that the surface property of Hb was altered.

The CIEF profiles for the reaction mixtures that contained Hb-oxaliplatin, is shown in Figure 4-3(a-d) . On the basis of the CIEF profile in Figure 4-3, two peaks are identified as the major components of Hb and focused at the pI (7.13 and 7.27). Figure4-3a-b shows the electropherograms of the incubated reaction mixtures with two molar ratios, 1:1 and 1:10. The Hb-oxaliplatin incubated in a 1:1 molar ratio exhibited the same pattern and similar pI values as the control sample (Fig. 4-2). However, the intensities of the three peaks, which appeared after 12 h, are lower compared to the control. Short-term (0-8h) incubation of Hb with oxaliplatin metabolites in a 1:1 ratio did not exhibit a significant change in the protein structure, whereas longer incubation periods (12-72h) resulted in a distortion of the complex. This indicates the stage at which the adduct is formed between the two analytes. In contrast, although a similar CIEF profile was observed during the first 8h in the sample with a 1:10 ratio, peak distortion and degradation of the adducts occurred after 12h. When the incubation time reached 48h, the adduct peak completely vanished. This clearly illustrates the formation of Hb-drug adducts and the change in pI of the protein. The observed pI change is estimated to be of the order of 0.006-0.19 pH units (Table 4-1). One

possible explanation for the disappearance of the peak is that it results from the loss of iron or the heme group resulted the conformational change of the protein. It has been suggested that the target protein can be adducted by multiple reactive species ⁴⁴.



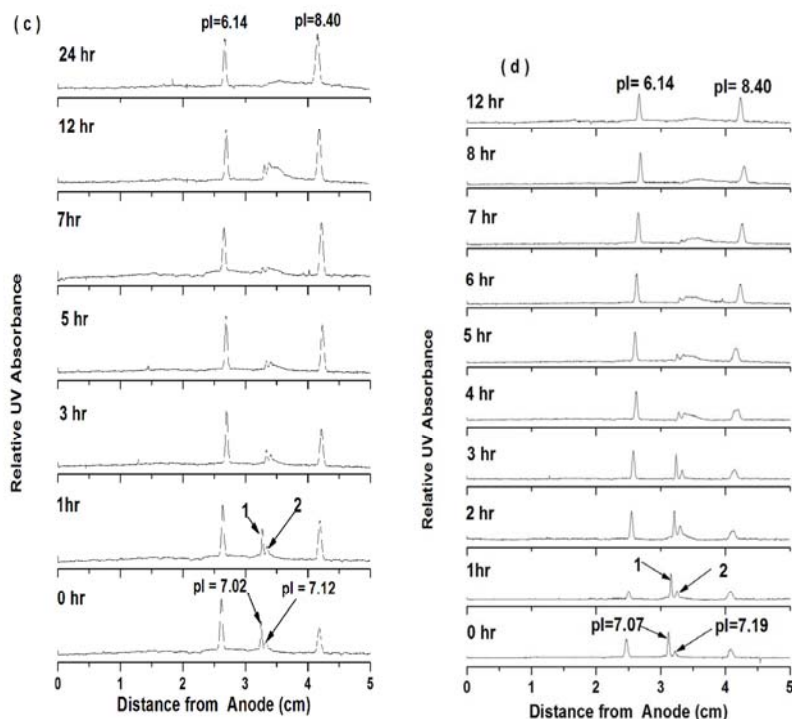


Figure 4-4. Electropherograms representative of binding of human hemoglobin A₀ with oxaliplatin : (a) 1:1 ; (b) 1:10 ; (c) 1:50 and (d) 1:100 molar ratios . The drug-protein mixture were incubated for 3 days at 37°C. Appropriate amounts of the incubated samples were removed and mixed with 0.5% PVP, 2% pharmalytes (pH 3.0-10.0) for each CIEF run. Catholyte and anolyte were 100mM NaOH and H₃PO₄.

The pI shift and the drug-induced disappearance of the peaks, provide striking evidence of strong and kinetically fast interactions of the protein with oxaliplatin. The time dependent decreasing pattern was observed for all peaks, along with progressively decreasing peak intensities (Fig 4a-b). As the drug-protein ratios approached saturation of the protein binding site, the peaks became

broader and distorted. The peak broadening suggests that the formation of multiple protein-drug complexes is possible in the presence of increasing amounts of the drug. These data may provide some insight into how high dosages of the drug affect the structure of Hb.

Having demonstrated the formation of adducts between Hb and oxaliplatin at 1:1 and 1:10 molar ratios, we further explored the analysis of binding interactions involving the formation of Hb-oxaliplatin complexes at higher molar ratios (1:50 and 1:100). In contrast to the previous experiment, the effect of oxaliplatin was substantially greater than that seen at lower molar ratios. As shown in Figure 4c-d, there is a concentration and time-dependent disappearance of the protein adducts. Although the CIEF profiles of the two incubation ratios appear similar, the degradation kinetic of the adducts exhibit a minor difference between the two samples. According to the CIEF profiles, for higher molar ratios (1:100), significant adduct formation is observed after 60 min of incubation, at which point changes in the peak shapes and intensities were observed (Figs4-3a and 4-4). The changes resemble those observed in Figure 4b. The transformation continues for the first 4 h, before the adducts start to disappear rapidly, which suggests that the drug-protein ratios are approaching saturation of the protein binding sites. According to the CIEF profile, when the incubation time reached 7 h, the protein adducts vanished completely. This phenomenon was also observed for the sample at a 1:50 molar ratio (Fig 4-4c). However, significant differences were observed between the two reaction mixtures on the kinetics of the drug-protein adduct formation. For example, in

the case of the 1:50 molar ratio sample, the altered CIEF profile of the adduct was observed after 12 h of incubation (Figure4-4c). Conversely, complete transformation of the adducts was observed for the sample with the 1:100 molar ratio.

It should also be noted that no new peaks were observed in both CIEF profiles. The marked effect observed for the higher incubation ratios strongly depends on the quantity of the drug in the sample. Therefore, it is not surprising that the kinetics of adduct formation was faster for higher incubation ratios. The pI values for the two peaks were slightly higher than the control (Fig.4-3). This indicates that as the level of the drugs increases, the adducts may decompose or be converted to non-absorbing species, which are no longer visible on the CIEF profiles.

4.3.2 Cisplatin- Hb interaction

The final phase of the study involved the evaluation of the interaction between cisplatin and Hb . The CIEF profiles of Hb-cisplatin, including the two pI markers (6.14 and 8.40), is shown in Figures 4-5. Cisplatin transforms to positively charged aquated species $[(\text{NH}_3)_2\text{PtCl}(\text{H}_2\text{O})]^+$ ^{34 11} when in contact with water. Both these aqua species and the parent drug are responsible for the reaction and binding properties of cisplatin. This agrees with previous observations achieved by other methods^{19, 29}.

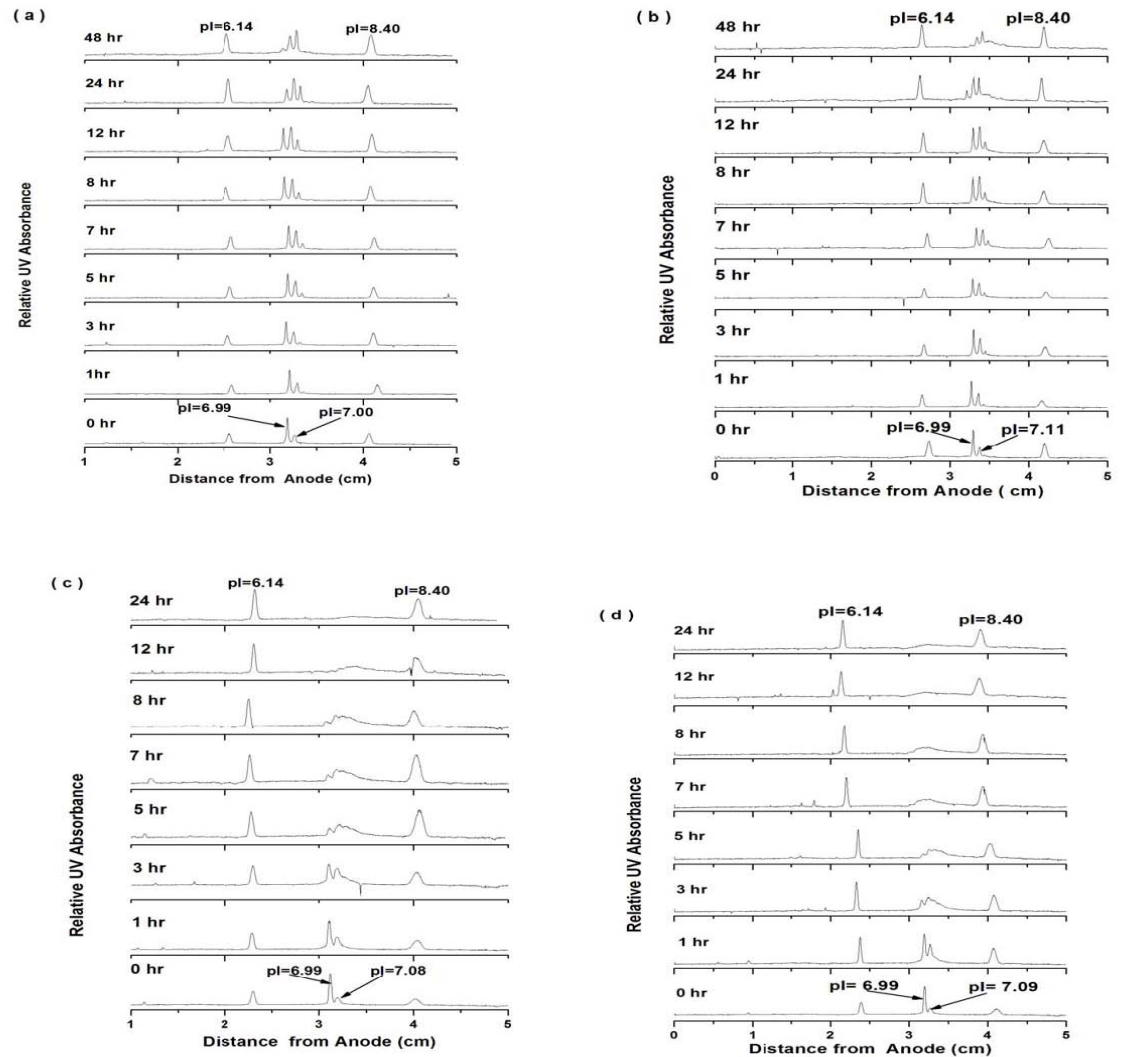


Figure 4-5. CIEF electropherograms of human hemoglobin A₀ incubated with cisplatin for 2 days at 37°C, at (a) 1:1; (b) 1:10; (c) 1:50 and (d) 1:100 molar ratios. Separation conditions as given in Section 2.2 (i.e. cisplatin, 10µmol/L; Hb A₀ , 0-100 µmol/L; 2% pharmalytes , pH 3-10;0.5% pvp; pI markers, pI 6.14 and 8.40; catholyte, 100mM NaOH; anolyte, 100mM H₃PO₄). The observed pI variations may rise from small changes of the capillary inner wall properties during successive runs. Separation voltage was set to 500 V for 2 min and 3000 V for the remainder of the time. For peak identification, see Table 4-1.

As has been previously described, the amount of covalent binding between Hb and cisplatin increases almost linearly as the incubation period increases (Fig4-5). As observed with the previous profiles, the formation of the protein adducts begins after 60 minutes of incubation (Fig4-5). Figure 4-5(a-b) shows the CIEF profile of cisplatin-Hb interaction at 1:1 and 1:10 molar ratios. The peak profiles of the cisplatin-Hb adduct reveal several intriguing differences compared to oxaliplatin-Hb at the same molar ratios. For the Hb-cisplatin complex (1:10 molar ratio), adduct degradation was not observed (Fig. 4-5b) during the first 48h, whereas the Hb-oxaliplatin complex at the same molar ratio vanished after 24h (Fig4-5b). This suggests that cisplatin demonstrates a weaker affinity to Hb compared to oxaliplatin, though the formation of the third adduct is observed consistently in both CIEF profiles (Fig 4-5(a-b)). The most likely explanation is that cisplatin may have other targets of action compared with oxaliplatin⁴⁵. In contrast, the Hb-oxaliplatin interaction at the same ratio produces only two peaks, except at 24 and 48 hrs (Fig4-2a). However, as a result, the intensities of these peaks are relatively weak. Similar differences were observed for higher incubation ratios (1:50 and 1:100).

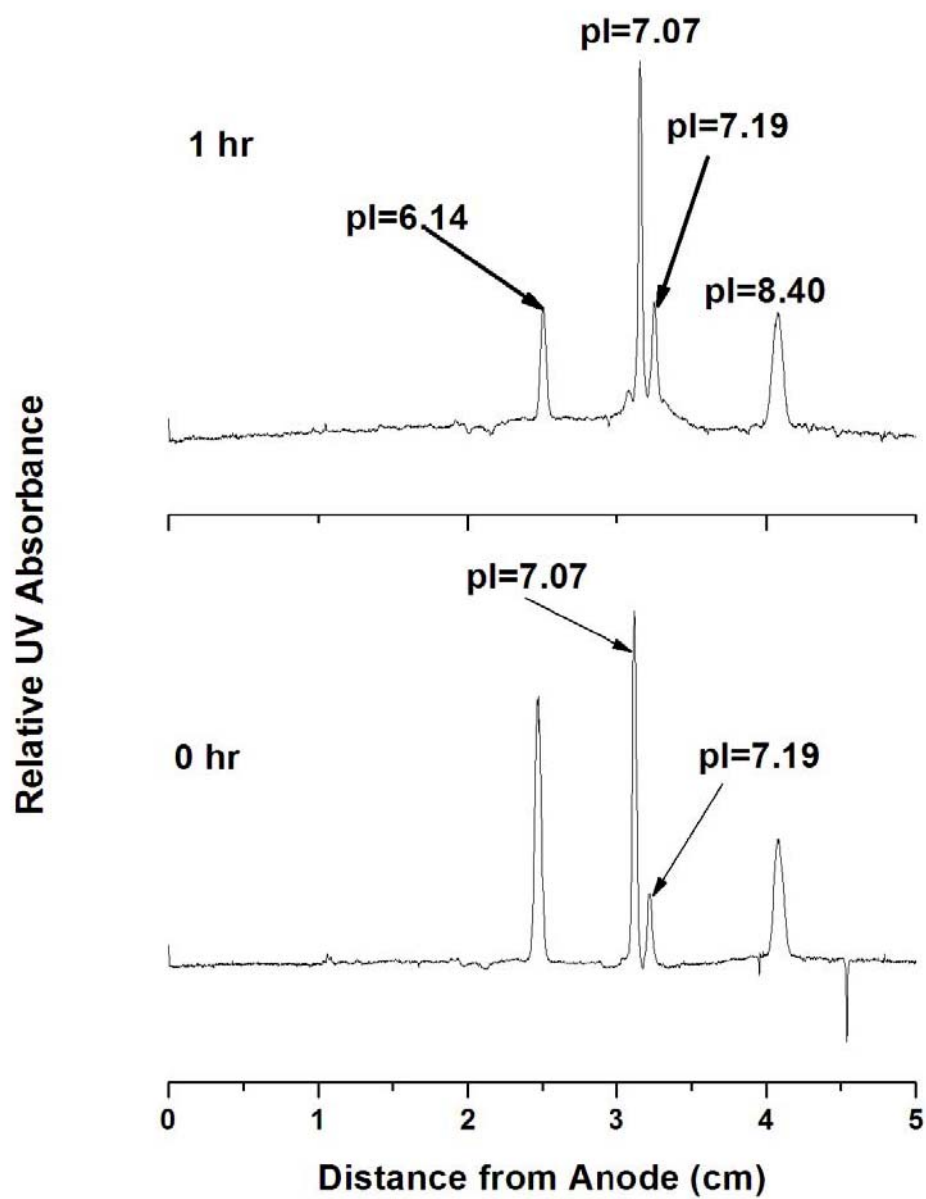


Figure 4-6. CIEF of Hb (1:100 ratios) incubated with oxaliplatin for 0 and 60 minutes at 37°C. The profiles displayed change of the peak area after 60 minutes incubation time. The separation conditions are described in Figure 4-4.

Figure 4c-d illustrates the CIEF profiles for the higher reaction mixtures (1: 50 and 1:100). The profiles in Fig. 4-5 further confirm the formation and transformation of adducts between cisplatin-Hb as the concentration of the drug increases.

Table 4-1. Experimental values of the pI shifts of Hb after Hb-oxaliplatin adducts formation.

Sample	Incubation ratio	Incubation time (h)	pI	
			Peak1	Peak2
Hb-Oxaliplatin	1:10	0	7.07	7.19
		0.5	7.10	7.20
		4	7.13	7.25
		12	7.18	7.28
	1 :50	0	7.02	7.12
		1	7.05	7.16
		3	7.13	7.23
		12	7.10	7.21
	1:100	0	7.07	7.19
		1	7.12	7.25
		4	7.32	7.41
		12	NA	NA

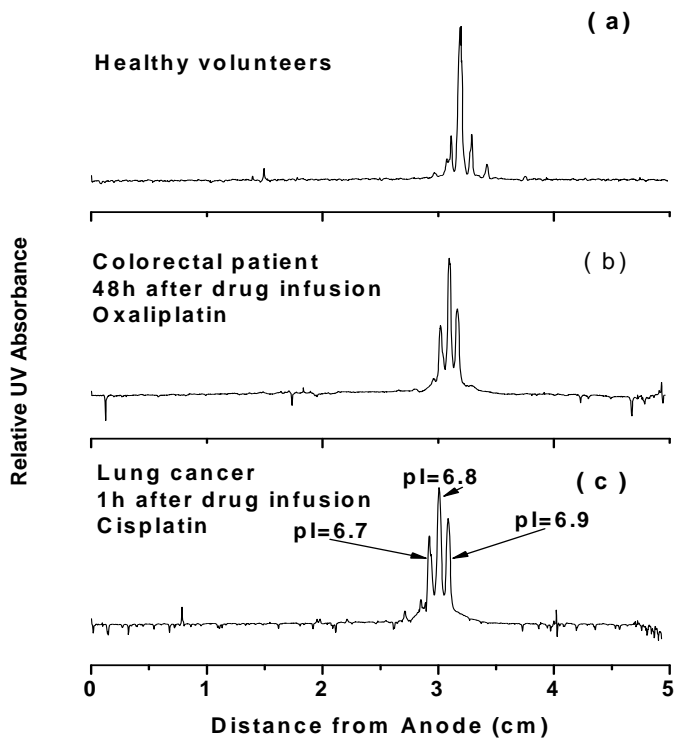


Figure 4-7. CIEF profile of Hb from cancer patients (lung and colorectal) undergoing oxaliplatin and cisplatin treatment : (a) from healthy volunteers; (b) colorectal; (c) lung cancer.

4.3.3 Cisplatin and oxaliplatin – adducts in Erythrocytes of Cancer Patients undergoing oxaliplatin and cisplatin treatment

We further investigated the formation of Hb with oxaliplatin and cisplatin adducts by analyzing erythrocyte samples from cancer patients and from healthy volunteers. Figure 4-7 is a typical CIEF profile of erythrocyte samples from a healthy volunteer (Fig4-7a) and from a patient obtained 1h (Fig4-7c) and 48h (Fig4-7b) after infusion of oxaliplatin and cisplatin. The

most comprehensive studies regarding the biotransformation of oxaliplatin and disposition in cancer patients were conducted in multiple matrices is reported by several researchers². CIEF analysis of the erythrocyte sample from a healthy volunteered showed only the intact Hb and no adducts with the two drugs. Erythrocyte samples from the patients undergoing oxaliplatin and cisplatin treatment clearly showed the Hb-adducts. Figure 4-7 shows that at a clinical relevant concentration formed three major complexes (one major and two minors) after 1 and 48h of the drugs infusion , whereas erythrocyte from healthy volunteered shows only two peaks. These two peaks which are typical peaks of human hemoglobin (Fig 4-7a) have a pI 6.9. Other minor peaks also observed in the same profile, which are representing the isomers of human hemoglobin A_0 which consist of five isomers in total. Similar result were obtained when oxaliplatin (0.05-0.5 μ M) and cisplatin were incubated with a fixed protein concentration 5.0×10^{-5} M Hb for variety of incubation times (Fig 4-5(a-d)). As it can be observed, with the increase of oxaliplatin and cisplatin concentration, the amount of Hb-drug complexes increases (Fig4-5). In the present work, the results obtained agreed with the our previous work , which allows the implementation of this methodology as a simple and a robust method for characterization of the protein-drug interaction, which is of a great importance in the development process of new drug. From the results obtained it can be deduced that oxaliplatin and cisplatin show great affinity toward Hb .By comparing the binding properties of drugs to Hb⁴⁶ and HSA (chapter 5), it was

concluded that both proteins are responsible for the binding of drugs.

4.4 Conclusion

Measurement of the interaction between a drug and a protein by CIEF-WCID is a simple and reliable technique. The interaction of Hb with oxaliplatin and cisplatin has been successfully determined using CIEF-WCID with a relatively simple system. It should be noted that the proposed technique only allows separation of Hb-drug adducts and a determination of the pI shift of the protein. The method can be considered as a complementary rather than a competitive technique, because the method exhibits specific ranges of applicability, advantages and disadvantages. For instance, with nano-ESI-MS/MS, the dissociation constant and binding sites may be determined, while with CIEF only adduct formations and pI shifts are observed.

On the basis of the CIEF profiles of Hb –cisplatin and Hb-oxaliplatin produced in this study, there are significant differences in binding patterns between oxaliplatin and cisplatin with Hb, presumably due to the differences in reaction species and reaction targets. From the results presented herein, we deduce that oxaliplatin shows a greater affinity towards Hb, while cisplatin binds less strongly. For both drugs, incubation with Hb for longer durations and at higher drug concentrations results in higher levels of adduct formation and destabilization of the Hb structure. Furthermore, a pI shift is observed only with the oxaliplatin-Hb CIEF profiles (Table 1). These experiments confirm the validity of CIEF as a simple and convenient method for investigation of protein-drug interactions.

In addition, blood samples collected from colorectal and lung cancer patients were characterized and compared with the sample from healthy volunteers by using CIEF method. From the observed results, it is concluded that this method is a valid method of determining the binding characteristics of drug to protein *in vivo* and *in vitro* and the method provided a fast and simple technique for the study of drug-protein interaction. Furthermore, it has been shown , the presented method can be used to study binding of drugs to proteins *in vivo* under physiological conditions following dosing.

CHAPTER 5

HUMAN SERUM ALBUMIN INTERACTION WITH OXALIPLATIN STUDIED BY SPECTROSCOPIC METHOD AND CAPILLARY ISOELECTRIC FOCUSING WITH THE WHOLE COLUMN IMAGING DETECTION

5.1 Introduction

Capillary isoelectric focusing (CIEF) provides high resolution separation of amphoteric biomolecular species based on differences of their isoelectric point in a pH gradient formed by carrier ampholytes when an electric potential is applied ¹. This high-throughput technique offers greater resolving power and has become a standard method for analysis of protein and protein-ligand interaction. The utilization of the whole column detection approach with UV WCID gives this separation technique a unique advantage over the conventional single point detection ¹⁻⁴. For example, in single point detection, several problems are encountered during the sample mobilization process, including protein precipitation, long analysis time and distortion of pH gradient. In contrast, CIEF-WCID successfully eliminates the mobilization process by using the WCID technique.

Thanks to the advantage of on-column detection and the capability of attaining real-time monitoring of the changes in peak area, CIEF-WCID is suitable for protein-protein and protein-drug interactions. Recently, CIEF-WCID has been successfully applied in our group to investigate protein-DNA ⁵,

protein-amino acid ⁶ and protein-lipid ^{3, 7-9} interactions. Furthermore, we demonstrated the use of this technique to determine the molecular weight of unknown proteins ¹⁰. CIEF-WCID is expected to make a unique contribution in proteomic research because of its ability to resolve wide ranges of proteins and protein complexes that have small differences in *pI* in real-time. This technique is very important when one studies protein-ligand interactions such as protein-protein, protein-DNA and protein-drug.

The development of efficient and sensitive analytical methods for the separation, identification and quantification of drug-protein adducts is paramount for understanding the drug activity and toxicity. The objective of the present study is to develop a CIEF-WCID to investigate the interactions of platinum-containing anticancer drugs, namely oxaliplatin, with a model blood protein, human serum albumin (HSA). The structural changes of HSA are investigated by monitoring the *pI* during the incubation of oxaliplatin with HSA. CIEF is the highest efficiency, single-dimensional separation method available for the investigation of the interaction between proteins and ligands. This technique offers a number of advantages, including speed, high separation efficiency, short analysis time and reduced sample consumption. Although the CIEF technique shows a number of advantages, quantitative information was chiefly provided by other techniques.

To our knowledge, the investigation of oxaliplatin interaction with HSA by CIEF with WCID is the first report of this type of analysis. The development of a simple and reliable method to study drug-protein interactions is of great

practical and theoretical importance.

Platinum-based drugs are among the most active anticancer agents and have been widely used in the treatment of a variety of human tumours. Over the last 30 years, a large number of platinum analogues have been synthesized to enlarge the spectrum of activity, overcome cellular resistance and/or reduce the toxicity of both first (i.e. cisplatin) and second generation (i.e. carboplatin) platinum drugs ¹¹. Of these platinum-based compounds, oxaliplatin, a novel compound containing a trans-1-(R,R)-1,2-diaminocyclohexane (DACH) carrier ligand, has recently been approved for the treatment of metastatic colorectal carcinoma in conjunction with fluoropyrimidines ¹². Oxaliplatin has shown *in vitro* and *in vivo* efficacy against many tumor cell lines and tumours, including those that are resistant to cisplatin and carboplatin ^{11, 13-15}. In addition to its positive effects oxaliplatin also shows several toxic effects. The main cumulative dose-limiting toxicity of oxaliplatin is progressive peripheral sensory neuropathy ^{16, 17}. It is also associated with an acute mild neuropathy, which reverses in several hours or days ^{16, 17}. Oxaliplatin can also produce diarrhea, vomiting and haematological suppression¹⁷⁻¹⁹. However, the mechanisms of action and toxicity are not clear.

Platinum-containing anticancer drugs are believed to induce apoptosis in cancer cells by covalently binding to DNA ²⁰⁻²², however, they also react with a number of proteins and peptides, such as glutathione, which may also play a role in detoxification of oxaliplatin ²³. In addition, after these drugs are introduced intravenously, 65 – 98% of the drugs are bound to blood plasma

proteins ²⁴⁻²⁶, and 40% of the blood platinum is found in erythrocytes ^{26, 27}. While it is widely accepted that platinum-DNA adducts are responsible for the drug's cytotoxicity, the role of platinum-protein adducts in the mechanism of action and toxicity of the drug remains unclear. Platinum-protein adducts are suggested to be the cause of the drug's side effects; however, there are also claims that they are important to the drug's activity ²⁸. Therefore, information on how anticancer drugs interact with proteins is important for the understanding of the mechanisms of action and toxicity of a drug and the optimization of cancer treatments.

HSA is an abundant protein that binds a variety of ligands with a typical concentration of 35-45 g/L. HSA interferes with certain antitumour drugs, changing their biological activity and affecting clinical activity ²⁹. In plasma, this protein is responsible for distributing and metabolizing many endogenous and exogenous ligands such as fatty acids, bilirubin, colic acid, metal ions, steroid hormones and pharmaceuticals, including metallodrugs ^{20, 24, 29-38}. HSA contains 585 amino acids and has a molecular weight of 66,500 Da. The crystal structure shows ligand binding sites located in the hydrophobic binding pockets in subdomains IIA and IIIA, each of which contains two subdomains (IA, IB, etc) and is stabilized by 17 disulfide bridges and one free thiol at Cys-34 ³⁹. HSA contains a single tryptophan (Trp) residue in position 214 in subdomain IIA. At physiological pH (7.4), HSA presents two structural isomers: N and B. Ligand binding one of the domains (II or III) induces conformational changes on the other domain since both domains share a common interface. At

pH 7.4, HSA tends to interact with positive species due to negatively surface charge⁴⁰. The molecular interaction between HSA with platinum-based anticancer agents have been extensively studied by variety of analytical and spectroscopic techniques^{29-32, 34, 36, 41, 42}.

In recent work, we investigated the effect of cisplatin and oxaliplatin on human hemoglobin⁴³ and described the adducts formation between the two analytes.

5.2 Experimental

5.2.1 Chemicals

Oxaliplatin (99.9%), carrier ampholytes (Pharmalytes 3.0-10.0) and HSA were purchased from Sigma (St. Louis, MO, USA). Polyvinylpyrrolidone (pvp) was purchased from Aldrich (Milwaukee, WI, USA). Water was purified with a NANOpure water system (Barnstead/Thermolyne, Dubuque, IA, USA) and had a minimum resistivity of 18.0 MΩ-cm. All of the chemicals employed in this study were of analytical reagent and used without further purification.

5.2.2 Solutions and sample preparation

Stock solutions of oxaliplatin (trans-1-(R,R)-1,2-diaminocyclohexane(DACH) oxalatoplatinum) were prepared to a concentration of 5 mmol/L. The HSA stock solution was prepared to a concentration of 25 μmol/L. The stock solutions were freshly prepared everyday. All reaction mixtures were prepared in duplicate.

5.2.3 Incubation of HSA with oxaliplatin

Samples containing a physiological concentration of HSA (5.0×10^{-5} mol/L), tryptophan (5.0×10^{-5} mol/L) and different concentrations of oxaliplatin (0-100 μ mol/L) were incubated at 37°C in a phosphate buffer solution (0.1 M pH 7.4) containing 10 mol/L NaCl for a maximum of three days. The pH values of all of the reaction mixtures were maintained at 7.4 to mimic physiological conditions. The molar ratios of the incubated protein:drug solutions were 1:1, 1:10, 1:50 and 1:100, respectively. Aliquots were taken for analysis after 0, 0.5, 1, 2, 6, 12, 24, 48 and 72 h.

5.2.4 Preparation of metal colloid

The colloid solutions used in this study were prepared according to the description of Lee and Miesel⁴⁴. The silver solution was prepared by the standard citrate reduction by dissolving 90mg (AgNO_3) in 500mL of H_2O and brought to boiling. A solution of 1% sodium citrate (10mL) was added. The solutions then diluted with water in the ratio of 1:7. The absorption spectrum of this brownish solution has a maximum at 500nm (Fig 5-9). This colloidal suspension was stable for several weeks and was stored in the dark.

5.2.5 Characterization of silver colloids

AFM images were obtained by measurement of the force on a sharp tip created by the proximity to the surface of the sample⁴⁵. This force is kept small and at a constant level with a feedback mechanism. When the tip is moved sideways it will follow the surface morphology.

AFM of colloid images were performed by Jin Xu at the Department of Chemistry, University of Waterloo.

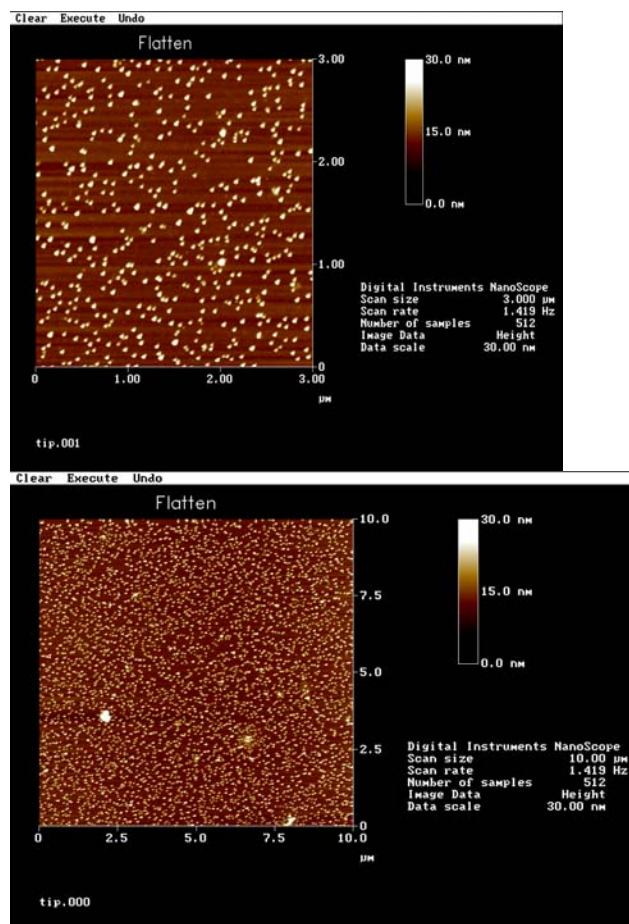


Figure 5-1. Atomic force microscopy (AFM) topographic and lateral force images of the silver nanoparticles.

5.2.6 CIEF System

The CIEF experiments were pursued with a commercial iCE₂₈₀ instrument (Convergent Bioscience, Mississauga, ON, Canada). The system was equipped with a charge couple device (CCD) camera for image collection. Separations were performed on commercial cartridges with silica capillary tubes

(Convergent Bioscience), with an effective length of 5 cm, 100 μm i.d. and 200 μm o.d. The capillary wall was coated with fluorocarbon (Restek, Bellefonte, PA, USA) to suppress the electroosmotic flow (EOF). Focusing was carried out for 2 min at 500V and the system was set at 3000V for the remainder of the analysis. The catholyte and anolyte contained 1% pvp with 100 mM NaOH and 100 mM of H_3PO_4 , respectively. The sample, which was mixed with 0.5% pvp and 2% ampholyte (pH 3-10), was manually injected with a needle. To avoid inconsistent coating efficiency, all capillaries were dynamically coated with additives for 30 minutes prior to the experiment. During the focusing process, the current was decreased from 10.8 μamp to 4.7 μamp , prior to completion.

5.2.7 UV/Vis absorption measurement

UV-Vis spectra were recorded on Ultrospec 2100 Pro UV-Visible spectrometer in a 1 cm cuvette. Freshly prepared HSA and oxaliplatin solutions were mixed in 1:n ratios (n is integer, varies from 1 to 100). The tryptophan solution ($5.0 \times 10^{-5} \text{ mol L}^{-1}$) was prepared in pH 7.40 phosphate buffer. The UV-Vis spectra were scanned in the range of 200–600 nm.

5.2.8 Fluorescence quenching measurement

The fluorescence emission spectra of HSA in the presence of oxaliplatin were recorded on a PTI QuantaMaster Instrument equipped with a xenon lamp source and 1.0 cm quartz cell with a thermostat bath. Fluorescence quenching spectra were collected by recording the fluorescence emission wavelength from

300 to 500 nm at an excitation wavelength of 390 nm, and with the slit width 5.0 nm. Freshly prepared HSA and oxaliplatin solutions were mixed in 1: n ratios as previously described above.

5.3 Results and Discussion

5.3.1 CIEF Investigation of Oxaliplatin- HSA Interaction

We have developed a CIEF technique to investigate the adduct formation between HSA and oxaliplatin in aqueous media, mimicking physiological conditions. The standard CIEF profile of HSA showed one peak (Fig5-1). The focusing time took 8 min. Within the 8 min focusing time, no peak distortion or intensity changes were observed. However, the peak area gradually started changing with a minor increase of the incubation ratio, and with higher oxaliplatin concentrations, the peaks altered drastically and diminished, which indicates the adduct formation between the two analytes. Figs 5-1 and 5-2 show typical CIEF separation profiles for HSA (control) and HSA-oxaliplatin adducts in buffer solution. This result is in excellent agreement with previous hemoglobin-oxaliplatin studies, which demonstrated that oxaliplatin induces structural alterations when incubated with HSA.

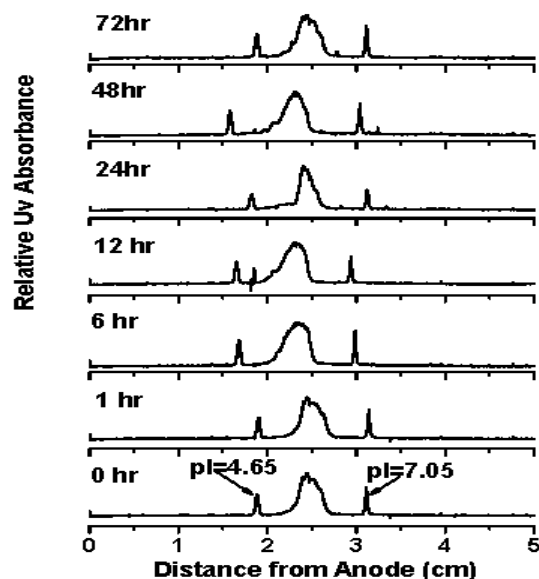


Figure 5-2. The CIEF analysis of HSA ($10\mu\text{mol L}^{-1}$) incubated for 72 hr at 37°C . For the CIEF analysis, a sample solution ($400\ \mu\text{L}$) containing 2% pharmalytes (pH 3.0-10.0), pI markers (pI 6.14 and 8.40) and 0.5% PVP was injected into the capillary by pressure using a syringe. The catholyte and anolyte were $100\ \text{mmol L}^{-1}$ NaOH and H_3PO_4 consecutively. The focusing voltage was set at 500 V for 2 min and 3000 V for the remainder of the focusing period. The observed pI variations may arise from small changes of the capillary inner wall properties during successive runs.

Fig5-2 illustrates drug-free HSA (control) separated by CIEF containing two pI markers (4.65 and 7.05). It should be mentioned that the two pI markers were used to observe possible pI shifts during the incubation progress. In the absence of the drug, the electropherogram of HSA contains only one distinct peak, which is characteristic of this protein. The pI value of HSA is

approximately 5.7. However, a minor fluctuation can be observed due to an inconsistency in the manufacturing of the separation cartridges and focusing time. As shown in Fig 5-3a, no significant change was observed for the first 6 hr of the incubation period. However, as the incubation time progressed from 6 to 12 hr, the peak intensity started to decrease accompanying an increase in peak width of the profile. A small *pI* shift is also observed in going from a 12 to 72 hr incubation time; this is most likely due to the early stage of adduct formation between the two analytes, accompanying the alteration of HSA surface properties.

The CIEF profile for the reaction mixtures that contain HSA-oxaliplatin (1:1, 1:10, 1:50 and 1:100 molar ratios), is shown in Fig 5-3(a-d). From Fig 5-3a, it is seen that as the incubation ratio reached 12 hr, the area of the CIEF profile of HSA increased, which indicates the stage at which the adducts start forming between the two analytes. However, the profile indicates no *pI* shift or structural change within the 72 hr incubation time. This indicates that the structural change was less evident at low drug concentration. From Fig5-2a, we also observed that the CIEF profiles are identical to that obtained in Fig5-1.

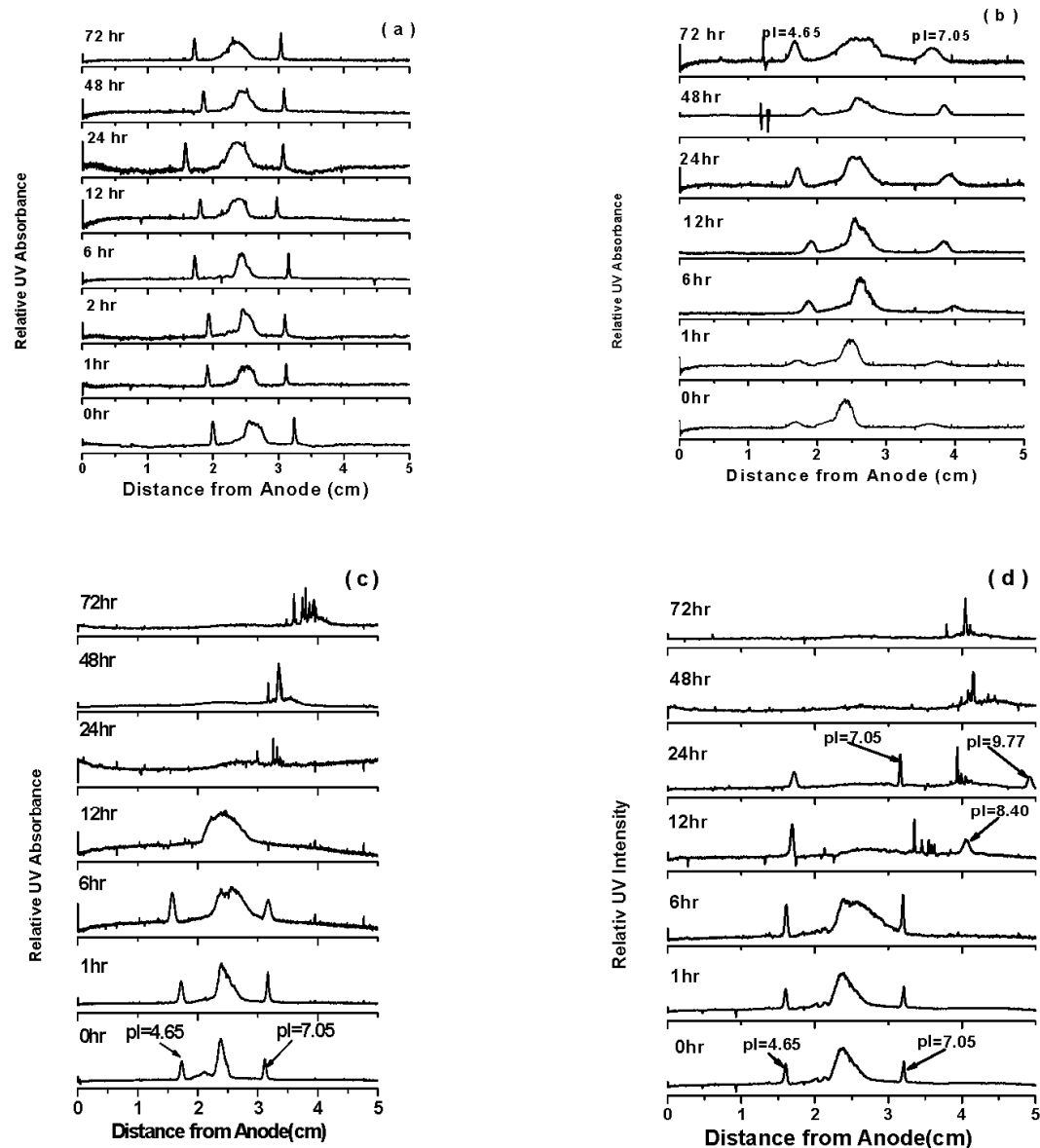


Figure 5-3. Electropherograms representative of binding of HSA with oxaliplatin: (a) 1:1 ; (b) 1:10 ; (c) 1:50 and (d) 1:100 molar ratios. The drug-protein mixtures were incubated for 3 days at 37°C. Appropriate amounts of the incubated samples were removed and mixed with 0.5% pvp, 2% pharmalytes (pH 3.0-10.0) and pI markers (4.65, 7.05, 8.40 and 9.77) for each CIEF run. Catholyte and anolyte were 100 mM NaOH and H₃PO₄. On electropherogram c

and d, the pI markers were not mixed with the running sample due the formation of fragments after 24 and 48hr incubation time. For all solutions, the total concentration of HSA was constant: $5.0 \times 10^{-5} \text{ mol L}^{-1}$. The separation conditions are described in Fig 5-1.

Figure 5-3(b-d) shows the CIEF profile of HSA-oxaliplatin adducts in 1:1, 1:10, 1:50 and 1:100 molar ratios, incubated at 37°C under the same CIEF conditions. The spectral profile of Figure 5-2b (1:10 molar ratio) shows the protein was markedly affected by the complexation with oxaliplatin. For short incubation times (0 to 6 h), in contrast to Fig 5-1 and Fig 5-2a, a minor pI shift was observed after 1 hr of incubation. Also shown in Fig. 2b is the increase of spectral width. When the incubation time progressed from 1 to 72 hr, the relative intensity of the peaks was decreasing as a function of incubation time. Although the pI shift was not significantly changed between the time frame of 12 to 72 hrs, the drug induced structural alteration of the protein structure. This demonstrates the stage at which the adducts are formed between the two analytes. The decreasing intensity and increasing area of the CIEF profiles further demonstrate the effect of the drug on the protein structure. The pattern of the electropherograms recorded for samples containing 1:50 and 1:100 molar ratio of HSA-oxaliplatin showed substantial differences from the other samples (1:1 and 1:10 molar ratio). As shown in Fig 5-2(c-d), there is a concentration and time-dependent CIEF profile alteration and structural breaking down into fragments, or forming aggregates of the protein adducts. Although similar CIEF profiles were observed for the two incubation ratios, the degradation kinetics

show a minor difference between the two samples. In the case of Fig 5- 1c (1:50), the distortion of the protein adducts started after 6 hr of incubation time, followed by peak shape changes. These are the expected results since the sample contains a smaller amount of oxaliplatin compared to that of the 1:100 ratio. It can also be seen that the CIEF profile exhibits *pI* shift, suggesting that adducts form between the two analytes. As time progressed, the adducts formed completely dissociated after 12 h of incubation time, which suggests that the drug-protein ratios are approaching saturation of the protein binding sites. Previously, we had shown that there is a biologically significant interaction between protein (Hb A) and oxaliplatin⁴⁰. Similar behavior was observed when oxaliplatin incubated with Hb at the two ratios (1:50 and 1:100). However, for 1:100 molar ratio, the dissociation of the adducts starts after 6 hr, which suggested that the kinetic transformation was faster compared with the lower molar ratio, (1:50) . These two samples show very different behavior under the same separation conditions. One of the significant differences between the two samples was the relatively broader peak shape for the 1:100 molar ratios. This broader peak starts appearing after approximately 1 h of incubation time. When the incubation time reached 12 hr, the peak almost disappeared and the fragments of the adducts appeared. One possible explanation was that the formed adduct was breaking down or changing to other species as incubation time progressed. It has been shown in a number of previous studies that HSA contains platination sites such as Met, His, or S-S bonds³⁴. Since the S-S bridge is responsible for the stabilization of HSA, a high concentration of oxaliplatin

might cleave the S-S bridge. This may lead to the activation of the protein aggregate, which was observed in our experiments for the two higher incubation ratios (1:50 and 1:100).

5.3.2 UV/Vis spectra of HSA and HSA-oxaliplatin adducts

For reconfirming the structural changes of HSA upon complexation with oxaliplatin, the UV/Vis absorption spectra of HSA with various amount of oxaliplatin were collected. Similar to the previous investigations using CIEF-WCID, samples with 1:1, 1:10, 1:50 and 1:100 molar ratios were incubated for 1 hr at 37⁰C in a water bath. In parallel with HSA-oxaliplatin incubated mixtures, blank samples of HSA, oxaliplatin and tryptophan were investigated by similar techniques as a control. The two controls (HSA and oxaliplatin) demonstrate the maximum absorption at 278 and 255 nm. Thus, by comparing the peak intensities and the optical absorption with HSA-oxaliplatin adduct, the absorption profiles of the four analytes can be analyzed.

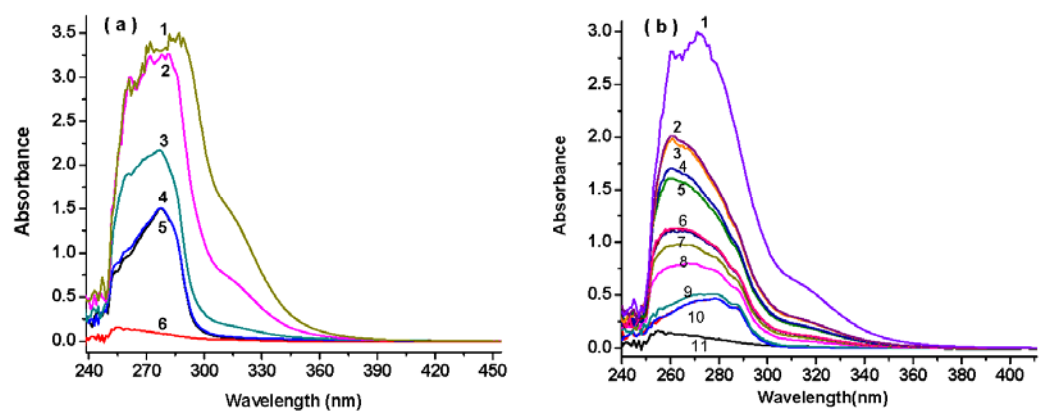


Figure 5-4. The absorption spectra of HSA and tryptophan in the presence of oxaliplatin incubated in phosphate buffer at room temperature. For all solutions, the total concentration of HSA was constant: $5.0 \times 10^{-5} \text{ mol L}^{-1}$ (a) HSA-oxaliplatin molar ratios at 0:1, 1:0, 1:1, 1:10, 1:50 and 1:100 incubated molar ratios; (b) Tryptophan- oxaliplatin mixtures were (curves 12 to 1): 1:0, 1:1, 1:2, 1:4, 1:6, 1:8, 1:10, 1:12, 1:14, 1:16, 1:18 and 1:20 molar ratios.

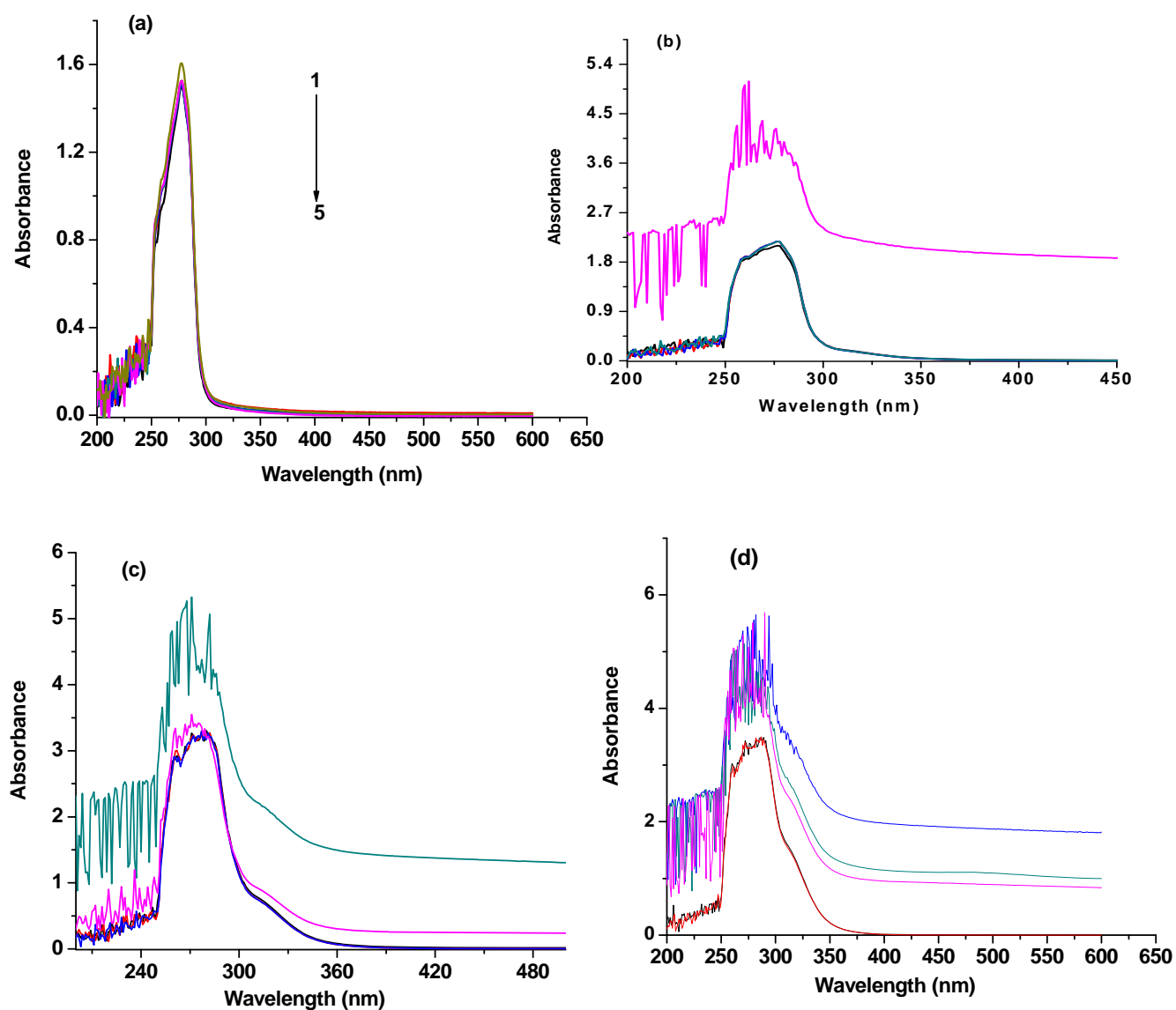


Figure 5-5. The UV/Vis spectra of HSA-oxaliplatin in (a) 1:1, (b) 1:10, (c) 1:50 and (d) 1:100 molar ratio and the reaction mixtures incubated for 0, 1, 6, 12 and 24hours at 37⁰C in water bath. The incubated buffer contained 5.0 x10⁻⁵M HSA with oxaliplatin concentration varied from 5.0 x 10⁻⁵ to 5.0 x 10⁻³mol/L.

Fig 5-4 demonstrates the optical absorption spectra of HSA-oxaliplatin reaction solutions at different molar ratios. In this study, at lower molar ratio

(1:1), which is a fairly close approximation to the real drug-protein proportions in blood, the drug effect was minimal. Fig5-4a shows the absorption spectrum of HSA incubated with oxaliplatin in a 1:1 molar ratio. The absorption spectra show no significant changes for this incubation ratio. However, the peak shape and intensity start to change upon increase of the drug concentration (1:10 molar ratio). This effect shows the beginning of the formation of adducts between the two analytes. Although the peak intensity was not significantly changed for 1:10 molar ratio for the first 24 h period, multiple peaks appeared as the incubation time progressed to 48 h. This result suggests that multiple forms of the adducts formed due to different conformations of the protein. It is also possible that the formed adducts are degraded after a higher incubation time was reached. These surprising results were also observed in higher incubation ratios of the CIEF-WCID studies. Having demonstrated the formation of adducts between HSA and oxaliplatin at 1:1 and 1:10 molar ratios, we further explored the analysis of binding interactions involved in the formation of HSA-oxaliplatin complexes at higher molar ratios (1:50 and 1:100). In contrast to the previous experiments, the effect of oxaliplatin was substantially greater than that seen at lower molar ratios. As shown in Fig5-4(b-c), for higher drug concentrations, the kinetic formation of adducts was faster for 1:100 molar ratios. This can be attributed to a very high drug concentration present in reaction solutions. It is important to note that such high drug to protein ratios were used to ensure the complete (equilibrium) binding. In addition, for the high incubation ratios (1:50 and 1:100), the amount of adducts

formed increased as the concentration of the drug increased, accompanied by baseline changes.

5.3.3 Fluorescence quenching spectra and quenching mechanism

Fluorescence quenching can be described by the Stern-Volmer equation ⁴⁶:

$$\frac{F_0}{F} = 1 + K_q \tau_0 [Q] = 1 + K_{sv} [Q] \quad (1)$$

Where F_0 and F are the fluorescence intensities in the absence and presence of the quencher, K_q represents the quenching rate constant, K_{sv} the Stern-Volmer dynamic quenching constant, $\tau_0 (10^{-8} \text{s})$ ⁴⁷ the average lifetime of the biomolecule without quencher, and $[Q]$ is the concentration of the quencher respectively. The K_{sv} and K_q values are calculated from the linear plot of F_0/F against the drug concentration, $[Q]$:

$$K_q = \frac{K_{sv}}{\tau_0} \quad (2)$$

There are two kinds of fluorescence quenching: dynamic and static. These two mechanisms can be distinguished from each other by their differing dependences on temperature and excited-state life time. The K_{sv} value decreases with an increase in temperature for static quenching, but there is a reverse effect

on dynamic quenching. For higher temperatures, the diffusion constant increases, due to the dissociation of weakly bonded complexes. It is well known that the maximum scattering collision quenching constant of various quenchers with biological macromolecules is about $2.0 \times 10^{10} \text{ l mol}^{-1} \text{ s}^{-1}$. For HSA-oxaliplatin as shown in Table 1, the quenching constant is much higher than $2.0 \times 10^{10} \text{ l mol}^{-1} \text{ s}^{-1}$. The K_{sv} decrease with temperature increased. Therefore, it can be concluded that the quenching was not initiated by dynamic collision but probably initiated by static quenching resulting from complex formation between HSA-oxaliplatin. The intrinsic fluorescence of HSA is essentially due to tryptophan alone, because phenylalanine has a very low quantum yield and the fluorescence of tyrosine is almost totally quenched if it is ionized or is near an amino group, a carboxyl group, or a tryptophan residue.

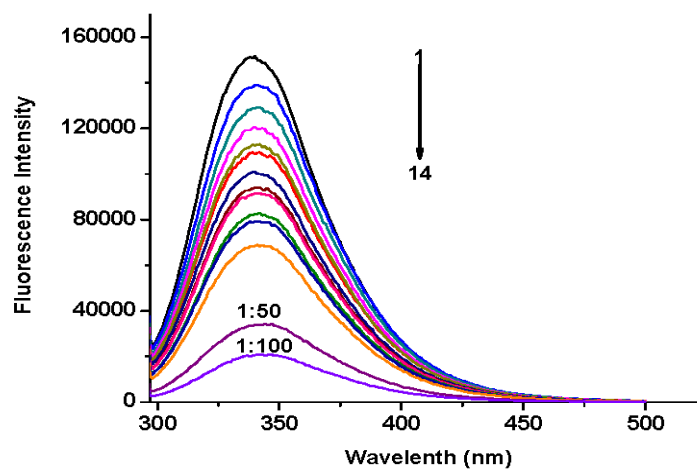


Figure 5-6. Fluorescence spectra of HSA ($5.0 \times 10^{-5} \text{ mol L}^{-1}$) in the presence of oxaliplatin ($5.0 \times 10^{-5} \text{ mol L}^{-1}$) at 47°C ; curves (1-14), 0, 1.0, 2.0, 4.0, 6.0, 8.0, 10.0, 12.0, 14.0, 16.0, 18.0, 20.0, 50.0 and 100.

Figures 5-5 and 5-6 show the fluorescence emission spectra for HSA with various molar ratios of oxaliplatin at pH 7.4, excited at 290 nm. As the data shows, the fluorescence spectra of HSA progressively decreased with the increasing concentration of oxaliplatin. These observations can be rationalized in terms of interactions between oxaliplatin and HSA and formation of complexes between the two analytes.

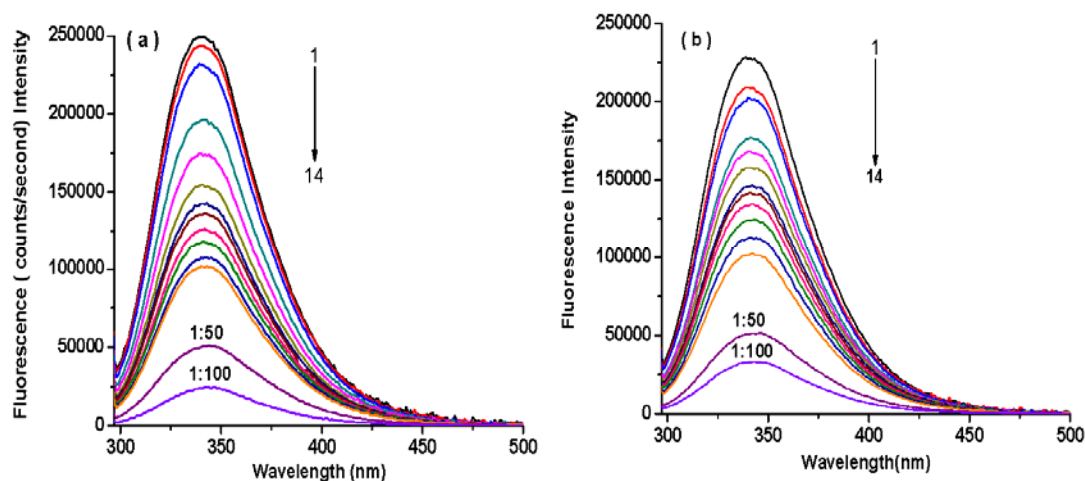


Figure 5-7. Fluorescence spectra of HSA ($5.0 \times 10^{-5} \text{ mol L}^{-1}$): oxaliplatin ($5.0 \times 10^{-5} \text{ mol L}^{-1}$): curves (1-14), 0, 1.0, 2.0, 4.0, 6.0, 8.0, 10.0, 12.0, 14.0, 16.0, 18.0, 20.0, 50.0 and 100.0, respectively; (a) 25°C , (b) 37°C

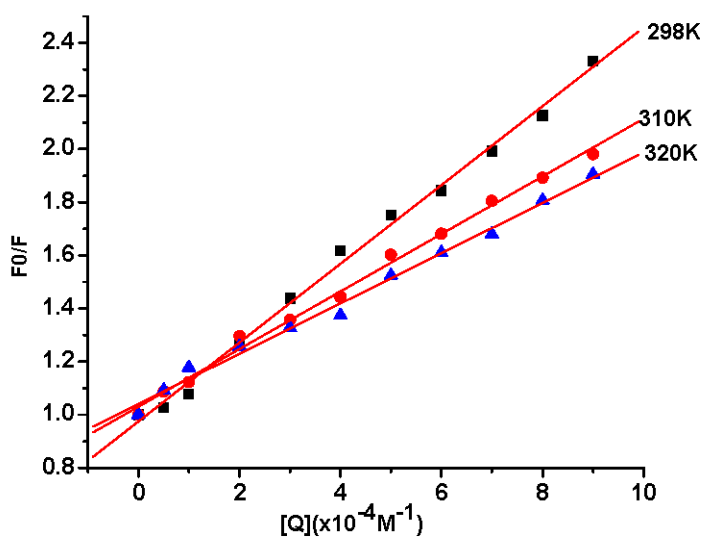


Figure 5-8. Stern-Volmer plot for the binding of HSA-oxaliplatin at different temperatures (298, 310 and 320K).

Table 5-1

Stern-Volmer dynamic quenching constants and quenching rate constant of HSA and oxaliplatin at different temperatures

pH	T(K)	$K_{SV}/l\ mol^{-1}$	$K_q/l\ mol^{-1}\ S^{-1}$	R
7.40	298	1.480×10^3	1.480×10^{11}	0.997
7.40	310	1.120×10^3	1.120×10^{11}	0.993
7.40	320	1.089×10^3	1.089×10^{11}	0.996

5.3.4 Influence of Silver Colloid on Protein's *pI*

Silver nanoparticles can be rapidly produced by a strong reducing agents, such as borohydrate or sodium citrate. There is a long nucleation period, resulting in particles of varying sizes⁴⁸. For example, the commonly used citrate reduction method⁴⁴, produces a distribution of particles different sizes and shapes. Silver colloid is commonly used for surface enhanced Raman spectroscopy (SERS). However, here our primary goals was to demonstrate, by comparison of CIEF profiles of the a protein, that the silver colloid affect the *pI* of the protein when it incubated for the period of 8 hrs.

The interaction occurs through hydrophobic and electrostatic interactions of silver particles and protein. Our experiments have shown that the protein structure is preserved upon adsorption to the metal surface and there no possibilities for changes after the adsorption took place.

Fig 5-9 shows the CIEF spectrum of Carbonic Anhydrase I incubated with silver colloid. The electropherogram shows the cIEF profile of Carbonic Anhydrase I incubated with Ag colloid solution. Two major properties are expected when protein absorb onto colloidal particles; the proteins may either stablized or destabilized the colloidal dispersion or they may affect the charge distribution of the nanoparticles. This protein contains a positive charge so no interaction was expected when mixed with a Ag colloid. However, the *pI* was shited to left with a short incubation

period. This shows that the positive charge from the Ag colloid, enhance the positive charge on the protein to cause a shift to the left. However, the reasons of the distortion of the protein structure not clear.

The amount of initially added colloid slightly influenced the stability of the protein.

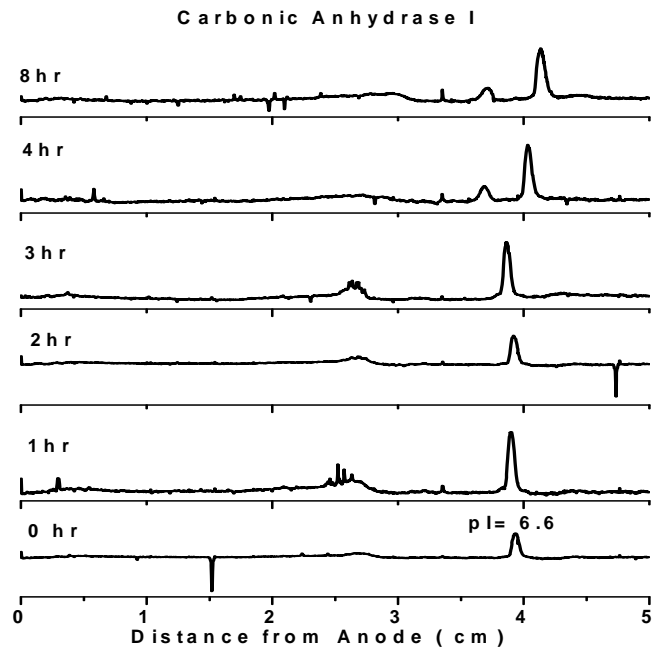


Figure 5-9. The observed *pI* shift of Carbonic Anhydrase I upon incubated with Ag colloid for a short period of time. 0.3mg/mL of carbonic Anhydrase I mixed with 10, 20 and 30 μ L of citrate colloid (5.00×10^{-3} M) and incubated for the period of 0 to 8 hours.



Figure 5-10. The Ag solutions which are prepared by the Lee procedures. The greenish yellow solution is prepared by citrate reduction procedures. This solution shows a strong SERS activity(Fig5-9). However, the second solution (the colloid particles collapsed) shows no SERS activity.

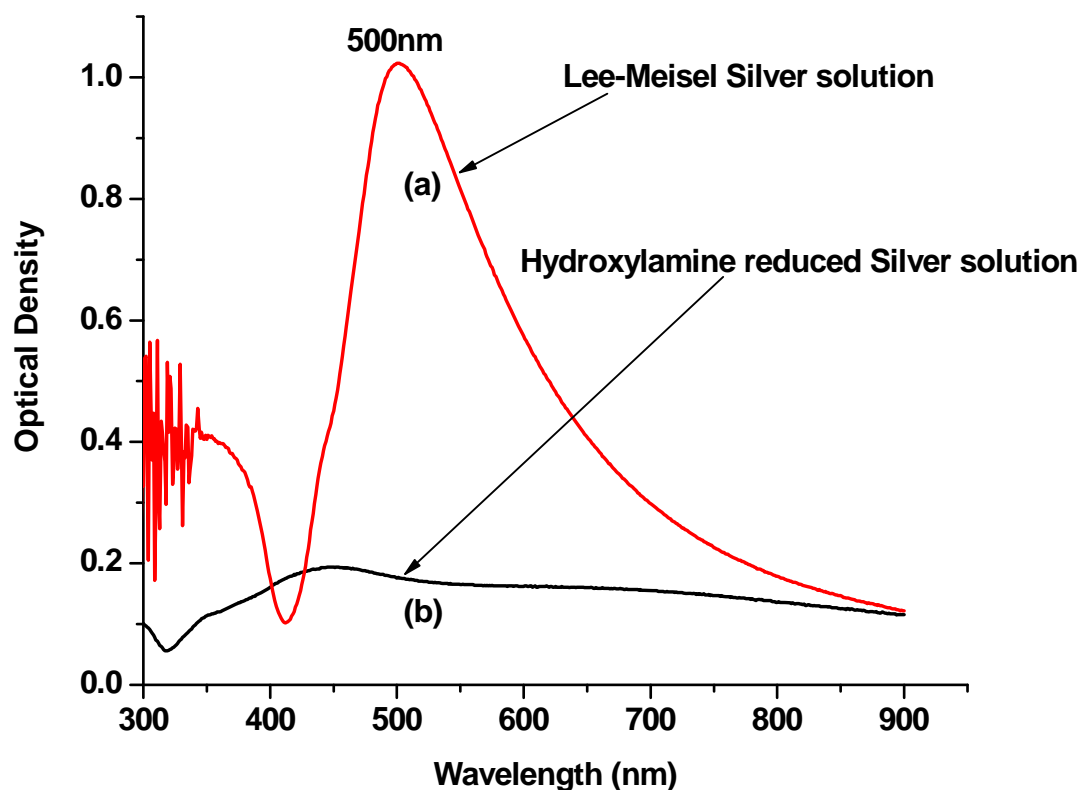


Figure 5-11. The optical absorption of silver colloidal particles.

5.4 Conclusion

CIEF-WCID allows us to monitor the *pI* shift and structural alteration of the protein, when interacted with ligands such as the anticancer agents (oxaliplatin). Several conclusions can be drawn from the results presented here. First, the experimental results demonstrate the significant effects of oxaliplatin on the structural stability of HSA when incubated for a maximum 72 h at physiological pH. Second, on the basis of the data presented here, it may be hypothesized that oxaliplatin may have multiple binding sights on HSA, and, at higher molar ratios, oxaliplatin may cleave S-S the bond, which is responsible

for the stability of the protein. Previous work suggested that cisplatin, the same platinum-based anticancer drug, interacts with multiple sites on HSA when incubated with the protein ⁴². Furthermore, quenching of the intrinsic fluorescence of HSA reinforces the formation of the HSA-oxaliplatin complex. The red shift of the absorption peak of HSA and tryptophan indicates the strong effect caused by oxaliplatin and complex formation of the two analytes.

Finally, CIEF-WCID can help to elucidate the anti-cancer mode of action regarding the affinity toward proteins. However, the technique can be considered as a complementary rather than a competitive technique, because the method exhibits specific ranges of applicability, advantages and disadvantages. For instance, with nano-ESI-MS/MS, the dissociation constant and binding sites may be determined, while with CIEF only adduct formations and *pI* shifts are observed.

CHAPTER 6

CAPILLARY ISOELECTRIC FOCUSING COUPLED WITH DYNAMIC IMAGING DETECTION: A ONE-DIMENSIONAL SEPARATION FOR TWO-DIMENSIONAL PROTEIN CHARACTERIZATION

6.1 INTRODUCTION

Isoelectric point (pI) and molecular weight are two primary attributes for protein characterization and analysis. Classical two-dimensional gel electrophoresis (2D-GE) combines isoelectric focusing (IEF) and sodium dodecyl sulfate (SDS)-polyacrylamide gel electrophoresis (PAGE). Although it offers outstanding high resolution, this method is time-consuming (unusually more than 10 h) and lacks automation. Attempts have been made to overcome the shortcomings of 2D-GE, including combining IEF in capillary-format (CIEF) with electrospray ionization (ESI)-mass spectrometry (MS)¹⁻³ and replacing SDS-PAGE with matrix-assisted laser desorption/ ionization (MALDI)-MS^{4,5}.

***The result presented in this chapter have been published:**

Zhen Liu, **Tibebe Lemma**, and Janusz Pawliszyn,

Capillary Isoelectric Focusing Coupled with Dynamic Imaging Detection: A One-Dimensional Separation for Two-Dimensional Protein Characterization,

Journal of Proteome Research 2006, 5, 1246-1251

The candidate equally contributed to this work.

Clearly, these methods require two one-dimensional separations or two one-dimensional instruments. So far, there is no single one-dimensional separation/instrument that can determine both *pI* and molecular mass. In this study, we present a simple but capable approach to achieve 2D characterization and analysis of proteins employing a single one-dimensional separation.

Proteins were first focused into stationary bands by CIEF in a short column (5 cm long). The focusing process in the whole column was dynamically imaged by a CCD camera through detecting UV absorbance, a technique that is referred to as whole-column imaging detection (WCID)⁶⁻¹³. The *pI* values are calculated from the peak positions through comparing with a calibration curve built with standard *pI* markers. After completion of the focusing, the applied voltage is turned off, and thus, the focused protein bands are allowed to diffuse, resulting in band broadening. The dynamic diffusion process is monitored by the CCD camera. Diffusion coefficient (*D*) is determined according to the Einstein equation¹⁴

$$\sigma^2 = 2Dt \quad (1)$$

where σ^2 is the spatial peak variance due to diffusion, and *t* is the diffusion time. When σ^2 is plotted against the separation time, a linear relationship can be obtained, the slope of which equals *2D*. Furthermore, there is a general formula that allows acceptable estimation of molecular weight from diffusion coefficient,¹⁵⁻¹⁷

$$D = A(T, \eta)M^{-1/3} \quad (2)$$

where A is a function of temperature (T) and the viscosity of the medium (η), and M is the molecular mass. When T and η are kept constant, the linear relationship between $M^{-1/3}$ and D can be used as a calibration curve for determining molecular weight. The principle of the 2D protein characterization approach is illustrated in Figure 6-1. Recently, CIEF-WCID has developed as a reliable pI -based protein characterization and analysis tool^{9, 10}. It offers a baseline resolution of 0.03 pH units, comparable to carrier ampholytes-based in-gel IEF (0.02 pH units). It provides better reproducibility as compared with in-gel IEF, with a SD of 0.01 pH units (corresponds to an RSD of 0.2%) for pI determination and an RSD of 4% for quantitation. As the use of CIEF-WCID for pI determination has been described in previous publications,^{9, 10} this study focuses on the measurement of diffusion coefficient and the determination of molecular weight from diffusion coefficient.

The diffusion coefficient of a molecule is important physical property that can indicate the size, shape, and effective charge of an ionic species. If diffusion is the only source of band broadening in the separation capillary, then it is possible to measure the diffusion coefficient from an electropherogram.

Several techniques are available for measurement of diffusion coefficients. Techniques for measuring diffusion coefficients include free diffusion¹⁸, sedimentation¹⁹, quasi-elastic light scattering (QLS)²⁰ and pulse NMR techniques²¹.

Unlike classical 2D-GE, in which proteins are usually broken into polypeptide chains by using denaturing and reducing reagents, the CIEF-WCID approach can be a useful tool for studying protein oligomeric state. The oligomeric states for β lactoglobulins (A and B), lentil lectin (isoforms I and II), glyceraldehyde-3-phosphate dehydrogenase and urease have been well documented in literature²². When these proteins were considered as monomer, a significantly degraded correlation between $M^{1/3}$ and D for the same set of proteins was observed. Therefore, if the diffusion coefficient measured for a protein is slower than expected from its molecular weight, it indicates a higher-order oligomeric state. For example, the diffusion coefficient for cytochrome C from bovine heart was determined to be 1.05×10^{-7} cm²/s and the molecular weight was calculated to be 22,900, which is 1.86 times higher than its actual molecular weight (12,300). This result implies a dimer form of this protein under the CIEF conditions.

The experiments described above were performed under native conditions, under which the native structure and biological activity of the protein are maintained. However, the isoelectric precipitation problem (proteins tend to precipitate at the pI value under conditions of very low ionic strength) under native conditions is severe for some proteins. This problem can be overcome by adding either protein denaturing reagents or protein solubilizers that are compatible with native structure and maintenance of biological activity. Classical 2D-GE often uses denaturing conditions to solubilize proteins in first dimensional separation (IEF). The possibility of measuring diffusion coefficient

under denaturing conditions was explored. Trypsin inhibitor is a representative protein that aggregated severely under native conditions. It exhibited multiple irreproducible sharp peaks at high concentration (≥ 0.1 mg/mL) but one single reproducible peak at low concentration (< 0.1 mg/mL). After withdrawing the focusing voltage, these peaks did not broaden at all. When denaturing conditions with addition of 6 M urea were used, the protein exhibited a single reproducible peak and its diffusion obeyed the Einstein equation very.

In the proposed approach, the total resolution is determined the CIEF separation (up to 100 peaks), which is much lower than that of a 2D-GE separation (up to 10,000 spots). Therefore, it is only suitable for protein samples of low to moderate complexity. Two applications are demonstrated in the study. One is to quickly identify whether a protein is degraded or not. If a protein is degraded, it will diffuse faster.

In summary, a technique developed a “two birds with one stone” approach for protein characterization/analysis: to measure pI and molecular mass simultaneously by using a single one-dimensional instrument. This approach benefited from the dynamic detection capability of the WCID technique developed in recent years. The accuracy is comparable to that of 2D-GE. Although the resolution is not as high as that of 2D-GE, this approach has several significant advantages. The procedures involved are very simple. The speed is very fast, taking only 10-30 min. The approach can be expected to be a useful 2D characterization/analysis tool for protein samples of low to moderate complexity.

6.2 Experimental

6.2.1 Apparatus

Experiments were conducted on a commercial iCE280 analyzer (Convergent Bioscience, Toronto, Canada)¹⁰. The detection was performed using UV-WCID equipped with 280nm excitation source. The separation column was fluorocarbon internally coated fused-silica capillary (100 μm ID \times 5 cm) to avoid wall absorption and supported by a cartridge (Convergent Bioscience, Toronto, Canada).

6.2.2 CIEF Method

The cartridge was conditioned with a 0.5% (w/v) pvp solution for 20 min before experiments. The protein samples were 0.03-0.3 mg/mL for other proteins, containing 2% Pharmalytes (pH 3-10) and 0.5% pvp. The sample was injected to fill the whole separation column. The applied voltage was 500 V for 2 min for UV-WCID and then increased to 3 kV. After a steady focusing was reached, the focusing voltage was turned off to let the focused protein diffuse. The focusing and diffusion processes were monitored by imaging detection at desired times.

The small molecules were run in the same capillary as CIEF. However, the two tanks (anode and cathode) were filled with a 0.05M phosphate buffer, pH 7.00. Sample ejection was by electromigration for 60sec at 1.5kV. The analytes concentration in the sample ranges from 1 to $4.7 \times 10^{-3}\text{M}$. Electrophoresis was carried out at 3 kV.

6.2.3 Materials and Chemicals

Pharmalytes (pH 3-10, 40% in concentration), polyvinylperrolidone (PVP, average molecular weight about 360,000 and intrinsic viscosity 80-100 K), and other proteins were purchased from Sigma (St Louis, MO, USA). The anolyte and catholyte were 100 mM phosphoric acid and 100 mM sodium hydroxide, respectively. Water was purified with an ultra-pure water system (Barnstead/Thermolyne, Dubuque, IA, USA).

6.3 Results and Discussion

6.3.1 Diffusion coefficient for proteins and peptides

CIEF is a unique CE mode in which the electric current through the capillary exponentially drops along with the separation time, and the residual current is quite low at the end of the focusing, for example, less than 5 μA when an applied voltage of 3 kV and 2% carrier ampholytes were used. Joule heating was further reduced by using low initial focusing voltage (500 V) and increasing it to 3 kV as focusing neared completion (maximum current of a run: 18 μA). It was assumed that if there was a temperature variation, it would be equivalent between runs, as all separations were performed under identical conditions.

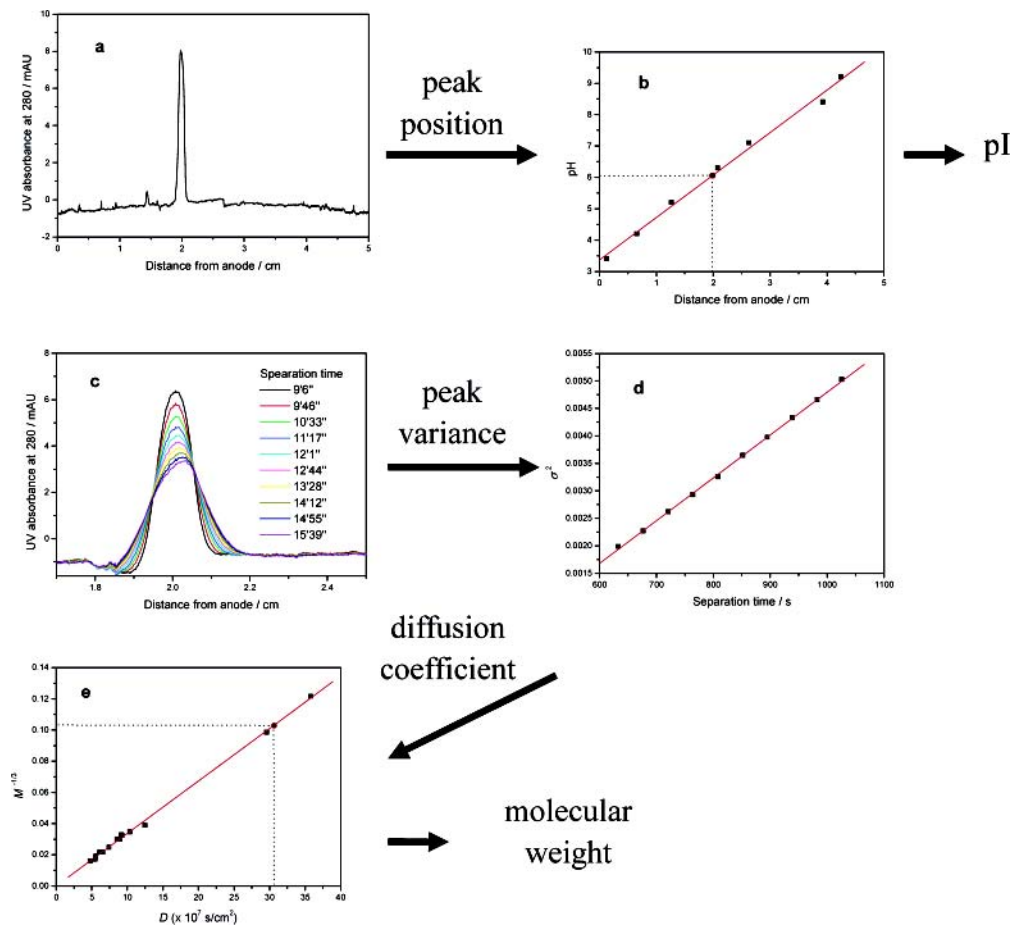


Figure 6-1. The principle of the 2D protein characterization approach using CIEF- WCID. (a) CIEF experiment to measure the peak position in the pH gradient; (b) calibration curve of the pH gradient; (c) dynamically monitoring the diffusion of the protein band; (d) measuring the diffusion coefficient by plotting σ^2 against the separation time (D) slope/2); (e) calibration curve for molecular weight measurement.

For this experiment, sixteen proteins and peptides with molecular weights from 295 to 272 000 were chosen as test proteins (Table 6-1). Diffusion

coefficients of these proteins were measured under identical conditions. The diffusion coefficient measurement is illustrated in Figure 6-2. The diffusion processes of the test proteins and peptides obeyed the Einstein equation very well, giving squared correlation coefficients of >0.99 in most cases. Acceptable reproducibility was obtained; for instance, the RSD was 2.0% for carbonic anhydrase II and 6.7% for myoglobin. Table 6-1 lists the experimental diffusion coefficients, along with available literature data for comparison. We emphasize that the diffusion coefficients in this study were measured at the pI values of the proteins, whereas those in the literature were usually not. As the diffusion coefficients of proteins reported in the literature depend on the surface charge of the protein molecule, the diffusion coefficients measured at isoelectric pH should provide a more reasonable measure for protein diffusivity as compared with those measured at other pH conditions, since the protein molecules have zero net charge at their isoelectric pH. The effect of charge status on the diffusion of bovine serum albumin (BSA) was investigated, as shown in Figure 6-3. The diffusion coefficient of BSA was determined to be $7.44 \times 10^{-7} \text{ cm}^2/\text{s}$ at neutral state, while 11.65×10^{-7} and $12.75 \times 10^{-7} \text{ cm}^2/\text{s}$ when the protein was positively and negatively charged, respectively. These data indicate that electrostatic interactions have a significant effect on diffusion. This effect can be neglected in the present study.

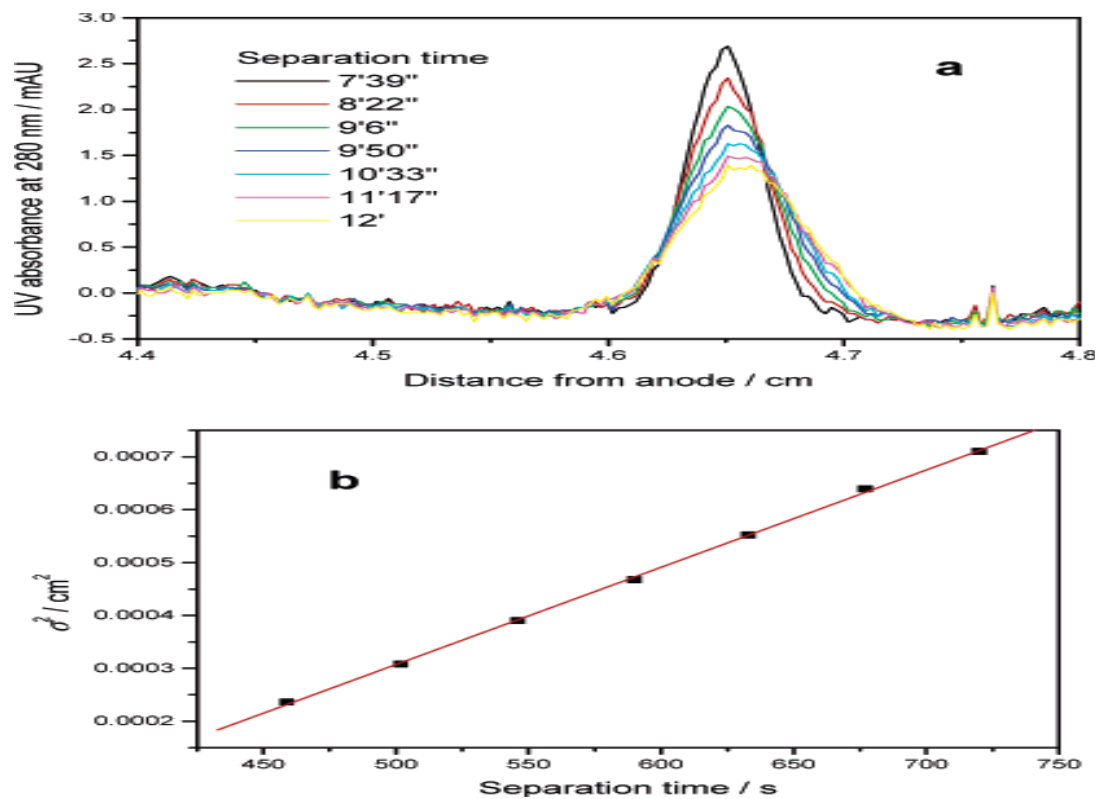


Figure 6-2. Measurement of diffusion coefficient of protein by CIEF-WCID.

(a) The electropherograms at different separation times (the focusing was terminated at 7 min); (b) the plot of σ^2 against separation time. $\sigma^2 = -6.14 \times 10^{-4} (\pm 1.16 \times 10^{-5}) + 1.84 \times 10^{-6} (\pm 1.95 \times 10^{-8})t$, $r^2 = 0.9995$, $SD = 4.49 \times 10^{-6}$, $n = 7$. σ was calculated from the peak width at half peak height ($W_{1/2}$) according to $\sigma = W_{1/2}/2.35$. To simplify the data-processing, the separation time instead of the diffusion time was used to perform the linear fit, which contributes an intercept in the resulting equation but makes no difference on the slope.

Figure 6-3 shows the linear relationship between $M^{1/3}$ and D , which gave excellent linearity ($r^2 = 0.9987$). The validity of this calibration curve was evaluated by the leave-one-out approach (using all but one protein in the data set to establish a calibration curve and then using the remaining one to test the prediction, and repeating this process until all proteins are tested), and the estimated values and errors are also listed in Table 6-1.

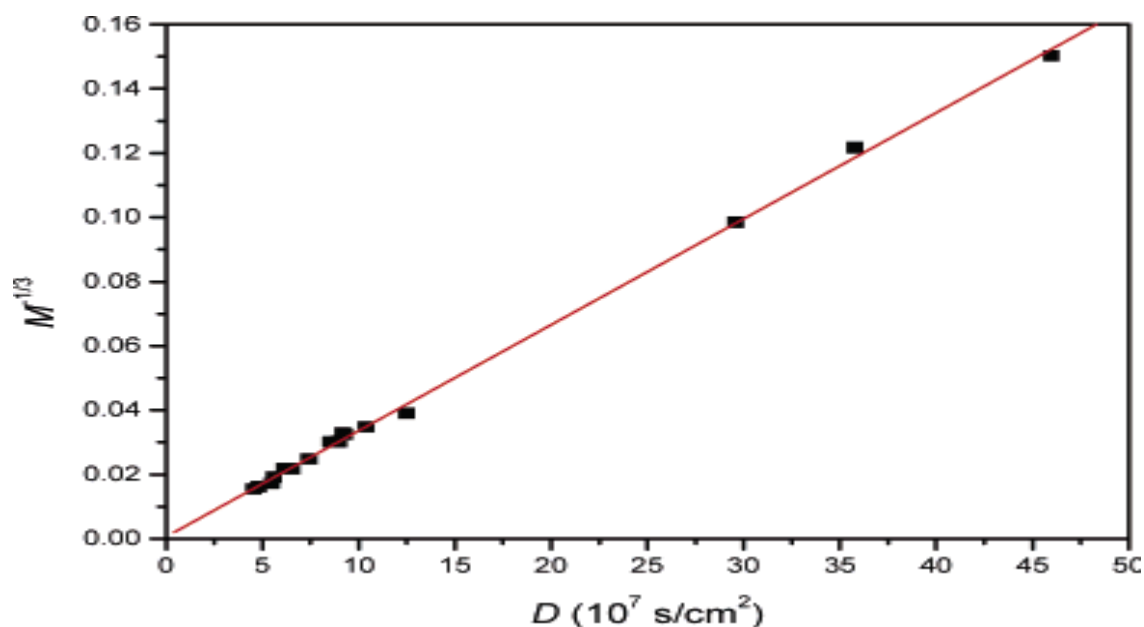


Figure 6-3. Calibration curve for the molecular weight estimation.

$$M^{1/3} = 5.77 \times 10^{-4} (\pm 5.67 \times 10^{-4}) + 3.30 \times 10^4 (\pm 3.17 \times 10^2) D, r^2 = 0.9987,$$

$$SD = 1.53 \times 10^{-3}, \quad n = 16.$$

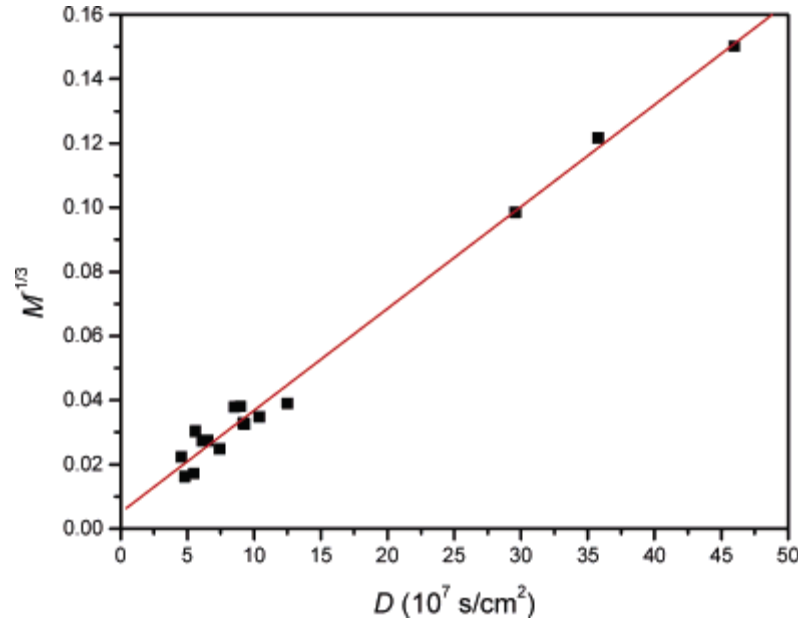


Figure 6-4. The correlation between $M^{-1/3}$ and D when considering all proteins tested as monomers. The use of incorrect oligomeric states led to a degraded correlation (refer to Figure 6-3). $M^{-1/3} = 5.03 \times 10^{-3} (\pm 1.56 \times 10^{-3}) + 3.17 \times 10^{-4} (\pm 8.72 \times 10^{-2})D$, $r^2 = 0.9894$, $SD = 4.21 \times 10^{-3}$, $n = 16$.

The errors were <8.5% for nine proteins, 10-15% for four proteins, and within 20-26% for the remaining three proteins, giving an average error of 9.9%. Such accuracy is comparable to that of 2D-GE (5-20%), for example, an average error of 8.6% and an error of >25% for some proteins in the literature.

Table 6-1. Experimental Diffusion Coefficients, Estimated Molecular Weights, and associated Errors.

Protein/peptide	M	Oligomeric state	D_{exp} ($\times 10^7$ s/cm²)	$D_{lit.}$ ($\times 10^7$ s/cm²)	$M_{exp.}$	Error %
Tyr-Gly-Gly	295	monomer	40.60		270	-8.4
Leucine enkephalin	556	Monomer	35.80	41.00 ²³	600	10.8
Angiotensin II, human	1046	monomer	29.60	25.25 ²⁴	1000	0.6
Myoglobin, isoform 1 (pI 7.2), horse heart	17000	monomer	12.50	11.3 ²⁵	13200	-20.7
Rypsinogen, bovine pancreas	24000	monomer	9.20	9.70 ²⁵	23300	-2.0
Carbonic anhydrase I, human erythrocytes	28200	monomer	9.36	10.66 ²⁵	34400	22.4
Carbonic anhydrase II, bovine erythrocytes	29250	monomer	9.27		33250	14.0
β -lactoglobulin B, bovine milk	36550	dimer	8.99	3.14 ²⁶	36100	-1.1
β -lactoglobulin A, bovine milk	36800	dimer	8.56	7.38 ²⁷	42300	14.7
Albumin, bovin serum	66000	monomer	7.75	5.90 ²⁵	63500	-4.8
Lentil lectin, isoform I (pI=8.2)	98000	dimer	6.56		92400	-7.6
Lentil lectin Isoform II (pI=8.6)	98000	dimer	6.15		114200	13.5
Glyceraldehyde-3-phosphate dehydrogenase	144000	tetramer	5.60	4.97 ²⁵	149800	0.4
β -amylase, sweet potato	200000	monomer	5.50	5.77 ²⁵	153900	-25.7
Rphycoerythrin, red algae	240000	monomer	4.81		234800	-7.0

Urease, jack bean	272000	trimer	4.56	3.46^{25}	276600	-3.9
-------------------	--------	--------	------	-------------	--------	------

It was found that the diffusion coefficient depends on not only the molecular weight but also the oligomeric state of proteins. The oligomeric states for β lactoglobulins, lentil lectins, glyceraldehyde-3-phosphate dehydrogenase, and urease have been well-documented in the literature.^{19, 28} When these proteins were considered as monomers, a significantly degraded correlation between $M^{1/3}$ and D for the same set of proteins was observed, as seen in Figure 6-1. If the diffusion coefficient measured for a protein is slower than expected from its molecular weight, therefore, a higher-order oligomeric state is indicated. For example, the diffusion coefficient for cytochrome *C* from bovine heart was determined to be $1.05 \times 10^{-7} \text{ cm}^2/\text{s}$, and the molecular weight was calculated to be 22 900, which is 1.86 times higher than its actual molecular weight (12 300). This result implies a dimer form of this protein under the CIEF conditions.

The experiments described above were performed under native conditions, where the native structure and biological activity of the protein are maintained. However, the isoelectric precipitation problem (proteins tend to precipitate at the pI value under conditions of very low ionic strength) under native conditions is severe for some proteins. This problem can be overcome by adding denaturing reagents such as urea to improve the solubility of protein. The possibility of measuring diffusion coefficient under denaturing conditions was explored. Trypsin inhibitor is a representative protein that aggregates

severely under native conditions. It exhibited multiple irreproducible sharp peaks at high concentration (>0.1 mg/mL) but one single reproducible sharp peak at low concentration (<0.1 mg/mL). After withdrawing the focusing voltage, these peaks did not broaden at all. When denaturing conditions with the presence of 6 M urea were used, the protein exhibited a single reproducible peak and its diffusion obeyed the Einstein equation . In the proposed approach, the total resolution is determined by the CIEF separation (up to 100 peaks), which is much lower than that of 2D-GE (up to 10 000 spots). Therefore, it is only suitable for protein samples of low to moderate complexity. Two representative applications are demonstrated in the study. The first one is to quickly identify whether a protein is degraded or not. If a protein is degraded, it will diffuse faster. The normal protein, which was stored at 2-8 °C, exhibited a diffusion coefficient of 4.81×10^{-7} cm²/s.

6.3.2 Diffusion Coefficient of Small Molecules

To evaluate the feasibility of CIEF as a means of measuring diffusion coefficients of proteins, the technique was initially tested on small molecules that do not tend to display adsorptive behavior in a separation capillary. The samples selected for this initial study were dansyl-alanine, epinephrine, fluorescamine, phenol and L-tryptophan (Table 6-2).

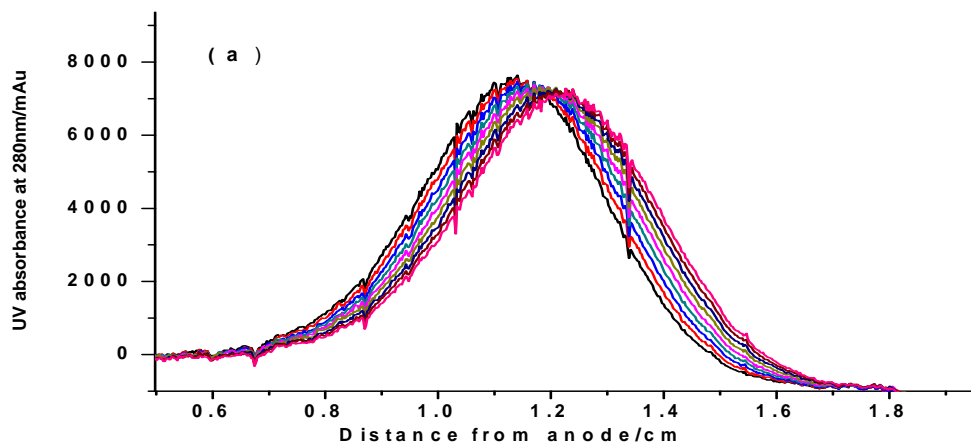
In this technique, contrary to the CIEF method, the samples were injected by electromigration at 1.5 kV for 5 sec and permitted to migrate

approximately halfway to the capillary. The voltage then turned off, and the solute is allowed to diffuse for several minutes.

The results of the above-described experiments are given in Table 6-2. These are all measured in 0.05 M phosphate buffer, pH=7.4. The experimental D values of the two neurotransmitter (epinephrine and dopamine) have been measured by flow injection analysis (FIA) and is not in good agreement with the present results (Fig 6-5). The discrepancy is probably caused by the total charge differences on the analytes or the mobility difference between the sample and the buffer²⁸. However, the two amino acids (L-tryptophan and dansyl alanine) showed only a small differences compared with the published values²⁹. Note that most of the tabulated D values are normally obtained in water, whereas the results tabulated in Table 6-2 were measured in phosphate buffer and should possess different charge density, as was found to be the case.

Table 6-2. Diffusion coefficient of test compounds measured by capillary zone electrophoresis (CZE).

Samples	Concentration M	D_m ($10^{-6} \text{ cm}^2/\text{s}$)	Published values ($10^{-6} \text{ cm}^2/\text{s}$)
Dansyl-Alanine	4.7×10^{-3}	5.948	5.35^{28}
Dopamine	2.64×10^{-3}	2.36×10^{-5}	6.05^{23}
Epinephrine	1.58×10^{-3}	9.547	5.1^{23}
Fluorescamine	1.41×10^{-3}	6.543	NA
Phenol	5.0×10^{-3}	1.724	8.4^{29}
L-Tryptophan	1.04×10^{-3}	7.748	9.33^{29}



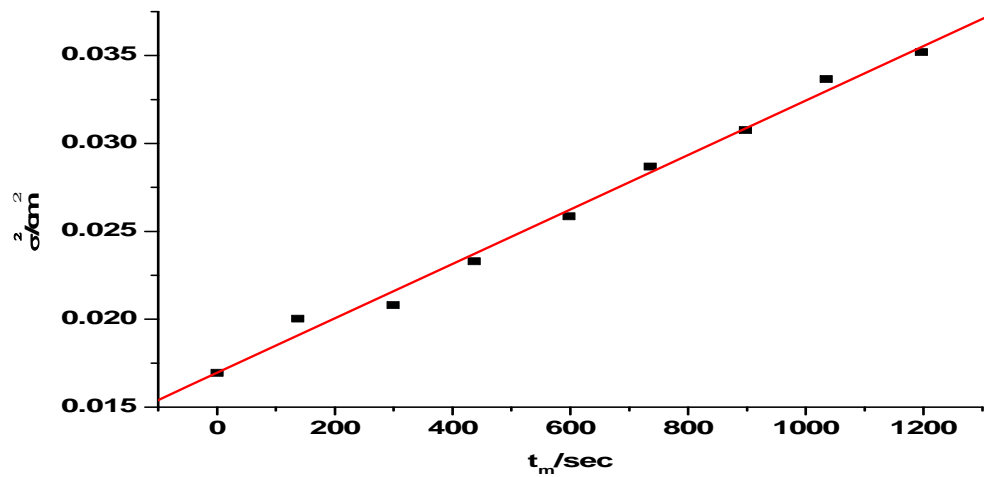


Figure 6-5. Measurement of diffusion coefficient using capillary zone electrophoresis. (a) The electropherograms at different separation times; (b) plot of peak variance (σ^2) against separation time. Separation parameter; 50 mM, phosphate buffer, pH= 8.04 and samples injected from anode ; 1.5 kV applied voltage.

6.4 Conclusions

The method developed is simple but effective approach for protein characterization, measuring *pI* and molecular mass using a single instrument. This approach benefited from the dynamic detection capability of the WCID technique. While yielding accuracy comparable to that of 2D-GE, this approach has several significant advantages, including speed (10-30 min per run) and ease of operation and automation. The approach can be expected to be a useful 2D characterization/analysis tool for protein samples of low to moderate complexity. When combined with prefractionation techniques, it can be applied to more complicated protein samples.

CHAPTER 7

SUMMARY AND RECOMMENDATION FOR FUTURE STUDIES

7.1 Summary

A new high performance Raman technique has been developed which employs low loss liquid core optical fibers of a short Teflon tube and a small probe volume Raman scattering based detector which is compared to conventional sample methods. In the new technique, the focused beam from an argon ion laser passes through 50 mm or more of a liquid or solution contained in a hollow fused quartz optical fiber having a core diameter of $\sim 120 \mu\text{m}$. The refractive index of the liquid or solution must be greater than that of the Teflon tube at both the wavelengths of the Raman and exciting radiations. The intensified radiation emerging from the optical fiber is simply collected near the entrance optics of the Raman spectrometer. The major advantages of the method are that very high Raman intensities are obtained and that only very small amounts of sample are required. The new fiber optics laser-Raman method should be of use in routine analytical procedures involving a wide range of solutions, for example, in the analysis of protein-ligand interactions, of solutions of biologically interesting materials, solutions of gases and solids, and involving traces pollutants.

The early chapters of this thesis were focused on the development and characterization of the instrumentation. In chapter 2, the performance and the various stages in the design and specifications of LCW-RS were discussed. The

performance of the instrument was evaluated using seven acetaminophen based Tylenol tablets with minor chemical composition differences. These results are important for future work of LCW-RS when it will be coupled to CIEF and Solid phase microextraction (SPME) to increase the limit of detection and to analyze wide ranges of molecules.

In chapter 3 the successful implementation of the liquid-core waveguide based Raman spectrometry using a short Teflon tube was demonstrated. Using this approach and a 6-nL probe volume, we have measured the Raman signal from the physiological concentration of HSA, oxaliplatin , HSA+oxaliplatin as test compounds. By demonstrating the feasibility of this technique, we have taken the first step in realizing the unparalleled collection efficiency of such scattering events occurring in the core of a short Teflon tube.

In chapter 4, in an attempt to understand how platinum based metallocomplexes bind to proteins, two different techniques have been applied to characterize the complex formation. Using oxaliplatin and cisplatin as reference drugs, the application of CIEF-WCID to reliably assess drug-Hb interaction was validated. On the basis of the CIEF profiles of Hb-cisplatin and Hb-oxaliplatin obtained using this method, differences in the binding patterns were observed for the two drugs. From the results presented in this chapter, oxaliplatin shows a greater affinity toward Hb at the physiological concentration of the proteins, while cisplatin binds Hb less strongly. However, the experiments also show for longer incubation periods and higher concentrations of the drugs resulted in the formation of adducts and destabilization of the

protein structures. These experiment confirm the validity of CIEF-WCID as a valid technique to characterize protein-drug interactions. In future, a variety of chemotherapeutic drugs and their interactions with different proteins under physiological conditions can be characterized using this simple technique when coupled with laser induced fluorescence (LIF). This chapter generalizes the validity of the CIEF-WCID technique for the study of protein-drug interactions and provides useful information and insight into the interaction of anticancer drugs with HSA for further toxicity of these chemotherapeutic drugs and improving their clinical performance.

In Chapter 5 a method was described to examine the interaction between the platinum-based anticancer drug, oxaliplatin, with human serum albumin (HSA) in aqueous solution at physiological pH with drug concentrations of 10 to 100 μ M and a constant concentration of HSA (5.0×10^{-5} M). The reaction mixtures were incubated for 0, 0.5, 1, 12, 24, 48 and 72 h at 37⁰C in a water bath. The CIEF results indicate that with increasing drug concentration, the complex formation of protein adducts increased compared to low drug concentrations, and major structural changes were observed as the incubation time progressed. The altered CIEF profile demonstrated the possible conformational changes due to the binding of the drug. Results also showed a significant protein *pI* shift for higher HSA-oxaliplatin incubation ratios. Furthermore, the interaction of HSA with oxaliplatin was also confirmed by ultraviolet-visible (UV/Vis) absorbance and fluorescence quenching spectroscopy. Spectroscopic evidence shows that

oxaliplatin caused the fluorescence quenching of HSA by formation of HSA-oxaliplatin complex. Using the Stern-Volmer equation, the quenching constants were calculated in the linear range. The quenching rate constants K_q at three different temperatures indicated that the quenching was initiated by static quenching.

Finally, a simple but effective approach was developed to characterize proteins including measuring pI and molecular mass. The approach combines CIEF, which separates proteins according to their pI , with dynamic imaging detection, which permits monitoring of protein diffusion in real time and thereby allows estimation of molecular weight from its diffusion coefficient. While yielding accuracy comparable to that of 2D-GE, this technique has several significant advantages, including speed (10-30 min per run) and ease of operation and automation. To test this approach, 16 proteins and peptides with molecular weights from 295 to 272 000 were chosen as test proteins. The diffusion coefficients and pI values of these proteins were determined under identical conditions. This simple technique can be applied to more complicated proteins if combined with prefractionation techniques.

7.2 Future Studies

The work present here lays the ground work for the new path of investigating ligand-protein interactions using two different techniques. As already stated in chapter 1, the Raman technique is a fast analysis technique that requires only small sample volumes with almost no interference from water. Raman spectroscopy is a powerful tool for investigating chemical composition and molecular structure. However, the major limitation of conventional Raman spectroscopy is its low sensitivity due to the inherently low efficient scattering process. One technique, which overcomes these difficulties, is surface enhanced Raman spectroscopy (SERS). The unique ability to obtain molecular recognition of an analyte at very low concentrations in situ in aqueous environments using SERS and surface enhanced resonance Raman scattering (SERRS) detection makes these spectroscopies of considerable interest.

Further work on the coupling of LCW-CIEF and LCW-SPME is essential for studies of proteins and protein-ligand interactions. Furthermore, the detection of single molecules can be achieved by using SERS active nanoparticles, coupled with CIEF or Laser induced fluorescence (LIF). A logical progression would be to conduct experiments under physiological concentrations for protein-drug interactions in order to study the action of the drug at the single molecule level.

Finally, the mechanism of transport of oxaliplatin or cisplatin into erythrocytes to form Hb adducts is, however, not known. Thus, further studies

are necessary to investigate how oxaliplatin or cisplatin transported into erythrocytes to form Hb adducts. To accomplish this task, nanotubes have been suggested as a promising technique to transport the drug to the target site. Using this technique, nanotubes can be used as a drug carrier and the adducts formation between the drug-protein and drug-protein-nanotubes can be investigated by Raman spectroscopy. Furthermore, SERS active metal particles can be used to enhance the Raman signal of single adducts molecule formed between the drug and the protein of interest.

References

Chapter 1. References

- (1) Kolin, A. *J. Chem. Phys* **1954**, *22*, 2099.
- (2) P.G., Righetti. *Isoelectric Focusing: Theory, Methodology and Application*; Elsevier Biomedical press: Amsterdam, 1983.
- (3) Svensson, H. *Acta Chemica Scandinavica* **1961**, *15*, 325-341.
- (4) Svensson, H. *Arch. Biochem. Biophys* **1962**, *1*, 132-138.
- (5) Svensson, H. *Acta Chem. Scand* **1962**, *16*, 456-466.
- (6) Reiner, W. *Electrophoresis in Practice*; WILEY-VCH Verlag GmbH, 2001.
- (7) Righetti, P. G.; Chiari, A. *Conventional isoelectric focusing and immobilized pH gradients: an overview, in Capillary electrophoresis technology*; New York : Dekker, c1993.: New York, 1993.
- (8) Vesterberg, O. *Acta Chem. Scand* **1969**, *23*, 2653-2666.
- (9) Mosher, R. A.; Saville, D. A.; Thormann, W. *The dynamics of electrophoresis*; VCH Verlagsgesellschaft mbH, D-6940 Weinheim (Federal Republic of Germany), 1992.
- (10) Vesterberg, O.; Svensson, H. *Acta Chem Scand* **1966**, *20*, 820-834.
- (11) Hjerten, S.; Liao, J. L.; Yao, K. Q. *J Chromatogr* **1987**, *387*, 127-138.
- (12) Hjerten, S.; Zhu, M. D. *J. Chromatogr* **1985**, *346*, 265-270.
- (13) Hjerten, S.; Zhu, M. D. *J. Chromatogr.* **1985**, *346*, 265-270.
- (14) Hjerten, S.; Elenbring, K.; Kilar, F.; Liao, J. L.; Chen, A. J.; Siebert, C. J.; Zhu, M. D. *J Chromatogr* **1987**, *403*, 47-61.
- (15) Wehy, T.; Rodrigues-Diaz, R.; Zhu, M. D. *Capillary Electrophoresis of Proteins*; Marcel Dekker, Inc, 1999.
- (16) Horvath, J.; Dolnik, V. *Electrophoresis* **2001**, *22*, 644-655.
- (17) Gao, Q.; Yeung, E. S. *Anal. Chem* **1998**, *70*, 1382-1388.
- (18) Cifuentes, A.; Canalejas, P.; Ortega, A.; Diez-Masa, J. C. *J. Chromatogr* **1998**, *823*, 561-571.
- (19) Chiari, M.; Micheletti, C.; Nesi, M.; Fazio, M.; Righetti, P. G. *Electrophoresis* **1994**, *15*, 177-186.
- (20) Baker, D. R. *Capillary electrophoresis*; John Wiley & Sons, Inc, 1995.
- (21) Mosher, R. A.; Saville, W, D. A.; Thormann, W. *The Dynamics of Electrophoresis*; VCH: Germany, 1992.
- (22) Wehy, T.; Rodrigues-Diaz, R.; Zhu, M. *Capillary Electrophoresis of Proteins*; Marcel Dekker, Inc, 1999.
- (23) Hjerten, S.; Elenbring, K.; Kilar, F.; Liao, J. L.; Chen, A. J.; Siebert, C. J.; Zhu, M. D. *J Chromatogr* **1987**, *403*, 47-61.
- (24) Patrick, C. *Capillary Electrophoresis. Theory and Practice*, Second Edition ed., 1998.
- (25) Thormann, W.; Caslavská, J.; Molteni, S.; Chmelik, J. *J. Chromatogr.* **1992**, *589*, 321-327.
- (26) Wu, J.; Pawliszyn, J. *Anal. Chem* **1992**, *64*, 224-227.
- (27) Wu, J.; Pawliszyn, J. *Anal. Chem* **1994**, *66*, 867-873.

- (28) Wu, J.; Watson, A. H.; Torres, A. R. *American Biotechnology Laboratory* **1999**, *17*, 24, 26.
- (29) Liu, Z.; Pawliszyn, J. *Anal. Chem* **2003**, *75*, 4887-4894.
- (30) Wu, J.; Tragas, C.; Watson, A.; Pawliszyn, J. *Anal. Chim. Acta* **1999**, *383*, 67-78.
- (31) Spanik, I.; Lim, P.; Vigh, G. *J. Chromatogr* **2002**, *960*, 241-246.
- (32) Mao, Q.; Pawliszyn, J. *J. Biochem. Biophys. Methods* **1999**, *39*, 93-110.
- (33) Wu, J.; Li, S.-C.; Watson, A. *J. Chromatogr* **1998**, *817*, 163-171.
- (34) Cunliffe, J. M.; Liu, Z.; Pawliszyn, J.; Kennedy, R. T. *Electrophoresis* **2004**, *25*, 2319-2325.
- (35) Liu, Z.; Pawliszyn, J. *Electrophoresis* **2005**, *26*, 556-562.
- (36) Goodridge, L.; Goodridge, C.; Wu, J.; Griffiths, M.; Pawliszyn, J. *Anal. Chem* **2004**, *76*, 48-52.
- (37) Liu, Z.; Pawliszyn, J. *Anal. Biochem* **2005**, *336*, 94-101.
- (38) Liu, Z.; Wu, S. S.; Pawliszyn, J. *J. Chromatogr* **2007**, *1140*, 213-218.
- (39) Liu, Z.; Pawliszyn, J. *J. Proteome Res* **2004**, *3*, 567-571.
- (40) Liu, Z.; Lemma, T.; Pawliszyn, J. *J. Proteome Res* **2006**, *5*, 1246-1251.
- (41) Kilar, F. *CRC Handbook of Capillary Electrophoresis: a practical Approach*; CRC Press, Boca Raton, FL., 1994.
- (42) Ahuja, S. *Selectivity and Detectability Optimizations in HPLC*; Wiley: New York, 1989.
- (43) A.Guzman, N. *Capillary Electrophoresis Technology*; Mercel Dekker, Inc: New York, 1993.
- (44) Yeung, E. S.; Sepaniak, M. J. *Anal. Chem* **1980**, *52*, 1465A.
- (45) Coblenz, W. W. *Investigations of Infrared Spectra*; Carnegie: Washington, 1905; reprinted 1962.
- (46) Raman, C. V.; Krishnan, K. S. *Nature* **1928**, *121*, 501-502.
- (47) *Molecular Vibrations*; McGraw-Hill, New York, 1955.
- (48) *Molecular Vibrations*; Nauka, Moscow, 1972.
- (49) Cotton, F. A. *Chemical Applications of Group Theory*; Wiley-Interscience, New York, 1971.
- (50) Grasselli, J. G.; Bulkin, B. J. *Analytical Raman Spectroscopy*; John Wiley & Sons, INC., 1991.
- (51) Califano, S. *vibrational States*; John Wiley & Sons, 1976.
- (52) Bernhard, S. *Infrared and Raman Spectroscopy*, 1995.
- (53) McHale, J. L. *Molecular Spectroscopy*; Prentice-Hall, Inc: United States, 1999.
- (54) Hollas, J. M. *Modern Spectroscopy*, Fourth ed.; John Wiley & Sons Ltd, UK, 2004.
- (55) Chalmers, J. M.; Griffiths, P. R. *Handbook of Vibrational Spectroscopy, Vol. 1*; Wiley & Sons, Chichester Baffins Lane: UK, 2002.
- (56) Ewen, S.; Geoffrey, D. *Modern Raman Spectroscopy*; John Wiley & Sons Ltd., 2005.
- (57) Long, D. *The Raman Effect: A Unified Treatment of the Theory of Raman Scattering by Molecules*; John Wiley & Sons, 1977.

- (58) Ferraro, J., R.; Nakamoto, K. *Introductory Raman Spectroscopy*; Academic Press, San Diego, 1994.

Chapter 2. References

- (1) Pawluczyk, R.; Yang, W.; Hockley, B. S.; (Cme Telemetry Inc., Can.). Application: WO9723159,1997.
- (2) Pawluczyk, R.; Sampara, K.; Hu, S.-J.; Li, M.; (CME Telemetry Inc., Can.). Application: WO/2003/055381,2003, pp 56
- (3) Kryszczyński, T.; Pawluczyk, O.; Pawluczyk, R.; (P&P Optica Inc., Can.). Application: US, 2005.
- (4) Pawluczyk, R.; Sampara, K.; Morand, K.; Hu, S.-j.; Lynch, M.; Li, M.; (Nir Diagnostics Inc., Can.). Application: CA, 2005, pp 57 pp.
- (5) <http://www.ppo.ca/>.
- (6) Pawluczyk, O.; Pawluczyk, R. *Proc. SPIE* **2007**, 6443, 64430G-64431.
- (7) Barden, S. C. *Proc.SPIE* **1998**, 3355, 866-876.
- (8) Becke, A., D. *Physical Review A* **1988**, 3098-3100.
- (9) Callahan, M. R.; Rose, J. B.; Byrne, R. H. *Talanta* **2002**, 58, 891-898.
- (10) Frisch, M. J. T., G. W.; Schlegel, H. B.; Scuseria, G. E.; Robb, M. A.; Cheeseman, J. R.; Montgomery, Jr., J. A.; Vreven, T.; Kudin, K. N.; Burant, J. C.; Millam, J. M.; Iyengar, S. S.; Tomasi, J.; Barone, V.; Mennucci, B.; Cossi, M.; Scalmani, G.; Rega, N.; Petersson, G. A.; Nakatsuji, H.; Hada, M.; Ehara, M.; Toyota, K.; Fukuda, R.; Hasegawa, J.; Ishida, M.; Nakajima, T.; Honda, Y.; Kitao, O.; Nakai, H.; Klene, M.; Li, X.; Knox, J. E.; Hratchian, H. P.; Cross, J. B.; Bakken, V.; Adamo, C.; Jaramillo, J.; Gomperts, R.; Stratmann, R. E.; Yazyev, O.; Austin, A. J.; Cammi, R.; Pomelli, C.; Ochterski, J. W.; Ayala, P. Y.; Morokuma, K.; Voth, G. A.; Salvador, P.; Dannenberg, J. J.; Zakrzewski, V. G.; Dapprich, S.; Daniels, A. D.; Strain, M. C.; Farkas, O.; Malick, D. K.; Rabuck, A. D.; Raghavachari, K.; Foresman, J. B.; Ortiz, J. V.; Cui, Q.; Baboul, A. G.; Clifford, S.; Cioslowski, J.; Stefanov, B. B.; Liu, G.; Liashenko, A.; Piskorz, P.; Komaromi, I.; Martin, R. L.; Fox, D. J.; Keith, T.; Al-Laham, M. A.; Peng, C. Y.; Nanayakkara, A.; Challacombe, M.; Gill, P. M. W.; Johnson, B.; Chen, W.; Wong, M. W.; Gonzalez, C.; and Pople, J. A.; . Gaussian, Inc., Wallingford CT, 2004.
- (11) Jeanette, D., Hanna, Purdue University, 1996.

Chapter 3. References

- (1) Colladon, D. *Comptes Rendes* **1842**, 15, 800-802.
- (2) Hecht, J. *City of Light*; Oxford University Press, New York, 1998.
- (3) Allan, W. B. *Fibre Optics Theory and Practice*; Plenum, London, 1973.
- (4) Napoli, D. *Sci. Am* **1889**, 61, 376-377.

- (5) Gambling, W. A.; Payne, D. N.; Matsumura, H. *Opt. Commun* **1972**, *6*, 317-322.
- (6) Buck, W. H.; Resnick, P. R. In *183rd meeting of the electrochemical society*, ; DuPont Product Bulletin H52454: Honolulu, Hawaii, 1993.
- (7) Lowry, J. H.; Mendlowitz, J. S.; Subramanian, N. S. *Opt. Eng* **1992**, *31*, 1982.
- (8) <http://www.dupont.com/teflon/af/performance.html>.
- (9) Yao, W.; Byrne, R. H. *Talanta* **1999**, *48*, 277-282.
- (10) Dasgupta, P. K.; Zhang, G.; Li, J.; Boring, C. B.; Jambunathan, S.; Al-Horr, R. *Anal. Chem* **1999**, *71*, 1400-1407.
- (11) Byrne, R. H.; Yao, W.; Kaltenbacher, E.; Waterbury, R. D. *Talanta* **2000**, *50*, 1307-1312.
- (12) Gooijer, C.; Hoornweg, G. P.; de Beer, T.; Bader, A.; van Iperen, D. J.; Brinkman, U. A. T. *J. Chromatogr* **1998**, *824*, 1-5.
- (13) Dasgupta, P. K.; Zhang, G.; Poruthoor, S. K.; Caldwell, S.; Dong, S.; Liu, S.-Y. *Anal. Chem* **1998**, *70*, 4661-4669.
- (14) Altkorn, R.; Koev, I.; Gottlieb, A. *Appl. Spectrosc* **1997**, *51*, 1554-1558.
- (15) Altkorn, R.; Koev, I.; Pelletier, M. J. *Appl. Spectrosc* **1999**, *53*, 1169-1176.
- (16) Holtz, M.; Dasgupta, P. K.; Zhang, G. *Anal. Chem* **1999**, *71*, 2934-2938.
- (17) Okada, T. *Electrophoresis* **2007**, *28*, 3414-3419.
- (18) Walrafen, G. E. *Appl. Spectrosc* **1975**, *29*, 179-185.
- (19) Ross, H. B.; McClair, W. M. *Appl. Spectrosc* **1981**, *35*.
- (20) Walrafen, G. E. *Phys. Bl* **1974**, *12*, 540.
- (21) Schwab, S. D.; McCreery, R. L. *Appl. Spectrosc* **1987**, *41*, 126.
- (22) Benoit, V.; Yapper, M. C. *Anal. Chem* **1996**, *68*, 2255 - 2258.
- (23) Synytsya, A.; Alexa, P.; de Boer, J.; Loewe, M.; Moosburger, M.; Wurkner, M.; Volka, K. *J. Raman Spectrosc* **2007**, *38*, 1646-1655.
- (24) Dunk Rachel, M.; Peltzer Edward, T.; Walz Peter, M.; Brewer Peter, G. *Environmental science & technology* **2005**, *39*, 9630-9636.
- (25) Siddiqui, M. S. U.; Stanley Robert, J. *Anal Biochem* **2005**, *337*, 121-129.
- (26) Wada, A.; Harada, M.; Okada, T. *Anal Chem* **2006**, *78*, 4709-4712.
- (27) Singh, K.; Liu, C.; Capjack, C.; Rozmus, W.; Backhouse, C. J. *IEE Proc Nanobiotechnol* **2004**, *151*, 10-16.
- (28) Lemma, T.; Mandal, R.; Li, X.-F.; Pawliszyn, J. *J. Sep. Sci* **2008**, *31*, 1803-1809.
- (29) Schweitzer-Stenner, R. *Vib Spectrosc* **2006**, *42*, 98.
- (30) Wiberg, K. B.; Shrake, A. *Spectrochim. Acta, Part A* **1973**, *29*, 583-594.
- (31) <http://ppo.ca/>.
- (32) <http://www.sigmaldrich.com/spectra/rair/RAIR012227.PDF>.
- (33) Lin-Vien, D.; Colthup, N. B.; Fateley, W. G.; Grassetti, J. G. *The Handbook of Infrared and Raman Characteristics Frequencies of Organic Molecules*; ACADEMIC PRESS, INC. Harcourt Brace Jovanovich, Publisher, 1991.
- (34) Liu, Z.; Pawliszyn, J. *Anal Chem* **2003**, *75*, 4887-4894.

- (35) Ye, M.; Hu, S.; Quigley, W. W. C.; Dovichi, N. J. *Journal of Chromatography, A* **2004**, *1022*, 201-206.

Chapter 4. References

- (1) Walrafen, G. E.; Stone, J. *Appl. Spectrosc* **1972**, *26*, 585-589.
- (2) Walrafen, G. E. *Appl. Spectrosc* **1975**, *29*, 179-185.
- (3) <http://www.dupont.com/teflon/af/performance.html>.
- (4) Yao, W.; Byrne, R. H. *Talanta* **1999**, *48*, 277-282.
- (5) Dasgupta, P. K.; Zhang, G.; Li, J.; Boring, C. B.; Jambunathan, S.; Al-Horr, R. *Anal. Chem* **1999**, *71*, 1400-1407.
- (6) Byrne, R. H.; Yao, W.; Kaltenbacher, E.; Waterbury, R. D. *Talanta* **2000**, *50*, 1307-1312.
- (7) Gooijer, C.; Hoornweg, G. P.; de Beer, T.; Bader, A.; van Iperen, D. J.; Brinkman, U. A. T. *J. Chromatogr* **1998**, *824*, 1-5.
- (8) Dasgupta, P. K.; Zhang, G.; Poruthoor, S. K.; Caldwell, S.; Dong, S.; Liu, S.-Y. *Anal. Chem* **1998**, *70*, 4661-4669.
- (9) Altkorn, R.; Koev, I.; Gottlieb, A. *Appl. Spectrosc* **1997**, *51*, 1554-1558.
- (10) Altkorn, R.; Koev, I.; Pelletier, M. J. *Appl. Spectrosc* **1999**, *53*, 1169-1176.
- (11) Holtz, M.; Dasgupta, P. K.; Zhang, G. *Anal. Chem* **1999**, *71*, 2934-2938.
- (12) Okada, T. *Electrophoresis* **2007**, *28*, 3414-3419.
- (13) Okada, T. *Electrophoresis* **2007**, *28*, 3414-3419.
- (14) Preston, T. C.; Jones, N. D.; Stille, S.; Mittler, S. *Applied Physics Letters* **2006**, *89*, 253509/253501-253509/253503.
- (15) Kostal, V.; Zeisbergerova, M.; Hrotekova, Z.; Slais, K.; Kahle, V. *Electrophoresis* **2006**, *27*, 4658-4665.
- (16) Dijkstra, R. J.; Bader, A. N.; Hoornweg, G. P.; Brinkman, U. A. T.; Gooijer, C. *Anal. Chem* **1999**, *71*, 4575-4579.
- (17) Wada, S.; Kawatsu, T.; Hashizume, Y.; Yabutani, T.; Motonaka, J. *International Journal of Modern Physics B: Condensed Matter Physics, Statistical Physics, Applied Physics* **2006**, *20*, 4046-4050.
- (18) Wang, S.-L.; Fan, X.-F.; Xu, Z.-R.; Fang, Z.-L. *Electrophoresis* **2005**, *26*, 3602-3608.
- (19) Sun, M.; Du, W.-B.; Fang, Q. *Talanta* **2006**, *70*, 392-396.
- (20) Wang, Z. A.; Cai, W.-J.; Wang, Y.; Upchurch, B. L. *Marine Chemistry* **2003**, *84*, 73-84.
- (21) Robles, T.; Paige, D.; Anastasio, C. *Review of Scientific Instruments* **2006**, *77*, 073103/073101-073103/073104.
- (22) Wada, A.; Harada, M.; Okada, T. *Anal. Chem* **2006**, *78*, 4709-4712.
- (23) Wilson, R. E.; Hu, Y.-J.; Nitsche, H. *Radiochim. Acta* **2005**, *93*, 203-206.
- (24) Kostal, V.; Zeisbergerova, M.; Slais, K.; Kahle, V. *J. Chromatogr., A* **2005**, *1081*, 36-41.
- (25) Manor, R.; Datta, A.; Ahmad, I.; Holtz, M.; Gangopadhyay, S.; Dallas, T. *IEEE Sensors Journal* **2003**, *3*, 687-692.

- (26) Datta, A.; Eom, I.-Y.; Dhar, A.; Kuban, P.; Manor, R.; Ahmad, I.; Gangopadhyay, S.; Dallas, T.; Holtz, M.; Temkin, H.; Dasgupta, P. K. *IEEE Sens. J* **2003**, *3*, 788-795.
- (27) Tao, S.; Gong, S.; Xu, L.; Fanguy, J. C. *Analyst* **2004**, *129*, 342-346.
- (28) Roerdink, A. R.; Aldstadt, J. H. *Analytica Chimica Acta* **2005**, *539*, 181-187.
- (29) Liu, Z.; Pawliszyn, J. *Analytical Biochemistry* **2005**, *336*, 94-101.
- (30) Dijkstra, R. J.; Boelens, H. F. M.; Westerhuis, J. A.; Ariese, F.; Brinkman, U. A. T.; Gooijer, C. *Anal. Chim. Acta* **2004**, *519*, 129-136.
- (31) Curcio, M.; Stalhandske, P.; Lindberg, P.; Roeraade, J. *Electrophoresis* **2002**, *23*, 1467-1472.
- (32) Inya-Agha, O.; Stewart, S.; Veriotti, T.; Bruening, M. L.; Morris, M. D. *Applied Spectroscopy* **2002**, *56*, 574-578.
- (33) Hanning, A.; Westberg, J.; Roeraade, J. *Electrophoresis* **2000**, *21*, 3290-3304.
- (34) Li, Q.; Morris, K. J.; Dasgupta, P. K.; Raimundo, I. M.; Temkin, H. *Anal. Chim. Acta* **2003**, *479*, 151-165.
- (35) Li, J.; Dasgupta, P. K.; Genfa, Z. *Talanta* **1999**, *50*, 617-623.
- (36) Bo, T.; Pawliszyn, J. *J Chromatogr A* **2006**, *1105*, 25-32.
- (37) Bo, T.; Pawliszyn, J. *J Sep Sci* **2006**, *29*, 1018-1025.
- (38) Bo, T.; Pawliszyn, J. *Anal Biochem* **2006**, *350*, 91-98.
- (39) Bo, T.; Pawliszyn, J. *Electrophoresis* **2006**, *27*, 852-858.
- (40) Bo, T.; Pawliszyn, J. *Analytica Chimica Acta* **2006**, *559*, 1-8.
- (41) Wang, Z.; Wang, Y.; Cai, W.-J.; Liu, S.-Y. *Talanta* **2002**, *57*, 69-80.
- (42) Liu, Z.; Pawliszyn, J. *Anal. Chem* **2003**, *75*, 4887-4894.
- (43) Belz, M.; Dress, P.; Klein, K.-F.; Boyle, W. J. O.; Franke, H.; Grattan, K. T. V. *Water Sci. Technol* **1998**, *37*, 279-284.
- (44) Li, J.; Dasgupta, P. K. *Anal. Sci* **2003**, *19*, 517-523.
- (45) Jamieson, E. R.; Lippard, S. J. *Chemical Reviews* **1999**, *99*, 2467-2498.
- (46) Dress, P.; Franke, H. *Rev. Sci. Instrum* **1997**, *68*, 2167-2171.

Chapter 5. References

- (1) Hjerten, S.; Zhu, M. D. *Journal of Chromatography* **1985**, *346*, 265-270.
- (2) Liu, Z.; Pawliszyn, J. *Analytical Chemistry* **2003**, *75*, 4887-4894.
- (3) Bo, T.; Pawliszyn, J. *Analytica Chimica Acta* **2006**, *559*, 1-8.
- (4) Reedijk, J. *Chemical Communications* **1996**, 801-806.
- (5) Liu, Z.; Drabovich, A. P.; Krylov, S. N.; Pawliszyn, J. *Analytical Chemistry* **2007**, *79*, 1097-1100.
- (6) Bo, T.; Pawliszyn, J. *J Chromatogr A* **2006**, *1105*, 25-32.
- (7) Bo, T.; Pawliszyn, J. *J Sep Sci* **2006**, *29*, 1018-1025.
- (8) Bo, T.; Pawliszyn, J. *Anal Biochem* **2006**, *350*, 91-98.
- (9) Bo, T.; Pawliszyn, J. *Electrophoresis* **2006**, *27*, 852-858.
- (10) Liu, Z.; Lemma, T.; Pawliszyn, J. *Journal of Proteome Research* **2006**, *5*, 1246-1251.
- (11) Cvitkovic, E. *Seminars in oncology* **1998**, *25*, 1-3.

- (12) Graham, M. A.; Lockwood, G. F.; Greenslade, D.; Brienza, S.; Bayssas, M.; Gamelin, E. *Clinical Cancer Research* **2000**, *6*, 1205-1218.
- (13) <http://www.dupont.com/teflon/af/performance.html>.
- (14) Dunn, T. A.; Schmoll, H. J.; Gruenwald, V.; Bokemeyer, C.; Casper, J. *Investigational New Drugs* **1997**, *15*, 109-114.
- (15) Soulie, P.; Bensmaine, A.; Garrino, C.; Chollet, P.; Brain, E.; Fereres, M.; Jasmin, C.; Musset, M.; Misset, J. L.; Cvitkovic, E. *European Journal of Cancer* **1997**, *33*, 1400-1406.
- (16) Gamelin, E.; Le Bouil, A.; Boisdron-Celle, M.; Turcant, A.; Delva, R.; Cailleux, A.; Krikorian, A.; Brienza, S.; Cvitkovic, E.; Robert, J.; Larra, F.; Allain, P. *Clinical Cancer Research* **1997**, *3*, 891-899.
- (17) O'Dwyer, P. J.; Stevenson, J. P.; Johnson, S. W., 2000.
- (18) Louvet, C.; Andre, T.; Tigaud, J. M.; Gamelin, E.; Douillard, J. Y.; Brunet, R.; Francois, E.; Jacob, J. H.; Levoir, D.; Taamma, A.; Rougier, P.; Cvitkovic, E.; de Gramont, A. *Journal of Clinical Oncology* **2002**, *20*, 4543-4548.
- (19) Kern, W.; Beckert, B.; Lang, N.; Stemmler, J.; Beykirch, M.; Stein, J.; Goecke, E.; Waggershauer, T.; Braess, J.; Schalhorn, A.; Hiddemann, W., 2001.
- (20) Eastman, A. *Biochemistry* **1982**, *21*, 6732-6736.
- (21) Jamieson, E. R.; Lippard, S. J. *Chemical Reviews* **1999**, *99*, 2467-2498.
- (22) Go, R. S.; Adjei, A. A. *Journal of Clinical Oncology* **1999**, *17*, 409-422.
- (23) Kung, A.; Strickmann, D. B.; Galanski, M.; Keppler, B. K. *Journal of Inorganic Biochemistry* **2001**, *86*, 691-698.
- (24) Gullo, J. J.; Litterst, C. L.; Maguire, P. J.; Sikic, B. I.; Hoth, D. F.; Woolley, P. V. *Cancer chemotherapy and pharmacology* **1980**, *5*, 21-26.
- (25) Boisdron-Celle, M.; Lebouil, A.; Allain, P.; Gamelin, E. *Bulletin du cancer* **2001**, *88 Spec No*, S14-19.
- (26) Pendyala, L.; Creaven, P. J. *Cancer Research* **1993**, *53*, 5970-5976.
- (27) Rai, D. K.; Landin, B.; Alvelius, G.; Griffiths, W. J. *Analytical Chemistry* **2002**, *74*, 2097-2102.
- (28) Espinosa, E.; Feliu, J.; Zamora, P.; Gonzalez Baron, M.; Sanchez, J. J.; Ordon ez, A.; Espinosa, J. *Lung cancer* **1995**, *12*, 67-76.
- (29) Takahashi, I.; Ohnuma, T.; Kavy, S.; Bhardwaj, S.; Holland, J. F. *British Journal of Cancer* **1980**, *41*, 602-608.
- (30) Ohta, N.; Chen, D.; Ito, S.; Futo, T.; Yotsuyanagi, T.; Ikeda, K. *International Journal of Pharmaceutics* **1995**, *118*, 85-93.
- (31) Ivanov, A. I.; Christodoulou, J.; Parkinson, J. A.; Barnham, K. J.; Tucker, A.; Woodrow, J.; Sadler, P. J. *Journal of Biological Chemistry* **1998**, *273*, 14721-14730.
- (32) Neault, J. F.; Tajmir-Riahi, H. A. *Biochimica et Biophysica Acta* **1998**, *1384*, 153-159.
- (33) Gibson, D.; Costello, C. E. *European Mass Spectrometry* **1999**, *5*, 501-510.
- (34) Esposito, B. P.; Najjar, R. *Coordination Chemistry Reviews* **2002**, *232*, 137-149.

- (35) Timerbaev, A. R.; Aleksenko, S. S.; Polec-Pawlak, K.; Ruzik, R.; Semenova, O.; Hartinger, C. G.; Oszwaldowski, S.; Galanski, M.; Jarosz, M.; Keppler, B. K. *Electrophoresis* **2004**, *25*, 1988-1995.
- (36) Warnecke, A.; Fichtner, I.; Garmann, D.; Jaehde, U.; Kratz, F. *Bioconjugate Chemistry* **2004**, *15*, 1349-1359.
- (37) Rudnev, A. V.; Aleksenko, S. S.; Semenova, O.; Hartinger, C. G.; Timerbaev, A. R.; Keppler, B. K. *Journal of Separation Science* **2005**, *28*, 121-127.
- (38) Timerbaev Andrei, R.; Hartinger Christian, G.; Aleksenko Svetlana, S.; Keppler Bernhard, K. *Chemical reviews* **2006**, *106*, 2224-2248.
- (39) He, X. M.; Carter, D. C. *Nature* **1992**, *358*, 209-215.
- (40) Li, Y.; Yan, X.-P.; Chen, C.; Xia, Y.-L.; Jiang, Y. *Journal of Proteome Research* **2007**, *6*, 2277-2286.
- (41) Yotsuyanagi, T.; Ohta, N.; Futo, T.; Ito, S.; Chen, D.; Ikeda, K. *Chemical & Pharmaceutical Bulletin* **1991**, *39*, 3003-3006.
- (42) Liu, X.; Wang Zhaohui, A.; Byrne Robert, H.; Kaltenbacher Eric, A.; Bernstein Renate, E. *Environmental science & technology* **2006**, *40*, 5036-5044.
- (43) Lemma, T.; Mandal, R.; Li, X.-F.; Pawliszyn, J. *J. Sep. Sci.* **2008**, *31*, 1803-1809.
- (44) Lee, P., C.; Meisel, D., D. *Phys. Chem* **1982**, *86*, 3391-3395.
- (45) Binnig, G.; Quate, C., F. *Physical Review Letters* **1986**, *56*, 930.
- (46) Ashutosh, S.; Stephen G., S. *Introduction to Fluorescence Spectroscopy*; John Wiley & Sons, Inc., New York, 1999.
- (47) Lakowicz, J. R.; Weber, G. *Biochemistry* **1973**, *12*, 4161-4170.
- (48) Neil, S.; Ulrich, N.; Siegfried, S. *Journal of Colloid and Interface Science* **1999**, *211*, 122-129.

Chapter 6. References

- (1) Tang, Q.; Harrata, A. K.; Lee, C. S. *Anal. Chem* **1995**, *67*, 3515-3519.
- (2) Tang, Q.; Harrata, A. K.; Lee, C. S. *Anal. Chem* **1997**, *69*, 3177-3182.
- (3) Yang, L.; Lee, C. S.; Hofstadler, S. A.; Pasa-Tolic, L.; Smith, R. D. *Anal. Chem* **1998**, *70*, 3235-3241.
- (4) Loo, R. R. O.; Cavalcoli, J. D.; VanBogelen, R. A.; Mitchell, C.; Loo, J. A.; Moldover, B.; Andrews, P. C. *Anal. Chem* **2001**, *73*, 4063-4070.
- (5) Giorgianni, F.; Desiderio, D. M.; Beranova-Giorgianni, S. *Electrophoresis* **2003**, *24*, 253-259.
- (6) Wu, J.; Pawliszyn, J. *Anal. Chem* **1992**, *64*, 2934-2941.
- (7) Wu, J.; Pawliszyn, J. *Anal. Chem* **1992**, *64*, 224-227.
- (8) Wu, J.; Pawliszyn, J. *Anal. Chem* **1994**, *66*, 867-873.
- (9) Wu, J.; Tragas, C.; Watson, A.; Pawliszyn, J. *Anal. Chim* **1999**, *383*, 67-78.
- (10) Wu, J.; Watson, A.; Torres, A. R. *Am. Biotechnol. Lab* **1999**, *17*, 24-26.
- (11) Liu, Z.; Pawliszyn, J. *Anal. Chem* **2003**, *75*, 4887-4894.
- (12) Liu, Z.; Pawliszyn, J. *J. Proteome Res* **2004**, *3*, 567-571.

- (13) Liu, Z.; Pawliszyn, J. *Anal. Biochem* **2005**, *336*, 94-101.
- (14) Einstein, A. **1905**.
- (15) Young, M. E.; Carroad, P. A.; Bell, R. L. *Biotechnol. Bioeng* **1980**, *22*, 947-955.
- (16) Tyn, M. T.; Gusek, T. W. *Biotechnol. Bioeng* **1990**, *35*, 327-338.
- (17) He, L.; Niemeyer, B. *Biotechnol. Prog* **2003**, *19*, 544-548.
- (18) Schachman, H., K. In *Methods in Enzymology*; Colowick, S., P., Kaplan, N., O., Eds.; Academic Press, New York, 1957; Vol. 4.
- (19) Van Holde, K., E.; Neurath, H., Hill, R., L., Eds.; Academic Press, New York, 3rd, 1975; Vol. 1.
- (20) Berne, B., J.; Pecora, R. *Dynamic Light Scattering*; Wiley Interscience, New York, 1976.
- (21) Stejskal, E., O.; Tanner, J., E. *J. Chem. Phys* **1965**, *42*, 288.
- (22) Loris, R.; Steyaert, J.; Maes, D.; Lisgarten, J.; Pickersgill, R.; Wyns, L. *Biochemistry* **1993**, *32*, 8772-8781.
- (23) Gerhardt, G.; Adams, R. N. *Anal. Chem* **1982**, *54*, 2618-2620.
- (24) Behlke, J.; Risata, O. *Biochem. Soc. Trans* **1998**, *26*, 758-761.
- (25) Smith, M. H. In *Handbook of Biochemistry*; Sober, H.A., Ed.; Chemical Ruber Company:: Cevland, 1970.
- (26) Chen, B.; Chrambach, A.; Rodbard, D. *Anal. Biochem* **1979**, *97*, 120-130.
- (27) Chu, B.; Yeh, A.; Chen, F. C.; Weiner, B. *Biopolymers* **1975**, *14*, 93-109.
- (28) Walbroehl, Y.; Jorgenson, J., W. *J. Microcol. Sep* **1989**, *1*, 41-45.
- (29) Lide, R., David. *CRC Handbook of Chemistry and Physics*, 88th Edition ed.; CRC Press/Taylor and Francis, Boca Raton, FL., 2008.